A STUDY OF NOVEL SUPERCONDUCTING STATES IN HYBRID FERROMAGNETIC-SUPERCONDUCTING METAMATERIALS AND THIN FILM DEVICES

Rhea Stewart

A Thesis Submitted for the Degree of PhD
at the
University of St Andrews

2019

Please use this identifier to cite or link to this thesis:
http://hdl.handle.net/10023/18956

A study of novel superconducting states in hybrid ferromagnetic-superconducting metamaterials and thin film devices

Rhea Stewart

University of
St Andrews

This thesis is submitted in partial fulfillment for the degree of
Doctor of Philosophy (PhD)
at the University of St Andrews

August 2019

Candidate's declaration

I, Rhea Stewart, do hereby certify that this thesis, submitted for the degree of PhD, which is approximately 48,000 words in length, has been written by me, and that it is the record of work carried out by me, or principally by myself in collaboration with others as acknowledged, and that it has not been submitted in any previous application for any degree.

I was admitted as a research student at the University of St Andrews in August 2015.

I received funding from an organisation or institution and have acknowledged the funder(s) in the full text of my thesis.

Date Signature of candidate

Supervisor's declaration

I hereby certify that the candidate has fulfilled the conditions of the Resolution and Regulations appropriate for the degree of PhD in the University of St Andrews and that the candidate is qualified to submit this thesis in application for that degree.

Date Signature of supervisor

Permission for publication

In submitting this thesis to the University of St Andrews we understand that we are giving permission for it to be made available for use in accordance with the regulations of the University Library for the time being in force, subject to any copyright vested in the work not being affected thereby. We also understand, unless exempt by an award of an embargo as requested below, that the title and the abstract will be published, and that a copy of the work may be made and supplied to any bona fide library or research worker, that this thesis will be electronically accessible for personal or research use and that the library has the right to migrate this thesis into new electronic forms as required to ensure continued access to the thesis.

I, Rhea Stewart, confirm that my thesis does not contain any third-party material that requires copyright clearance.

The following is an agreed request by candidate and supervisor regarding the publication of this thesis:

Printed copy

No embargo on print copy.

Electronic copy

No embargo on electronic copy.

Date Signature of candidate

Date Signature of supervisor

Underpinning Research Data or Digital Outputs

Candidate's declaration

I, Rhea Stewart, understand that by declaring that I have original research data or digital outputs, I should make every effort in meeting the University's and research funders' requirements on the deposit and sharing of research data or research digital outputs.

Date Signature of candidate

Permission for publication of underpinning research data or digital outputs

We understand that for any original research data or digital outputs which are deposited, we are giving permission for them to be made available for use in accordance with the requirements of the University and research funders, for the time being in force.

We also understand that the title and the description will be published, and that the underpinning research data or digital outputs will be electronically accessible for use in accordance with the license specified at the point of deposit, unless exempt by award of an embargo as requested below.

The following is an agreed request by candidate and supervisor regarding the publication of underpinning research data or digital outputs:

No embargo on underpinning research data or digital outputs.

Date Signature of candidate

Date Signature of supervisor

Abstract

In hybrid mesoscopic systems the Meissner response of a superconducting film can be very different from its bulk behaviour. For instance, in normal (N) superconductor (S) bilayers screening can be greatly enhanced depending on the relative material properties and interface conditions. Furthermore, with the addition of ferromagnetic (F) layers comes the possibility of generating a paramagnetic screening response due to spin triplet pairs. Such pairs are produced from the mixing of opposing microscopic orders within S (which conventionally hosts electron pairs of opposite spin and momenta) and F (inside which spin symmetry is broken). The net result is a conversion of a fraction of the pairs to an odd-frequency s-wave triplet state. Any resultant modifications to the screening manifest in the flux profile across a sample which is directly probed using low energy muon spin rotation (LEμSR).

Results of LEμSR experiments involving layered systems comprised of N, S and F elements are presented within chapter 3. A discrepancy between the pre-existing quasiclassical theory and measured flux profiles in the presence of an F layer was observed. A large enhancement to the flux lowering which could not be interpreted within the traditional S/F proximity picture was found. New theoretical developments have since suggested that coupled to direct electronic proximity effects within these systems is an additional electromagnetic component. Chapter 4 presents the results of analysing LEμSR data using a spatial flux profile consistent with new theory. In doing so, the observed anomalous enhancement could be successfully reconciled with the electromagnetic proximity effect. Subsequent experimental work in chapters 4-6 sought to test the main predictions of the theory by manipulating S/F interfaces within a variety of different structures. In all tested cases the theory provided an excellent description of experiment suggesting the importance of considering electromagnetic effects within S/F hybrid systems.

Acknowledgements

The work presented within this thesis is not the achievement of just a single person. There have been many contributions of various different types from many different people. I am sure what is written here will not manage to cover them all but I hope to give a sense of the appreciation I have for the support, both academic and otherwise, I have received during the completion of this project.

First and foremost I would like to acknowledge the supervisory role of Professor Steve Lee. It has been a pleasure to work as part of your group for the past few years and I really appreciate the freedom I have been given to explore all aspects of physics that interest me (whether or not they were directly related to my thesis topic). Your understanding, enthusiasm, curiosity and support have been essential to the completion of this project[1] and I am sincerely grateful for the training I have received from you over the course of my time in St Andrews. I have also been fortunate enough to work with Dr Machiel Flokstra who has had a substantial role in the shaping of this project and my development as a physicist. Your knowledge of the field and skill with both experiment and theory has been an inspiration. Some of my favourite PhD moments were at the LEM beamline in the midst of the seventh sample change of the experiment. I think we must have set a sample change record by now! These muon experiments, however, would not have been possible without samples, or indeed the low energy muon facility at PSI, and this brings me to the next round of scientific acknowledgements. All of the sample growth was carried out at The University of Leeds with the aid of Dr Gavin Burnell and associated group members. I would like to specifically acknowledge the work of Gavin Burnell, Nathan Satchell and Matthew Rogers, all of whom have been instrumental in the work presented within this thesis. In addition to working with the team in Leeds, I have

---

[1] As has your inside knowledge of the best coffee machines at PSI and the discussions we and Machiel have had whilst standing around them.

also spent a great deal of time as a user of the LEM beamline at PSI where most of our measurements were performed. I cannot overstate how much I have enjoyed working both with the instrument and the beamline scientists who are responsible for its upkeep and development. I would like to extend thanks especially to Drs Thomas Prokscha, Hubertus Luetkens and Andreas Suter whose technical support and enthusiasm for our work I greatly appreciated. I would also like to thank Drs Chi Ming Yim and David Miller of the STM and electron microscopy groups in St Andrews respectively for their support with crucial measurements on our thin film systems.

As a student within the Condensed Matter Centre for Doctoral Training I have had access to many professional and scientific development resources, based both locally and remotely, all of which has been coordinated by an excellent team of supporting staff. I would like to extend gratitude to Christine, Julie, Wendy and Debra for all of their help, at various different times, in making the logistics of completing this PhD as smooth as possible. I thoroughly enjoyed being a part of the St Andrews branch of Cohort 7 alongside Artem, Danius, Maja, Mike and Veronika!

More broadly, during my time as a PhD student within the Physics department I have had the good fortune to work alongside a great many PhD student and postdoctoral peers. I would like to highlight a few of the ways in which they have enriched the experience of PhD life. The year in office 120 was a happy one during which collaborative problem solving at the whiteboard, cake competitions and office nonsense featured heavily. This was in large part due to the company of Maja, Scott and Veronika.[2] I would like to thank all three of them for both their friendship and their participation in our helpful physics discussions. In the following years I have relocated to office 166A which at various times has been shared with Helen, Conor and Laura, with relatively frequent and appreciated visits from Chris, Igor, Kristín, Natalie and Steph, all of whom have contributed to the homely and diverse nature of the office. Thanks for making the work environment an enjoyable place to be! Outside of working it has been a pleasure to get to know you all. Taste trips formed an important part of the day on most days and it was lovely to have the company of so many fellow flat white drinkers: Conor, Kristín, Matt, Natalie, Scott, Steph and Veronika to name a few.

---

[2] Who it turns out, due to her choice of desk and Scott's choice of office activities, had to live in constant fear of projectiles.

Natalie, I have enjoyed our art sessions, bad movie nights and general banter immensely over the past three years. Keep raging on with those ideas of the month! Conor, I have enjoyed our conversations and now have a new found appreciation for birds, classical music and Mathematica. Laura, thanks for opening up your house to our board gaming sessions. Your company and good, honest advice has been greatly appreciated. Igor, our excellent and eclectic discussions were a very welcome distraction and your enthusiasm for physics and beyond has been infectious. Kristín and Steph, I have enjoyed our walks and your positivity in all things has been a great help this past few months. Without all you comrades...things could have been pretty dire!

I would like also to extend my appreciation to a number of friends and family from outwith the physics community. Nia, thanks for keeping me connected to the world! Our shared sense of humour and love of the absurd has kept me going through some trying times.[3] Caroline and Alex, your support has meant a lot to me and I hope one day to be able to reciprocate. Annan, my work has taken a great deal of my time and my focus. Your patience, understanding and continued support was and is greatly appreciated. I would like to express gratitude to both my Auntie Tanya and to my sister Chloë for bearing the brunt of some very difficult circumstances such that I could continue to focus on my work and personal well-being. Finally, I would like to thank my parents, Roy and Debbie, without whom I would never have been in the position to write these acknowledgements. My studies, both undergraduate and postgraduate, took so much of my time from them and as such I would like to dedicate the work within this thesis to them both.

---

[3] I think that is -3 MP to me for being so soppy.

Publications

- **R. Stewart**, M. G. Flokstra, M. Rogers, N. Satchell, G. Burnell, D. Miller, H. Luetkens, T. Prokscha, A. Suter, E. Morenzoni, S. Langridge and S. L. Lee, Controlling the electromagnetic proximity effect by tuning the mixing between superconducting and ferromagnetic order. *Phys. Rev. B.* **100**, 020505(R) (2019).
- M. G. Flokstra, **R. Stewart**, N. Satchell, G. Burnell, H. Luetkens, T. Prokscha, A. Suter, E. Morenzoni and S. L. Lee, Manifestation of the electromagnetic proximity effect in superconductor-ferromagnet thin film structures. *Appl. Phys. Lett.* **115**, 072602 (2019).
- M. G. Flokstra, **R. Stewart**, N. Satchell, G. Burnell, H. Luetkens, T. Prokscha, A. Suter, E. Morenzoni, S. Langridge and S. L. Lee, Observation of Anomalous Meissner Screening in Cu/Nb and Cu/Nb/Co Thin Films. *Phys. Rev. Lett.* **120**, 247001 (2018).
- F. Al Ma'Mari, M. Rogers, S. Alghamdi, T. Moorsom, S. L. Lee, T. Prokscha, H. Luetkens, M. Valvidares, G. Teobaldi, M. G. Flokstra, **R. Stewart**, P. Gargiani, M. Ali, G. Burnell, B. J. Hickey, and O. Cespedes, Emergent magnetism at transition-metal–nanocarbon interfaces. *PNAS* **114(22)**, 5583 (2017).

Funding

The work presented in this thesis was financially supported by the University of St Andrews and the Scottish Doctoral Training Centre in Condensed Matter Physics under EPSRC grant number: **EP/L015110/1**.

Additional funding for experiments and related equipment was received from the following EPSRC grant numbers: EP/I031014/1, EP/J010634/1, EP/R031924/1, EP/R023522/1 and EP/L017008/1.

Contents

List of Figures

List of Tables

1 | Introduction

The interaction between conflicting types of microscopic order which are forced to coexist can give rise to new states of matter. One manifestation of this is within superconductor-ferromagnet heterostructures which, depending on the particulars of the materials involved and the precise geometries employed, can play host to a variety of emergent physics including unconventional superconductivity and topological states of matter [1–4]. These structures therefore open up a broad and very active field of research with a variety of potential applications, all of which rely on understanding and manipulating effects at buried interfaces. The generation of unconventional superconducting states through proximity of conventional superconductivity to ferromagnetism is just one facet of this field and is the primary focus of the work presented within this thesis.

Conventional superconducting correlations (S) form between electron states of opposite spin and momentum whilst ferromagnetism (F) involves the breaking of spin symmetry. Hybrid systems in which these orders are mixed combine the low temperature zero resistance of the superconductor [5, 6] with the spin polarisation of the ferromagnet. At carefully engineered interfaces between S and F the direct transfer of electrons across the interface results in a number of experimentally observed transport phenomena such as oscillations in critical current and critical temperature (T_c) [7–16], π phase shifts of the superconducting wavefunctions [17–20], T_c suppression [21] and long range triplet supercurrents due to the presence of equal spin triplet pairs [22–29]. The unconventional nature of the pairs present within S/F systems, however, does not only manifest within transport measurements. A paramagnetic Meissner screening, as opposed to the conventional diamagnetic response [30], was also predicted [31] and observed [32] to occur within these hybrid systems. Another consequence of these interactions is the inverse proximity effect [33–35]. This involves the transfer of a small magnetisation from the ferromagnet to the superconductor, through the formation of spin polarised pairs, over a lengthscale given by the superconducting coherence length. There is some experimental evidence of inverse proximity [36, 37] though in a series of experiments which probe the S/F interface in detail very different behaviour is observed [38, 39]. Over the past two years, however, new theoretical developments have worked to reconcile these observations through the description of a new type of proximity of electromagnetic origin [40–42]. This describes the screening response of the superconductor due to the vector potential at the S/F interface over a much longer lengthscale given by the London penetration depth. The interaction of these different types of proximity effect, all largely occurring with a region spatially localised around buried S/F interfaces, is of fundamental importance to understanding the overall behaviour of devices with more complex sample structures.

In this thesis the focus is primarily on measuring the screening response, in a spatially localised way using low energy muon spin rotation measurements, of simple layered systems comprised of normal metal (N), superconducting and ferromagnetic layers. The core of the sample systems discussed within each chapter are built from N/S and S/F interfaces which when combined generate a wealth of interesting consequences to the screening response of the proximitised system. Prior to presenting the experimental techniques and results, a brief discussion of the physics pertinent to these investigations is given.

1.1 A general introduction to N/S/F hybrid systems

The purpose of this section is to simply provide a brief overview of background physics and literature which is relevant to all work presented within the subsequent experimental chapters. Further details are provided within each chapter where appropriate to both motivate and contextualise the work.

1.1.1 Conventional mesoscopic superconductivity

The first building block of S/F hybrid systems is a conventional superconductor which, in all of the systems discussed within this thesis takes the form of a mesoscopic[4] thin film of niobium. The superconducting pairing in such a system at equilibrium, in the absence of any other interactions and at zero temperature, remains well described by the BCS Hamiltonian [43–45]

$$\mathcal{H} = \sum_{k,\sigma} \epsilon_k n_{k\sigma} + \sum_{k,k'} V_{kk'} c^{\dagger}_{k\uparrow} c^{\dagger}_{-k\downarrow} c_{-k'\downarrow} c_{k'\uparrow} \ , \tag{1.1}$$

where $n_{k\sigma} = c^{\dagger}_{k\sigma} c_{k\sigma}$ is the number operator, ϵ_k is the single particle energy and $V_{kk'}$ is the attractive interaction potential. There are two terms within equation 1.1. The first represents the total kinetic energy whilst the second describes the scattering of electron pairs, under the influence of an attractive interaction potential $V_{kk'}$, from state $(k^{'} \uparrow, -k^{'} \downarrow)$ to $(k \uparrow, -k \downarrow)$. The pairing described by equation 1.1 occurs between electrons of equal and opposite spin and momenta found within a shell of states of $k_B T_c$ around the Fermi energy. This conventional BCS pairing is illustrated within figure 1.1 for electron (filled symbols) and hole (empty symbols) states.

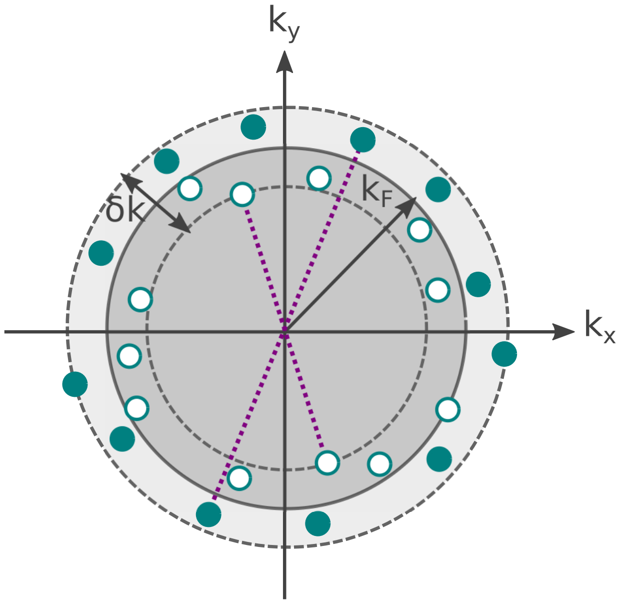

Figure 1.1: A schematic illustration of BCS pairing in k-space. All of the states involved in paring sit within a envelope δk around the Fermi wavevector k_F where $k_F \gg \delta k$. The dark and light shaded regions correspond to filled and empty states respectively. The filled (empty) circles correspond to electron (hole) states whilst the pairing interaction between equal and opposite states is represented by the dotted lines.

---

[4] Systems in which the layer thickness is of the order of a coherence length (ξ_S) where ξ_s is typically of the order of 10 nm for sputtered thin films of niobium.

Importantly, the Fermi spheres to which each member of a Cooper pair belong are degenerate. If this symmetry between states should be broken the pairing strength is weakened. There are two types of symmetry breaking effect which can occur: orbital and paramagnetic [46]. The orbital effect involves a shift in the positions of the Fermi spheres within k-space where one member of a pair acquires a net momentum with respect to the other, for example, within the presence of an external electromagnetic field. Paramagnetic pair breaking effects, however, involve a change in relative Fermi surface size and correspond to a splitting in energy of the two possible spin states. Within the presence of either effect, transitions between the superconducting and normal states are possible depending on the relative strength of the pairing interaction and the pair breaking.

Whilst the microscopic picture of pairing remains unchanged the relevant lengthscales within mesoscopic thin films can be very different from those of conventional bulk systems. The superconducting transition temperature, T_c, and superconducting coherence length, ξ_s, are often reduced when compared with a bulk crystalline system. In the case of niobium, for example, the bulk values of $T_c \approx 9.2\ K$ and $\xi_s \approx 30\ nm$ [47, 48] are typically reduced to $8.7\ K$ and $12\ nm$ respectively in the sputtered thin film systems measured here.[5] Importantly, the London penetration depth (λ_L), the lengthscale over which an applied field is screened, is also greatly altered in dirty[6] thin film systems. Since niobium is a type two superconductor it is expected that $\xi_s \leq \lambda_L$ [47]. For clean niobium $\lambda_L \approx 30\ nm$ [49–51] whereas in dirty superconducting systems the penetration length increases with decreasing mean free path and values of up to $270\ nm$ have been determined [52, 53]. As a consequence of such a long penetration depth, a dirty thin film where the thickness $ds < \lambda_L$ can no longer expel all of the flux from its interior in the presence of an external field.

1.1.2 Normal metal-superconductor proximity

Whilst Cooper pairs are eigenstates of superconducting materials, and are therefore only produced within superconductors, they can propagate across interfaces with normal metals *via* the superconducting proximity effect.

---

[5] The effect on T_c is due to a decrease in the purity of the niobium in its sputtered thin film form when compared with the bulk.

[6] In this case dirty means that the mean free path, l, is less than ξ_s. Typically $l = (1-3)\ nm$ and $\xi_s = (10-14)\ nm$ for the systems measured here.

This process allows the transfer of superconducting properties to a normal metal and was first observed as a zero resistance in superconductor-normal metal-superconductor junctions which have since become an important and widely studied sample architecture.

The theory of proximity between a conventional superconductor and a normal conductive metal was primarily developed during the 1960s by de Gennes and Guyon and Werthamer [54, 55]. The general principle involves the penetration of Cooper pair correlations into a normal metal which is in electronic contact with a superconductor over some lengthscale defined by both the system temperature and the properties of the metal. For diffusive systems, akin to those measured here, the presence of impurities decreases the efficiency of the transport when compared with clean systems. Within such a diffusive system, in three dimensions, the lengthscale over which the pairs can propagate within the normal metal is given by ξ_N, the coherence length within the normal metal, as shown in equation 1.2

$$\xi_N = \sqrt{\frac{\hbar D}{2\pi k_B T}} \quad \text{, with} \quad D = \frac{1}{3} v_F l, \tag{1.2}$$

where D is the diffusion constant and l the mean free path of the normal metal. The strength of the resultant proximity effect is related to both the superconducting gap and the transmission potential of the normal-superconducting interface. The leaking out of pairs into N is accompanied by a corresponding weakening of the superconducting gap within S on approach to the interface. The spatial profile of the gap is represented by the schematic diagram shown in figure 1.2 where the gap function is plotted in purple. The pair amplitude propagates into the normal metal over a distance defined by ξ_N where the corresponding reduction in pairs within the superconductor occurs over ξ_S as indicated. For a typical dirty normal metal $(10 \leq \xi_N \leq 100)$ nm which is comparable to ξ_S for the thin film niobium systems measured here. The precise values of the coherence lengthscales are material dependent and can vary markedly between growth runs, as is discussed within chapter 3, having a profound effect on the measured behaviour.

The mechanism through which the pairs traverse the interface is known as Andreev reflection [56, 57]. Within a superconductor-normal metal junction at $T < T_c$ transport of single electrons with $E \approx E_F$ is blocked by the superconducting energy gap, however, *via* Andreev reflection processes it is possible for Cooper pairs to be transferred across the interface as illus-

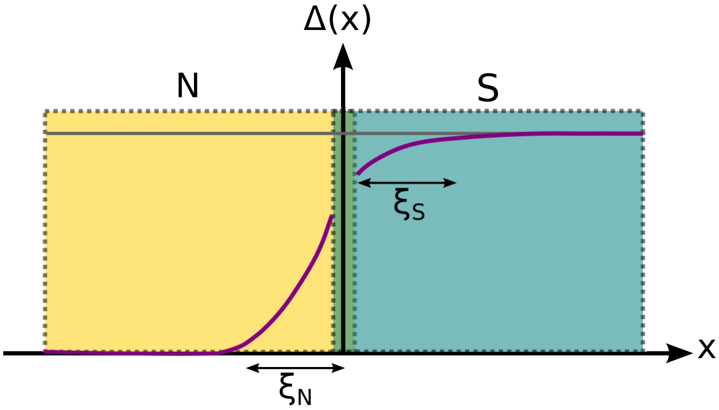

Figure 1.2: The spatial profile of the superconducting gap across an N/S interface. The gap propagates into the normal metal (N) over a lengthscale given by ξ_N and there is a corresponding weakening in the gap on the superconducting side (S) over a lengthscale ξ_S.

trated in figure 1.3. Within the normal metal, an excited electron of energy $E < \Delta$ propagates towards the interface. Ordinarily this electron would be reflected at the interface but instead it pairs with a valence electron, of opposite spin and approximately opposite momentum, sitting at energy $-E$. This electron pair can then pass into the superconductor as a Cooper pair in the ground state of the condensate. On the normal metal side a single hole is left within the valence band at energy $-E$, forming a correlated electron hole pair, which then back propagates into the metal. The opposite process may also occur. In this case, a valence band hole reaches the interface, plucks a Cooper pair out of the condensate which is then split into its constituent electrons. These then occupy the original valence band hole state and an excited state within the conduction band of the normal metal. In either case the net result of Andreev reflection is the transfer of two electron charges across the interface.

The correlated electron hole pair which results within the normal metal transmits superconducting properties over a distance ξ_N along the propagation direction. This pair is not bound *via* the attractive interaction of a standard Cooper pair and is consequently less robust. As mentioned above, the process of Andreev reflection is allowed for states where the momenta are approximately equal but opposite. The possible momentum shift, $2\delta k \gg k_F$, between the two electron states has important consequences for the pairing. Even in the absence of pair breaking effects the momentum shift results in a dephasing of the pairs with propagation distance. This occurs over a lengthscale of ξ_N for diffusive systems.

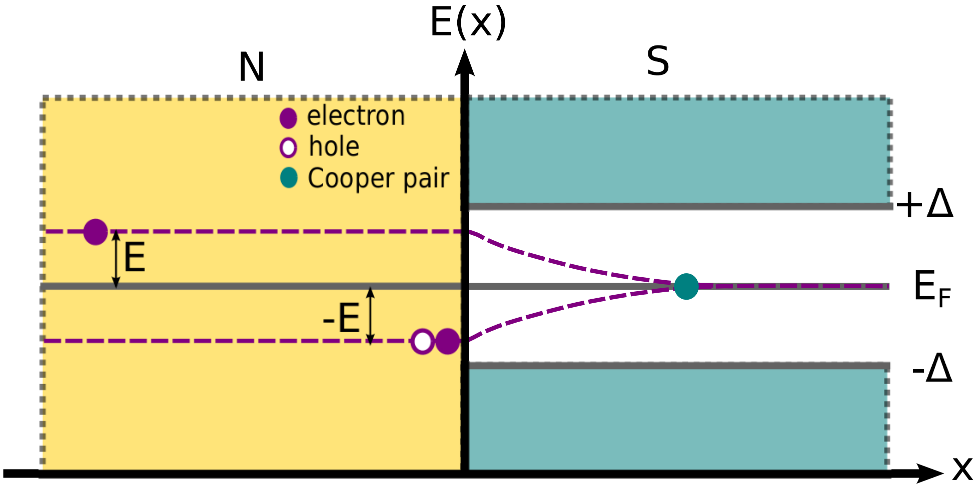

Figure 1.3: The process of Andreev reflection at the N/S interface. An electron sitting at energy E propagates towards the N/S interface where is acquires a partner electron of energy $-E$ with opposite spin and approximately opposite momentum. These propagate together into S as a Cooper pair. The opposite process may also occur.

The presence of the normal metal layer, and subsequent weakening of the superconductivity present within the total system, has a measurable effect on the transport properties of the thin film system. Perhaps the most easily accessible measure is the effect on the superconducting transition temperature. A very well documented reduction in T_c is observed, for a broad range of thin film superconducting systems, within the presence of an adjacent normal metal layer. The magnitude of this effect, for a fixed thickness of superconductor, depends largely on both the thickness of the normal metal and the properties of the N/S interface. For the systems measured within this thesis a suppression of $\approx 0.6\ K$ is routinely observed for an NS bilayer when compared with a comparable bare thin film of niobium.[7] More crucially, for the measurements presented within this thesis the presence of the normal metal layer can have a marked effect on the screening response of the system to an applied field. Within these mesoscopic bilayer systems, depending on the relative material parameters and interface conditions, it is possible for the normal metal layer to exhibit a Meissner response [58, 59]. This effect is largely determined by how the mean free path of the normal metal compares with the London penetration depth of the superconductor and is explored in detail within the measurements discussed in chapter 3. Surprisingly, given the right combination of material parameters it is pos-

---

[7] This typically corresponds to a percentage reduction of $\approx 7\%$ in the value of T_c.

sible, as demonstrated through theory and experiments (see for example [58, 60]), for the normal metal bilayer to be as effective at screening an external field as an equivalent thickness of niobium.

As a final note and link to the following section, the band structure properties of the normal conducting metal are crucially important to proximity with the superconductor. Within any material where the spin symmetry is broken, for example, the possible shift in momentum, $2\delta k$, between the paired electrons will be larger than in the normal metal and the effect of dephasing much stronger. Consequently, the lengthscale over which conventional pairs propagate will be shorter and alternative pairing mechanisms may be present. These ideas become important when one considers magnetic materials and heavy metals, where strong spin-orbit interaction may start to play a role, in close proximity to superconductivity [61, 62].

1.1.3 Superconductor-ferromagnet proximity

As discussed within section 1.1.2, the electrons which propagate across the interface within an N/S proximity system are of opposite spin and approximately equal but opposite momentum such that they form a Cooper pair. If the normal conducting metal is instead replaced by a ferromagnet this process can no longer happen in the same way since the spin symmetry is broken by the exchange field of the ferromagnet.[8] The first consequence is that the process of Andreev reflection is now of lower amplitude since there is a limited population within the minority spin band of the ferromagnet due to the exchange energy barrier [3, 46].[9] The second is that the pairing mechanism must now negotiate the spin split bands of the ferromagnet.

The process through which Andreev reflection can occur between a superconductor and ferromagnet is similar to the case for the N/S interface except the bands into which the electrons propagate are now spin split by an amount dependent on the exchange energy ($E_{ex} \ll E_F$). This results in a potential energy difference between the spin up and spin down states where an electron within the minority band is now of higher potential energy. The net consequence of this is that pairing must now occur between bands of slightly different momentum as illustrated within figure 1.4.

---

[8] This problem was first investigated experimentally by Tedrow and Meservey within magnetic tunnel junctions [63–65].

[9] This is in the absence of spin flip processes at the interface which in principle could allow Andreev reflection to occur from within a single spin band.

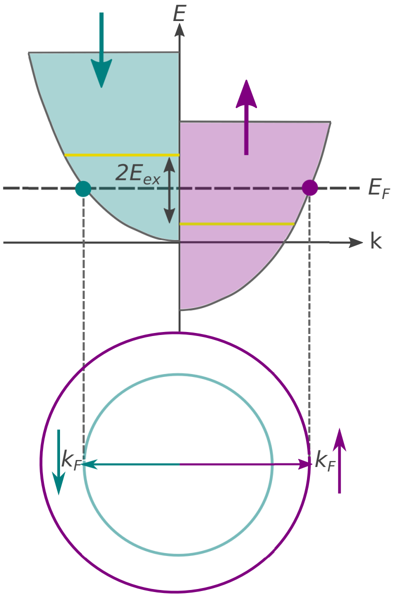

Figure 1.4: The effect of exchange splitting on the pairing. The minority (spin down) band is shifted up in energy when compared with the majority (spin up) band. The net result is a smaller k_F for the minority spin band when compared with the majority spin band. The consequence of this is that pairing must now take place between opposite spin states which are shifted with respect to one another in momentum space. This introduces a non-zero centre-of-mass momentum to the pairs.

An incoming electron of spin ↑ and momentum $k_{F,\uparrow}+\delta k$ must now pair with an electron of spin ↓ and an approximately opposite momentum which is shifted by an amount dependent on the exchange splitting. The increased potential of the minority spin band means that an electron which sits within a state of fixed energy, E, will have a lower kinetic energy than its counterpart within the majority spin band. Pairing between these two states results in the Cooper pair being left with a non-zero centre-of-mass momentum of $\frac{E\pm E_{ex}}{v_F}$ where v_F is the Fermi velocity. When electron pairing now occurs rather than the usual singlet state, $(\uparrow\downarrow - \downarrow\uparrow)e^{\frac{i2E}{\hbar v_F}}$, a pair of the form $(\uparrow\downarrow\, e^{\frac{i2E_{ex}}{\hbar v_F}} - \downarrow\uparrow\, e^{\frac{-i2E_{ex}}{\hbar v_F}})e^{\frac{i2E}{\hbar v_F}}$ results. This is directly akin to LOFF [66, 67] pairing but where rather than a bulk effect it is induced as a proximity amplitude. The new pairing present within the system can be decomposed into separate singlet, $(\uparrow\downarrow - \downarrow\uparrow)$, and triplet, $(\uparrow\downarrow + \downarrow\uparrow)$, components where even the equal spin triplets, $(\uparrow\uparrow)$ and $(\downarrow\downarrow)$, can be generated if the ferromagnetic exchange field itself is inhomogeneous [68, 69]. The equal spin triplet pairs are generated from the $m = 0$ triplet as it experiences multiple orientations of the exchange field and, given their spin orientation being akin to the ordering of a ferromagnet, they form the basis for long range triplet supercurrents which are now routinely realised within S/F proximity systems [3].

The proximity induced superconductivity close to the S/F interface is a mixture of both singlet and triplet character. As the pairs propagate into the ferromagnetic layer there is a spatial modulation of the two components of the pair amplitude bounded by an exponential decay envelope. The oscillations in pair amplitude, and the singlet and triplet mixing, occur over a lengthscale defined by the ferromagnetic coherence length as given in equation 1.3 where at low temperatures within a ferromagnet the dominant energy scale is the exchange energy, E_{ex}

$$\xi_F = \sqrt{\frac{\hbar D_F}{E_{ex}}} \,, \tag{1.3}$$

where D_F is the diffusion constant within the ferromagnet. This process of singlet-triplet mixing, and the associated lengthscales, are illustrated within figure 1.5. Importantly, the coherence length in the ferromagnet depends on the exchange energy. For strong ferromagnets, therefore, the lengthscales become much shorter and the damping of the amplitude more severe.

The majority of the measurements within this thesis use cobalt as the ferromagnetic layer. Due to the fact that cobalt is a strong ferromagnet the expected coherence length is of the order of only 1 nm.

The presence of the ferromagnet, and the associated generation of unconventional superconducting states, has a number of consequences for the behaviour of the superconducting system. These manifest in various ways within different types of measurement. Of course, owing to the damaging effect of the exchange field, there is a weakening of the superconducting gap which leads to a suppression in T_c when compared with the corresponding niobium thin film.[10] This suppression is dependent on the thickness of a given ferromagnetic layer in a non-monotonic way as has been measured for

---

[10] Typically for the Cu/Nb/Co systems measured within the experimental chapters of this thesis, the Co layer causes a drop in T_c of ≈ 0.7 K or about 8 % when compared with a control bilayer.

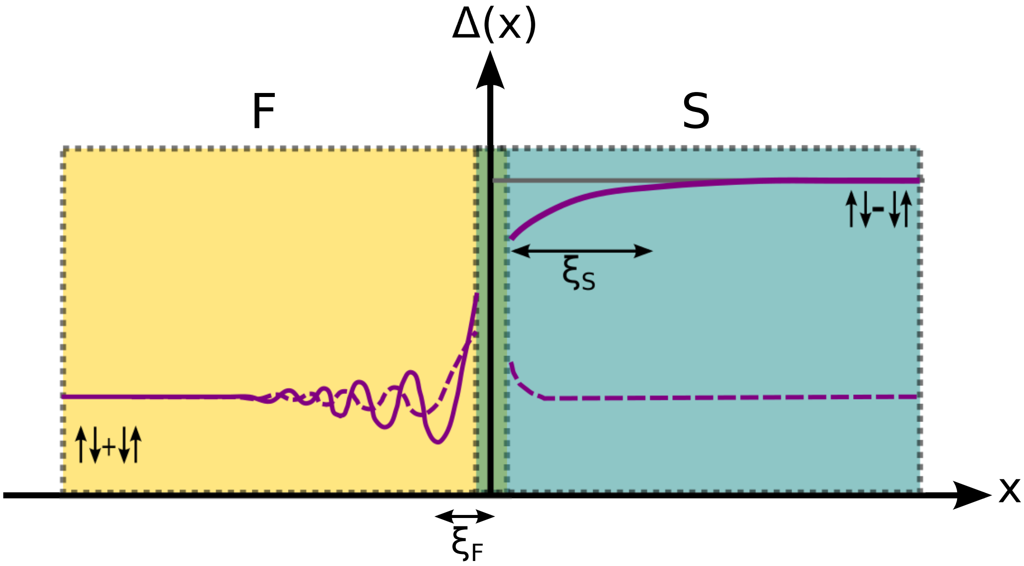

Figure 1.5: The spatial profile of the gap across an S/F interface. The singlet and triplet components are indicated using the solid and dashed lines respectively.

a wealth of different material systems (see for example [7–12]). The second important consequence to experiment, at least for the measurements conducted within the later experimental chapters of this thesis, is the possibility to generate a paramagnetic screening response to an applied field. Within a diffusive system, spin triplet states which are generated *via* the proximity effect remain in an s-wave orbital state so in order to preserve Fermi-Dirac statistics their frequency component must be odd [70, 71]. This anti-symmetry in time prompts the pairs to respond in an opposite sense to an applied magnetic field and results in a paramagnetic screening where flux is added rather than expelled from the interior of the superconductor [61]. This intriguing consequence of an odd frequency component to the superconducting state has now been experimentally observed [32]. It is also important to note that, coupled to the generation of unconventional superconducting states *via* direct proximity within S/F hybrids, there are other possible effects of proximity. These are inverse proximity [33–35], which involves the transfer of a small magnetisation to the superconductor *via* equal spin triplet pairs, and the newly described electromagnetic proximity effect [40–42] which is discussed in detail within chapter 4. Both of these possible contributions to S/F proximity are visible within the spatial flux profile across the proximitised system but are spatially localised around buried interfaces. In order to directly probe these effects, low energy muon spin rotation measurements, a technique which measures the local flux profile with high spatial precision, can be employed as discussed in section 2.1.

1.2 Aims and scope of the thesis

Given the possibility to generate unconventional states of matter not easily observable within bulk systems, it is clear why these interfaces between superconducting, normal metal and ferromagnetic materials are of fundamental interest. In addition, through combination of different material layers it is possible to manipulate the resultant proximity effects with useful applications in mind. The equal spin triplet states, in particular, are of interest since the pairs themselves carry a net spin which can be utilised in information transport [72]. A variety of device architectures are currently being explored including, π Josephson junctions [17–20], long range proximity effects in nanowire systems [73], and spin valve structures in which the level of magnetic inhomogeneity can be tuned and the effects on the superconducting state observed [74–81]. All of these device based studies require an acute understanding of the physics occurring at the interfaces and the effect of each material component within the system. In many cases this is challenging to uncover and to directly measure. The work presented within this thesis aims to examine the fundamental proximity effects occurring at normal metal - superconductor and ferromagnet - superconductor interfaces to address a number of previously anomalous results within the field of S/F hybrid systems [39, 60, 82]. The work performed, both as part of this study [60, 83, 84] and others [40–42, 85], have resulted in a step-change in understanding of these systems and highlighted the importance of newly described electromagnetic effects both in the interpretation of experimental data and in future device design.

The first experimental study, presented within chapter 3, follows on from the work published in reference [39] where an anomalous magnetic flux lowering was observed within the normal metal layer of an NSFnF sample structure with n being a thin metallic spacer layer. The degree of the measured flux lowering was reported to be dependent on the level of non-collinearity between the two ferromagnetic layers and could not be explained within the existing theory framework at the time of publication. In a bid to understand and uncover the origins of this effect a simple study of S, NS and NSF sample structures was carried out to disentangle the various contributions to the observed flux profile. The results of this study [60] form the basis for chapter 3, the main findings of which prompted the parallel development of a new theory of electromagnetic proximity [40–42]. Subsequent experimental work [83, 84], presented within chapters 4, 5 and 6 of this thesis, seeks to test this new theory within a variety of NSF thin film structures composed of a range of different materials. The overall findings support the proposed theory of the electromagnetic proximity effect though its precise origin within these S/F thin film systems remains an important open question.

In order to probe the desired physics within a thin film environment such that the experimental aims can be met, a local and appropriately sensitive probe of the magnetic flux across a thin film is required. The work presented in this thesis uses low energy muon spin rotation (LEμSR) to map out changes to the flux profile induced by the presence of different material layers. Through systematic experiments, a full spatial analysis of the acquired data is possible *via* application of a procedure which will be discussed within chapter 2. The technique of LEμSR, as is hopefully demonstrated through the work presented here, is a key tool for understanding these superconducting proximity systems and has been used extensively to this end (see for example [32, 38, 39, 60, 83, 84]).

2 | Experimental Techniques

This section seeks to give an overview of the experimental techniques and data analysis methods applied within this thesis. Details of the measurement systems used will be given where appropriate but it is neither intended to be an exhaustive reference nor a technical manual. The aim is to provide only the necessary experimental context with which to interpret the results and an attempt to be as succinct as possible in achieving this aim will be made.

2.1 Low energy muon spin rotation

This first subsection concerns itself with low energy muon spin rotation (LEμSR); a technique with which one can probe, amongst other things, the magnetic flux profile across a sample, and which has therefore, proven central to the experimental studies presented here. This section will by no means capture the full range of possible applications of LEμSR but rather serves as a basis from which the subsequent experimental chapters will be built.

2.1.1 Surface muon production

The positive muon, μ^+, is an unstable spin-$\frac{1}{2}$ lepton of charge $+e$ with a lifetime $\tau_\mu = 2.197\ \mu s$. Although a second species of muon with charge $-e$ also exists, in what follows we will only consider the positive variant and so choose to drop the label, referring to μ^+ particles simply as muons as in [86].

The surface muon is produced as a result of the parity violating decay of the positive pion, π^+, which is mediated by the weak interaction

$$\pi^+ \rightarrow \mu^+ + \nu_\mu \ . \tag{2.1}$$

The parity violating nature of the decay shown in equation 2.1 is crucial to the muon's usefulness as a local magnetic probe since it ensures the production of a nearly 100% spin polarised beam. In the decay process at rest, μ^+ and the muon neutrino, ν_μ, must be emitted in opposite directions and with antiparallel spins to conserve momentum and intrinsic angular momentum respectively. As a consequence of parity violation in the weak interaction the spin of the ν_μ will be antiparallel to its momentum; this fixes the spin of the corresponding muon. Since muons produced in pion decay at rest are emitted isotropically, for any given direction in space a beam of muons will therefore be produced where the spin vector is antiparallel to the momentum. This process is illustrated in figure 2.1. Additionally, in the pion rest frame, upon production the muons all possess a kinetic energy of $E_\mu = 4.1\ MeV$. The result is a monochromatic spin polarised beam [87].

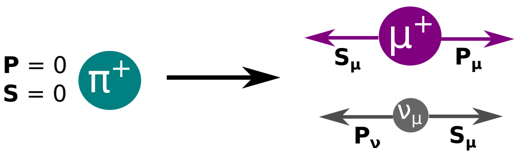

Figure 2.1: A schematic diagram of a pion decaying into a muon and muon neutrino. Since the pion decays at rest and has zero total spin, and the neutrino spin and momentum is fixed by parity violation, the resultant muon is produced with its momentum vector opposite to its spin.

Following production these muons can be put to use as highly sensitive and versatile local magnetic probes within condensed matter systems [86–89]. This is possible owing to their kinetic energy corresponding to penetration depths of only fractions of millimeters in solid materials and to their well defined spin direction. Muon spin rotation/relaxation/resonance (μSR) techniques all involve the implantation of muons into a host material and the subsequent monitoring of the time evolution of the muon spin within that environment.

2.1.2 The muon as a local magnetic probe

Upon implantation into a material a muon will rapidly thermalise, whilst preserving its initial spin direction, before Larmor precessing around the local magnetic field, B_{loc}, at a frequency given by $\omega_\mu = \gamma_\mu B_{loc}$, where $\gamma_\mu = 2\pi \times 135.5\ MHzT^{-1}$ is the muon gyromagnetic ratio. Since the muon is itself unstable it will decay, with a lifetime of $\tau_\mu = 2.197\ \mu s$, into a positron. The angle, ϕ at which the positron is emitted with respect to the momentary muon spin direction is governed by the probability distribution given by equation 2.2 where a is an energy dependent asymmetry factor taking an average value of $\frac{1}{3}$:

$$W(\phi) = 1 + a\cos(\phi)\ . \tag{2.2}$$

$W(\phi)$ has its maximum where positron emission takes place along the muon spin direction at the moment of decay [87]. A schematic diagram of the decay process, and subsequent positron detection, is shown in figure 2.2. A muon enters the experiment at t_0 and with an initial spin angle θ_0. The muon spin will then begin to process about the local field to a new angle θ where $\theta(t) = \omega_\mu t + \theta_0$. At any given time, t, the chance the muon will decay into a positron is given by $\frac{1}{\tau_\mu}e^{-t/\tau_\mu}$. Through detection of the resultant positron and knowledge of the time span of the event, the evolution of the muon spin direction can be tracked and information about the local field experienced established. This requires knowledge of a statistically significant number of single muon events each with an identical starting condition. Hence the importance of a spin-polarised monochromatic muon beam [90].

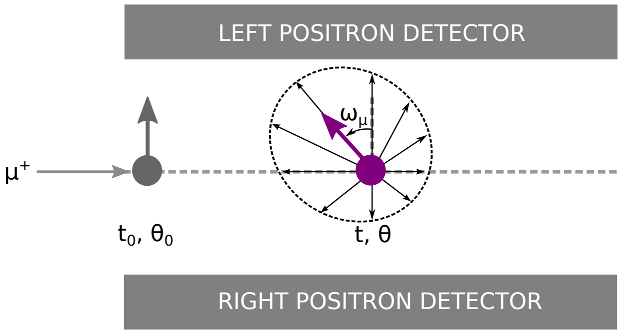

Figure 2.2: A schematic diagram of the basic principle of μSR. A muon enters the apparatus at t_0 with an initial spin angle θ_0 (grey arrow). At some later time, t, the muon spin has rotated about the local field to an angle θ (purple arrow) and decays emitting a positron preferentially along θ.

In order to monitor the spin rotation of the muon ensemble two positron detectors are positioned either side, in this case in the left and right directions, of the sample space. The number of positron events detected on either side can then be counted as a function of time. The resultant time spectra $N_L(t)$ and $N_R(t)$, given by equation 2.3, encode the information about the time evolution of the muon spin polarisation along the detection axis [86].

$$
\begin{aligned}
N_L(t) &= N_{0,L} \exp\left(-\frac{t}{\tau_\mu}\right)[1 + A_0 P(t)] \\
N_R(t) &= N_{0,R} \exp\left(-\frac{t}{\tau_\mu}\right)[1 - A_0 P(t)]
\end{aligned}
\tag{2.3}
$$

N_0 is the total number of muon events and $A(t) = A_0 P(t)$ is the asymmetry spectrum which is defined as the normalised difference between the two detector signals as in equation 2.4 where α is an efficiency parameter with a value close to unity.[11]

$$
A(t) = A_0 P(t) = \frac{\alpha N_L(t) - N_R(t)}{\alpha N_L(t) + N_R(t)} \tag{2.4}
$$

The maximum observable asymmetry between the two detectors is parameterised by A_0 the upper limit of which is set at $\frac{1}{3}$ by the intrinsic asymmetry of the muon decay. In practice A_0 is often lower and depends on the precise details of the experimental configuration and the energy distribution of the emitted positrons [90]. Typically, for the measurements presented in this thesis, A_0 is of the order of 0.20.

The main panel of figure 2.3 shows an example raw μSR time spectrum where the signals from the left and right detectors have been plotted separately in blue and red respectively. The signal shows periodic maxima and minima as the muon spin is directed towards or away from the relevant detector. This oscillatory component is then modulated by an exponential decay associated with the muon lifetime. The inset of figure 2.3 shows the corresponding asymmetry spectrum, $A(t)$, plotted in green. Here the oscillation frequency scales with the local field that the muon ensemble experienced. At t_0 the maximum asymmetry is measured, in the example shown this is about 20 %, but for $t > t_0$ there is some loss of the asymmetry amplitude. This damping is caused by depolarisation due to the presence of a distribution of internal fields and is represented in the inset by the

---

[11] In practice this depends on the precise experimental configuration and is related to the beam alignment with respect to the two detectors. Please see section 2.1.4 for further details.

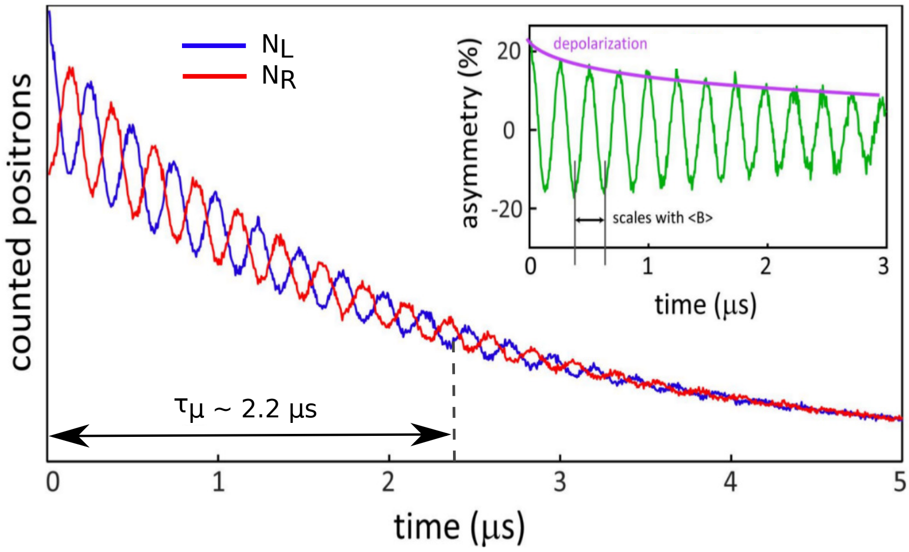

Figure 2.3: Main panel: an example μSR time spectrum with the counts from each detector plotted separately where N_L and N_R are shown in blue and red respectively. The exponential decay in the signal is due to the muon lifetime τ_μ. Inset: the corresponding asymmetry spectrum is plotted in green. The oscillation period in the signal scales with the average field that the muon ensemble experienced and the damping, represented by the magenta envelope, scales with the muon depolarisation.

magenta envelope. $A(t)$ contains all of the information pertaining to the local magnetic environment experienced by the implanted muons. In order to extract this information, one is required to fit the spectrum with an appropriate functional form which will depend on the precise experimental configuration [86].

2.1.3 The transverse field geometry

There are many different ways in which to configure a μSR experiment. In general, the experimentalist has control over the detector arrangement, applied field magnitude and orientation and the initial spin polarisation of the muon. Each configuration often lends itself to probing a specific subset of the physics of a system. For all of the studies presented here the measurements were carried out in the transverse field (TF) geometry since the aim was to probe the Meissner state of thin superconducting samples. In what follows we will therefore focus on the specifics of this TF geometry and the reader is directed to [86–88] for detailed information on alternative measurement geometries.

A schematic of the TF geometry adopted for the measurements pre-

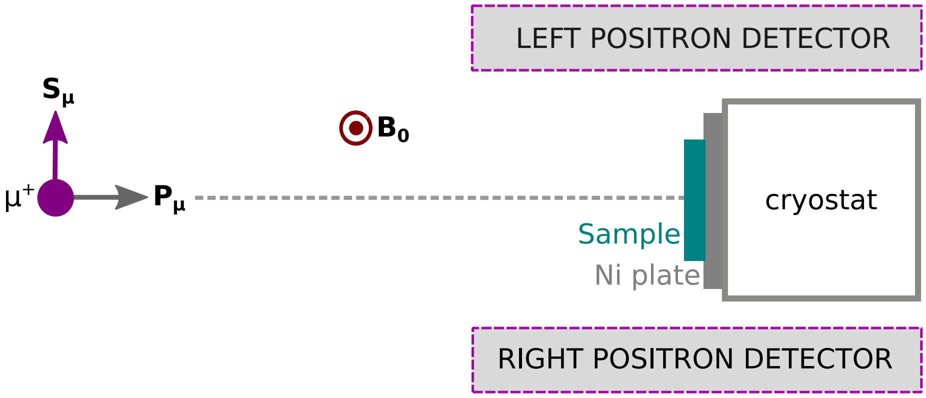

Figure 2.4: A schematic diagram of the transverse field configuration. The incoming muons have their spin polarisation in the plane perpendicular to a weak applied field B_0. This results in the muon spin precessing about the applied magnetic field.

sented here is shown in figure 2.4. In this geometry the incoming muons have their spin polarisation in the plane transverse to a uniform applied field. For the measurements contained within later chapters the applied field, B_0, was typically set to 300 Oe. The precession of the muon spin then occurs about B_0 such that the relevant pair of detectors are those situated to the left and right of the sample space. It is also important to note that owing to their high kinetic energies (around 30 MeV), the emitted decay positrons easily pass out of the sample and through a complex environment such that they are intercepted by the positron detectors. Within any μSR experiment there will always be some fraction of muons which do not stop in the sample but instead in the sample holder. In a TF experiment any resulting background contribution can be negated by using a nickel mounting plate. This is because the strong ferromagnetism rapidly depolarises any muons which land in the plate before the data collection window begins and therefore they do not contribute to the detected asymmetry signal.

2.1.4 Low energy muons

As discussed in section 2.1.1 the muons produced from pion decay result in a monochromatic beam of $E_\mu = 4.1\ MeV$. This typically corresponds to a material penetration depth of a few tens of millimeters which is ideal for the study of many condensed matter systems. In some cases, however, it is advantageous to be able to moderate E_μ to lower values whilst still benefiting from the properties of muons as local magnetic probes. This allows both the study of thin samples and, where a fine control of the incoming muon kinetic energy can be achieved, makes depth dependent measurements possible [90, 91]. Such low energy muon spin rotation (LEμSR)

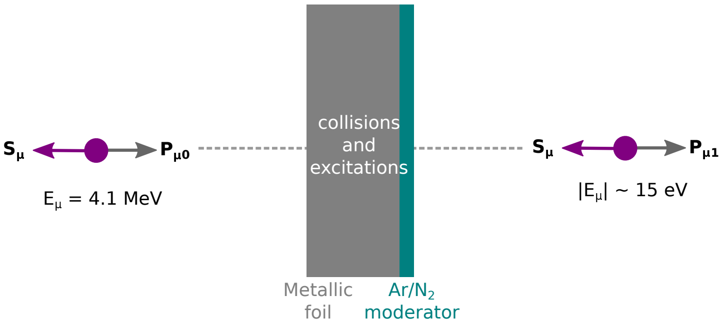

Figure 2.5: Moderation of surface muons to lower energies. The incoming muons of $E_\mu = 4.1\ MeV$ are incident on the moderator and through a combination of Coulomb collisions with the foil and subsequent excitation processes within the noble gas film are brought to an average final E_μ of around 15 eV with their spin polarisation preserved.

measurements are currently only possible on the *low* energy muon beamline at the Paul Scherrer Institut [92]. The principles of the measurement remain the same but with the muon energy becoming an additional degree of freedom which must be accounted for in the data analysis. As stated in the introduction to section 2.1 it is this low energy flavour of μSR which has been central to the work presented here.

The generation of low energy muons begins with the moderation of a surface muon beam. This is achieved through interaction with matter [93]. In particular, incoming muons are incident on a thin moderator film composed of solid noble gases. A layer each of Ar(10 nm) and N_2(1.2 nm) is grown atop a 100 μm metallic foil and held at 10 K as shown in figure 2.5. Incoming surface muons are incident first on the metallic foil where, through a series of Coulomb collisions and ionisation events, they rapidly lose energy down to the keV level and additional energy loss mechanisms begin to kick in. These include the formation and subsequent break up of muonium (μ^+- e^- pairs) within collisions. Dissipation continues efficiently until the muon energy becomes comparable with the threshold energy for these processes. In a noble gas film this occurs when $E_\mu \leq 20\ eV$ at which point the muon is then able to escape the moderator. The distribution of resultant energies for an argon moderator, for example, is strongly peaked at around 15 eV with a small tail extending up to high energies. This whole process occurs on the ps timescale *via* mechanisms which have a negligible effect on the muon spin polarisation.

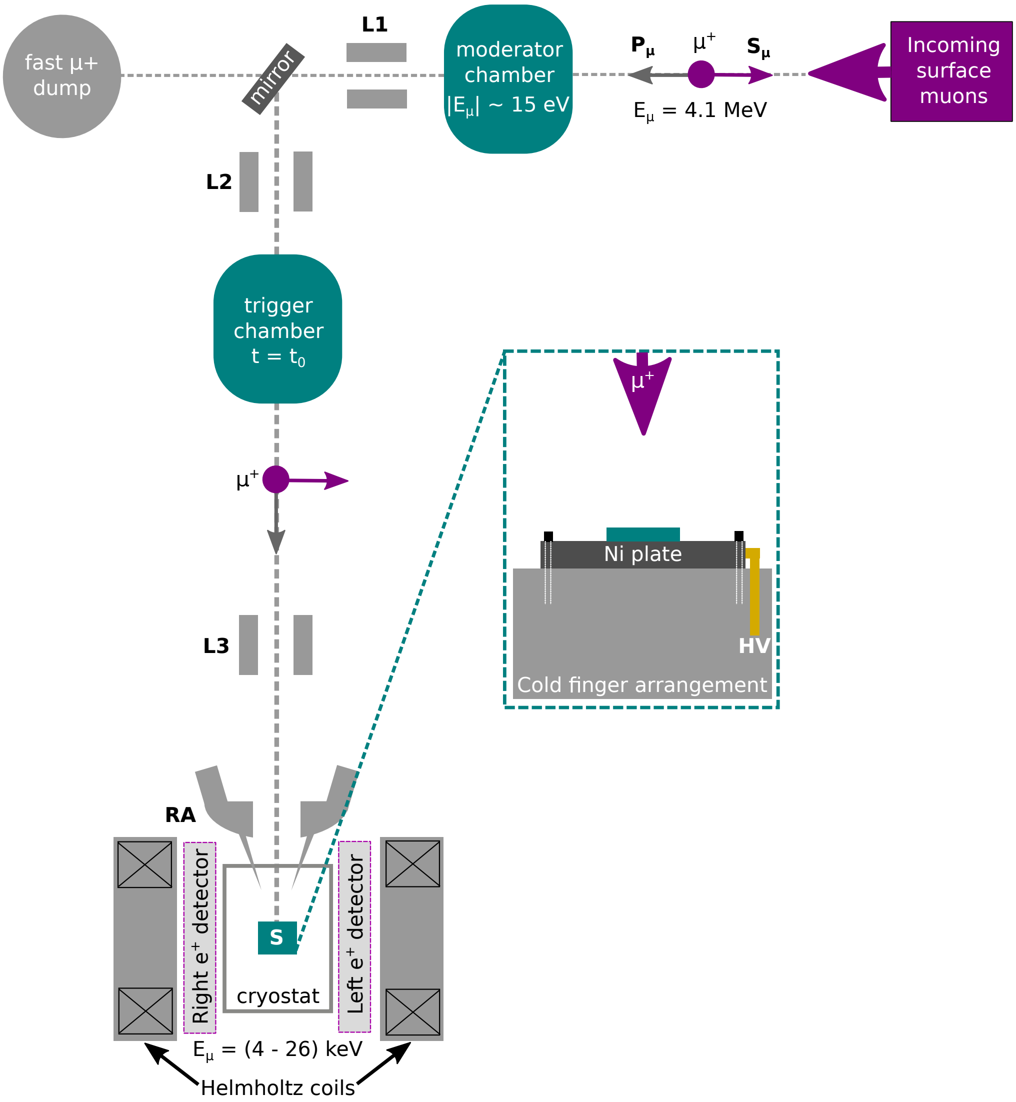

Figure 2.6: A schematic of the low energy muon beamline at PSI. Surface muons enter the beamline at the top right hand corner before being moderated to low energies and transported to the sample space. LX represent the electrostatic Einzel lenses which focus and steer the beam and RA the conical electrostatic lens that focuses the beam down to the sample. The inset shows a close up of the sample, indicated in the main panel by S, where HV represents the high accelerating voltage with which E_μ is set.

Once the muons have been moderated they must be tuned to the desired energy and transported to the sample space. Thankfully the muon is a charged particle so this is possible through the application of accelerating and beam steering electric fields. Figure 2.6 details how this is achieved on the LEM beamline at PSI where the measurements were performed [90, 91].

Upon entering the beamline a fraction of the surface muons become trapped within the moderator shield where they are converted to lower energies as previously described. The slow muons are then accelerated to a transport voltage, usually set to around 15 kV, before passing out of the moderator chamber. Since the muons are charged the beam transport is controlled by electrostatic Einzel lenses, indicated in figure 2.6 by "LX", which act to direct and focus the beam. The muons are then incident on an energy dependent reflecting mirror which directs only the slow muons down towards the trigger chamber leaving the fast muons to be discarded in the fast μ^+ dump. Within the trigger chamber the muons encounter a thin carbon foil causing the emission of electrons which can then be directed to a microchannel plate detector. It is this detection which starts the single muon event. A single measurement event then continues until a positron is detected at one of the active positron detector arrays within the sample chamber. The average rate at which muons pass through the trigger chamber is around 850 s^{-1}. This gives an interval of approximately 1 ms between muon events. Given that this is much longer than τ_μ it is highly unlikely that two events will occur simultaneously within the apparatus however should this happen, or a time interval greater than 12.5 μs pass without positron detection, the events are discarded.

From the trigger chamber the muons progress through into the sample space where they are steered onto the sample by a conical electrostatic lens arrangement. These voltage tuned ring anodes (RA) are responsible for compensating the magnetic field in the sample space, which due to the Lorentz force would act to deflect the muon beam, and so the high voltages around the beam need to be adjusted depending on the precise measurement conditions. In the transverse field arrangement described in section 2.1.3, for example, this involves tuning the left and right RA voltages to optimise the position of the beam spot with respect to the left and right positron detectors. Ideally the beam should be aligned such that it is exactly in the middle between the two detectors. In practice, however, there will always be a small misalignment which must be accounted for by weighting one of the detector signals, using a fixed parameter conventionally labelled α, with respect to the other. The inset of figure 2.6 shows a close up of a sample *in situ* mounted on a nickel plate as described in section 2.1.3. Importantly, the sample plate is electrically isolated from the environment such that, *via* a high voltage lead (HV), the sample voltage can be tuned through a range of ± 12 kV to either accelerate or deccelerate the incoming muons. This allows the experimenter to select an appropriate muon energy, within the range $(4 - 26)$ keV such that the implantation depth of the muon within the sample can be manipulated as desired [91]. This allows the study of, for example, magnetic flux profiles across thin films or regions around buried interfaces both of which are unique features of LEμSR.

In addition to altering the muon energy it is also possible to measure both as a function of applied magnetic field and temperature. On the LEM beamline, for example, the applied field can be tuned over the range $(0-300)$ Oe in the TF geometry for continuous measurement. With respect to temperature control, whilst the sample is electrically isolated from the environment it is kept in excellent thermal contact to a cold finger arrangement. This allows a base temperature of around 2.3 K to be reached and opens up the possibility to study low temperature states of matter.

2.1.5 Stopping profiles and muon implantation: building up a spatial profile

Implantation of a muon is dependent on the muon energy and the properties of the material into which it is being implanted. In cases where the sample is homogeneous the precise stopping location of the muon is not important. For the study of layered thin films composed of multiple and very different elements, however, it is necessary to know where in the sample on average a muon of fixed energy is probing. This can be calculated by a well proven Monte Carlo algorithm [93, 94], available at the beamline, which determines a step-by-step trajectory for the muon as it slows down within a given sample. By calculating this trajectory, and thus the final stopping position, for a large number of implanted muons of fixed energy a distribution of where the muons are likely to stop can be built up. Figure 2.7 shows an example of these so-called muon stopping profiles for a simple Cu(40)/Nb(50)/Co(2.4) trilayer, grown on a silicon substrate, where the brackets indicate the layer thickness in nanometers. These were calculated using an ensemble of 100000 muons and are plotted for a selection of possible measurement energies. The probing depth, plotted on the x-axis, is measured relative to the top surface of the sample and the y-axis represents the fraction of muons which stop at a given depth. For a muon energy of 4 keV all muons stop within the Cu(40) layer. As the muon energy increases the stopping

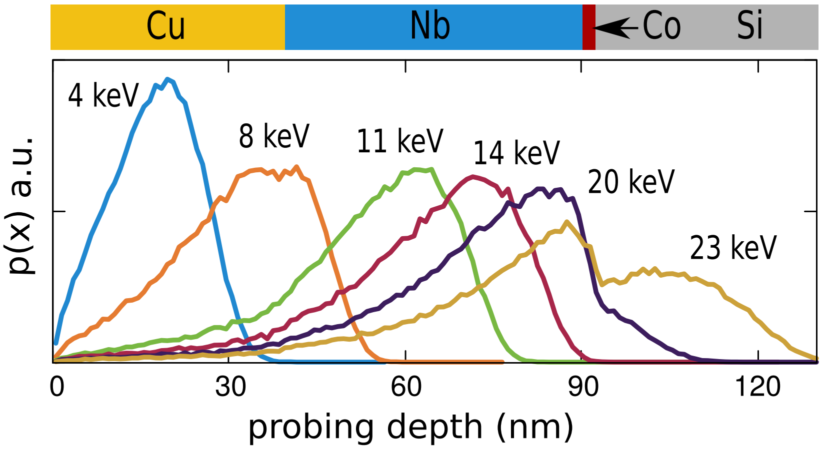

Figure 2.7: Muon stopping profiles for a set of select muon energies plotted for a Cu(40)/Nb(50)/Co(2.4)/Si sample. The bar at the top indicates the sample structure relative to the x-axis.

distribution shifts to higher depths whilst a tail always remains within the copper. In general an increase in muon energy results in a broader stopping profile and hence lower resolution spatial information.

Ideally, the local magnetic environment is uniform within the plane of the sample such that by tuning the muon energy a slice of information, averaged over the stopping profile, can be gleaned. A typical measurement then involves scanning the muon energy, where for each energy a spectrum of around 3 million events is collected, such that the average field as a function of the energy can be determined. Through knowledge of the stopping profile this can then be converted to an average field as a function of the average probing depth. This gives an indication of the spatial profile of flux across the sample.

2.1.6 The conventional approach to data modelling for a transverse field LEμSR experiment

This section details how to model the raw data for a typical transverse field LEμSR experiment on a superconducting thin film sample and serves as a basis for the analysis presented in each of chapters 3-6.

Section 2.1.2 described how, through monitoring the direction and timing of decay positrons, it is possible to follow the spin of a muon ensemble as a function of time. In order to extract the desired physical quantities from the resultant spectrum an appropriate model function needs to first be selected and fit to the data. In the case where the applied field is much larger than the internal fields it is possible to model the raw detector data,

$N_{L/R}(t,E)$, using the form shown in equation 2.5 where $K_{L/R}$ are time independent background contributions

$$\begin{aligned} N_L(t,E) &= N_{0,L}\exp\left(-\frac{t}{\tau_\mu}\right)[1-A(t,E)]+K_L\ , \\ N_R(t,E) &= N_{0,R}\exp\left(-\frac{t}{\tau_\mu}\right)[1+A(t,E)]+K_R\ . \end{aligned} \tag{2.5}$$

An energy dependence has now been acquired when compared with equation 2.3 since the average stopping depth, and hence potentially the local magnetic environment, can be tuned with the incoming muon energy. The quantity of interest is the asymmetry $A(t,E)$, now also energy dependent, which holds all the information about the field distribution. The form of $A(t,E)$ for the measurements presented in chapters 3-6 is given by equation 2.6:

$$A(t,E) = \int_0^{x_{max}} dx\ A_0 p(E,x) G(t,E)\cos\left[\gamma_\mu B(x)t+\phi(E)\right]\ . \tag{2.6}$$

To account for the stopping distribution of the muons, $A(t,E)$ must now be weighted by the relevant stopping profile, $p(E,x)$, and integrated over its spatial extent ($0 \leq x \leq x_{max}$) where x is measured normal to the sample surface. The cosine describes the Larmor precession of the muon spin ensemble about the average local field ($B(x) = B_0 + B_{internal}$), A_0 represents the amplitude of the signal at time t_0 and $G(t,E)$, the depolarisation function, encodes the information about the distribution of fields that the muons encounter within the sample. For a perfectly uniform field distribution $G(t,E) = 1$ but in general there will always be some source of field inhomogeneity such that $G(t,E) < 1$. This can take many forms but is commonly related to nuclear dipole moments or stray fields across the sample [86]. Importantly for superconducting films any flux gradients associated with Meissner expulsion will also play a role in depolarising muons resulting in an enhanced damping of the signal below T_c when compared with the normal state. The sources of depolarisation within the superconducting thin films studied here are well described by the general form of damping given by equation 2.7:

$$G(t,E) = G_0\exp\left(-(\lambda(E)t)^\beta\right), \quad \text{with}\ \ 1 \leq \beta \leq 2\ . \tag{2.7}$$

The β parameter allows for the exponential describing the damping to be "stretched" between a Lorentzian ($\beta = 1$) and a Gaussian ($\beta = 2$) form for the envelope. The depolarisation rate, $\lambda(E)$, can be a strong function of energy. This is generally true for layered samples where the material parameters vary as a function of the probing depth. In the case of structures with buried ferromagnetic layers, for example, λ can rise very sharply as the average probing depth approaches the magnetic layers. This being due to increased sampling of the stray fields [39].

Once the appropriate model functions have been selected they must be fit to the raw detector data where a standard Levenburg-Marquardt algorithm is applied to optimise the fit[95].[12] This is conventionally achieved by assuming all variables are constant over the spatial extent of a stopping profile. As is apparent in figure 2.7, this is more accurate at low probing energies where the stopping distributions are strongly peaked, therefore sampling over a narrower region, and confined to a single material layer. Based on this assumption, the detector histograms for all muon energies can then be fit separately with equation 2.5 using the appropriate forms for $A(t, E)$ and $G(t, E)$ shown in equations 2.6 and 2.7 respectively. This allows the average field as a function of the muon energy, $\langle B\rangle(E)$, to be extracted. A conversion between energy space and a spatial profile can then simply be achieved by calculating the average probing depth, $\langle x\rangle$ corresponding to a given muon energy. This finally allows a plot of $\langle B\rangle(\langle x\rangle)$ to be produced. Whilst clearly an approximation, this approach does give an indication of the underlying flux profile and is an excellent starting point to a full analysis of the data.

Given the large parameter space of the model used it is important to take a structured and well constrained approach to the data analysis which is appropriate to the physical system being studied. Many of the parameters can be linked, constrained or fixed across all measurement energies for a given system. For example, during the set up of an experiment a value for α, the signal weighting parameter associated with the lateral beam offset, can be determined at the beam optimisation step.[13] This parameter can

---

[12] Please see Appendix A for further details of the Levenberg-Marquardt algorithm.

[13] α is determined by applying a weak transverse field and fitting the resultant spectrum. It should be as close to 1 as possible whilst maintaining a maximum signal amplitude (A_0). For our measurements optimal alignments typically gave $0.99 \leq \alpha \leq 1.01$.

then be fixed for all subsequent measurements at the same field providing the sample position does not change. Although in principle the starting phase of each muon, ϕ_0, should remain constant in practice there can be a small variation between sets where the starting time, t_0, is different. t_0 is determined by the beam transport settings so where these are fixed ϕ_0 should remain fixed to good approximation.[14] The parameters $N_{0,L/R}$ and $K_{L/R}$ depend on the particular run, since they are related to the signal amplitude, and need to remain as free fit parameters across measurement sets. This is also true of the field, B, depolarisation rate, λ, and β parameter which may, depending on the sample, change as a function of depth and temperature.[15] In each case the resultant fit parameters will be averaged over the spatial width of the stopping profile. Depending on the particulars of the sample this can be less than ideal.[16]

In each of chapters 3-6 the systems studied are superconducting thin films with some combination of normal metal and ferromagnetic materials in contact with them. The properties of each material layer will be very different and many of the parameters change strongly as a function of temperature and probing energy. In each case the sample is measured at each muon energy above and below its superconducting transition temperature T_c. The normal state fit is found and can be used as an input to the superconducting state spectrum providing a good initial guess for all parameters. This allows any observed difference to be directly related to the superconductivity as opposed to, for example, fluctuations in the background field across the sample. It also allows any temperature independent parameters to be fixed to their normal state values in an effort to constrain the fit.

Figure 2.8 shows an example set of LEμSR data for the simple trilayer sample from figure 2.7.

---

[14] For the majority of our measurements we used fixed transport settings of 15 kV on the moderator. Where the accessible tuning range of the sample high voltage is not sufficient to achieve the desired muon energy, however, it is necessary to play with these settings and account for the different ϕ_0 in the corresponding fits.

[15] In practice for our samples it is possible to fix β across all measurement sets taken at a given temperature. This is material dependent but often takes a value within the range $1.2 \leq \beta \leq 1.7$.

[16] This is particularly true for the λ parameter in layered systems (especially where ferromagnets are involved since they can generate strong stray fields). In such cases a model profile can be imposed to allow λ to vary spatially in a controlled way. Further information can be found at the end of the present section where this is discussed in detail.

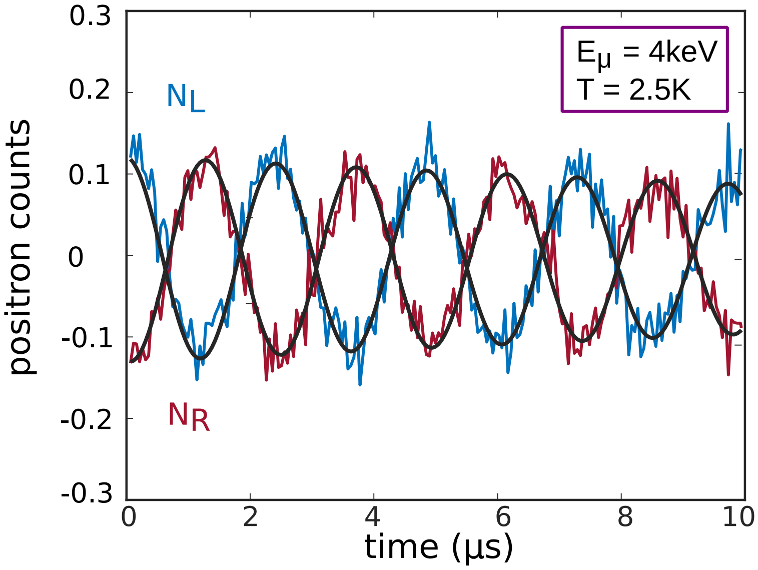

Figure 2.8: Positron detector data plotted for a Cu(40)/Nb(50)/Co(2.4)/Si sample, where the bracketed numbers indicate the layer thickness in nm, measured at 2.5 K using a muon energy of 4 keV. The left and right detector data are plotted separately in blue and red respectively. Also shown are the resultant best fits as solid black lines with $\chi^2 = 1.03$.

Table 2.1: Selected parameters for the example LEμSR fit displayed in figure 2.8.

α	β	ϕ_0 (rad)	A_0 $(\%)$	λ (MHz)	B (G)
1.088 ± 0.002	1.61 ± 0.05	-10 ± 1	13 ± 0.2	0.65 ± 0.06	293.4 ± 0.1

The data are plotted separately for the left (N_L) and right (N_R) positron detectors in blue and red respectively. In each case the solid black lines show the fit to the data, with a $\chi^2 = 1.03$, with the corresponding fit parameters shown in table 2.1. The measurement was conducted in an applied field of $B_0 = (302.8 \pm 0.1)$ Oe, as found from the corresponding normal state fit, and at a temperature and muon energy of 2.5 K and 4 keV respectively. The χ^2 value reflects that the model fit is an appropriate choice for the data set which can also be seen simply from looking at the raw data. As expected the α parameter is close to one which suggests the beam is well centred.

If one refers back to the stopping profiles in figure 2.7 then clearly for $E_\mu = 4$ keV all of the information is coming from the proximitised Copper layer. Seeing as the measurement temperature is below T_c a small Meissner screening response would be expected. Table 2.1 shows the average measured field is $B = (293.4 \pm 0.1)\ G$ which when compared with the value of B_0 shows there is clear diamagnetic screening in the superconducting state. The superconducting state value of λ also reflects the flux expulsion since there will be flux gradients that act to damp the signal more strongly than in the normal state.[17]

The example measurement in figure 2.8 provides a relatively clean illustration since the damping is low and the muons of $E_\mu = 4\ keV$ only sample a single layer. In cases where the stopping profile extends over two very different regions of a sample, however, it is possible to model the data more thoroughly by allowing the fit to be constructed from weighted sampling across the different layers. This is particularly useful when dealing with "step-changes" in material parameters, for example across the interface of an NS bilayer, where a simple spatial profile in λ can be imposed which reflects this step function. In more complicated situations where the change is continuous across the sample it may be appropriate to select a more complex profile. Within a layered sample, for example, whenever a ferromagnet is involved the associated stray fields result in much stronger damping that can decay across the full spatial extent of the sample. In such cases it is appropriate to model the depolarisation rate as an amplitude originating at the centre of the ferromagnetic layer that decays away exponentially on both sides as in equation 2.8

$$\lambda(x) = \lambda_0 \exp\left(-\frac{x}{\xi_\lambda}\right) , \tag{2.8}$$

which was deduced empirically for the S/F thin film systems measured within this thesis [39]. The depolarisation is characterised by an amplitude (λ_0) parameter and a characteristic decay length (ξ_λ). By allowing a constrained spatial variation of λ a more accurate fit to the data can be achieved. It is, however, now necessary to fit all of the data for a given temperature and field simultaneously such that the profile best describes the full set. Examples of both the step function and exponential form of modelling λ can be found in chapter 3 where it is used when modelling

---

[17] The corresponding normal state value was $\lambda = (0.35 \pm 0.04)\ MHz$. This will represent some combination of the nuclear depolarisation within the Copper and some background stray fields extending out from the Co layer.

Meissner screening in simple S, NS and NSF systems.

By fitting the full set of measured energies, as described in the example above, the average field profile can be extracted. In cases where the underlying profile is known however, in a similar way as for the λ parameter it is possible to impose the analytical form of $B(x)$ on the measured data in order to obtain a best fit profile for all measurement energies simultaneously. This gives access to a full spatial description of the system and often allows physical parameters to be extracted from the data.

2.1.7 Imposing the underlying field profile in an LEμSR experiment

As mentioned briefly in section 2.1.6 it is possible to impose an analytical form of $B(x)$ on a measured set of LEμSR data as seen in, for example, [60, 83]. This has the advantage of reconstructing the full spatial dependence from the average and allows physically relevant parameters to be extracted. This section highlights the important considerations to be made when applying this method and gives some example model profiles for superconducting thin films.

In the conventional analysis of low energy muon data it is assumed the field from which muons are sampling is constant across the width of the stopping profile. This, as previously described, allows the average field profile to be extracted and where sufficiently many energy points are sampled[18] can give a good indication of the underlying behaviour. This is particularly useful in situations where the sample is highly complex or where there is no initial expectation of what the full spatial profile ought to be. In reality, there are many field profiles which could result in the same average flux and so some amount of caution is required if and when interpreting the spatial information further. This is illustrated by the schematic in figure 2.9 where several possible underlying profiles (dashed lines) for the resultant average are shown plotted together. In general, one can always employ physical reasoning to eliminate some possibilities but this is not always accurate and will still leave many potential solutions. One might also try to identify the most likely profile by carrying out a χ^2 analysis on the fit results of imposing

---

[18] The number of measurement points required for a given sample depends on how slowly varying the underlying field profile is and on the spatial resolution of the stopping profiles.

several possible profiles as in [39]. This does not necessarily give a definitive solution, however, and care needs to be taken when comparing χ^2 values originating from fits of variable parameter number.

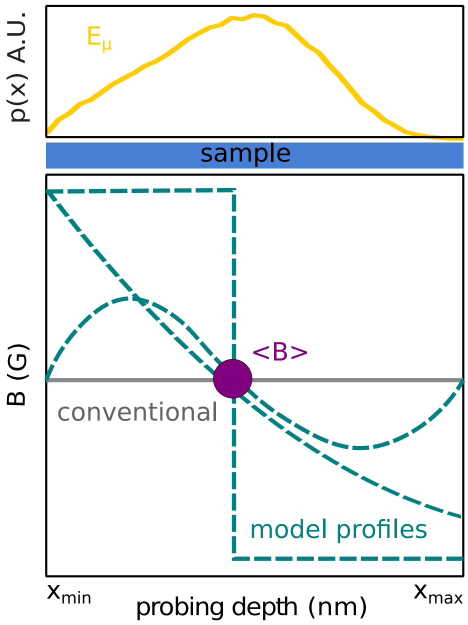

Figure 2.9: A schematic diagram of some possible underlying flux profiles for average LEμSR data. Top panel: A stopping profile for some arbitrary sample which extends over the range $x_{min} \leq x \leq x_{max}$. Bottom panel: Field as a function of probing depth. The grey line indicates the conventional approach to data analysis. The dashed lines are a selection of possible spatial profiles with $\langle B \rangle$ shown as the plotted point.

In cases where there is a supporting theory to motivate a specific choice of profile the average analysis can provide an indication of whether or not this choice is appropriate. For a thin film superconducting sample with vacuum interfaces, for example, the London theory provides the expected cosh form for the flux profile which is given by equation 2.9 [47, 96].[19]

$$B_S(x) = B_0 \cosh\left(\frac{x}{\lambda_L} - \frac{d_S}{2\lambda_L}\right) \cosh\left(\frac{d_S}{2\lambda_L}\right)^{-1}, \tag{2.9}$$

where λ_L is the London penetration depth, d_S is the thickness of the thin film superconductor and $x = 0$ corresponds to the top surface of the film. In general, for a given material in thin film format λ_L can be much longer than its bulk value. This is reflected in the amplitude of the screening that can

---

[19] The notation $\cosh(x)^{-1}$ will be consistently used throughout this thesis to refer to division by $\cosh(x)$.

build up at the centre of the sample. Within specific parameter regimes [58], as discussed within chapter 3, this Meissner profile can be easily extended to the modelling of an NS bilayer system simply by allowing for two different decay lengths, λ_{LL} and λ_{LR}, corresponding to the left and right of the minimum respectively as in equation 2.10:

$$B_{NS}(x) = B_0 + c\ e^{\left(\frac{-x}{\lambda_{LL}}\right)} + f(c)\ e^{\left(\frac{x-d_{NS}}{\lambda_{LR}}\right)} + g(c)\ . \tag{2.10}$$

The profile is now defined over the full thickness of the bilayer, d_{NS}, and $f(c)$ and $g(c)$ are chosen such that $B_{NS}(0) = B_{NS}(d_{NS}) = B_0$. This form of $B_{NS}(x)$ accounts for the possibility of an asymmetric screening profile associated with the two different materials and reduces to the simple London case where $\lambda_{LL} = \lambda_{LR}$. In principle, a numerical form of B_{NS} could be calculated using the quasiclassical theory but the analytical form given by equation 2.10 adequately describes the system.[20] The extension to include the effects of a ferromagnetic layer on the expected screening profile has proven not to be straightforward. Naively, one might expect the exchange field of the ferromagnet would act to break screening pairs within the region close to the superconductor-ferromagnet interface. The net result being an increase in λ_L and a corresponding reduction in the Meissner screening amplitude. A modified version of the bilayer profile given by equation 2.10 would then be an appropriate choice to describe the data. This is however not reflected in the experimental results presented within chapter 3. The discrepancies between theory and experiment have lead to a number of recent developments in the field. Most notably, the inclusion of electromagnetic phenomena at SF interfaces [40–42, 85]. A detailed discussion of this topic is given in the later experimental chapters.

Given an appropriate and justified choice for the analytical profile it then becomes possible to fit it to all the measured data simultaneously. In the case of equation 2.9 this would involve determining the value of B_0 from the normal state data, imposing the functional form on the superconducting state and tuning the value of λ_L such that the profile best describes the data. Where the chosen profile is a good description of the system this results in typical chi-squared values within the range $0.96 \leq \chi^2 \leq 1.06$. Once the best fit profile has been determined a final check can then be carried out by calculating the average values of $B(x)$ for each measurement energy, as

---

[20] Please see chapter 3, or reference [60], for further details.

in equation 2.11, and comparing these with the conventional data analysis which finds $\langle B\rangle(\langle x\rangle)$ directly from the raw data[21]:

$$\langle B(x)\rangle = \frac{\int_{x_{min}}^{x_{max}} dx\ p(x)B(x)}{\int_{x_{min}}^{x_{max}} dx\ p(x)}\ . \tag{2.11}$$

Here $p(x)$ is the stopping profile, for some fixed muon sampling energy, defined over the spatial range $x_{min} \leq x \leq x_{max}$. In general, the correspondence between the two methods is expected to be good where $B(x)$ is a fair description of the data.

---

[21] Note that a similar check can be carried out for the depolarisation rate modelling discussed at the end of section 2.1.6. This just involves making the same comparison but where the quantity of interest is now $\lambda(x)$ rather than $B(x)$.

2.2 Low temperature transport system

All the transport measurements were carried out in-house using a standard Cryogenic mini cryogen-free transport system.[22] This is of course advantageous in terms of cost, upkeep and maintenance and it has been a pleasure to work with this system over the past few years.

2.2.1 System specifications and stability

Within this section a brief description of the capabilities of the green cryostat transport system is provided. For technical details of the system the reader is referred to Cryogenic's technical manual of the instrument [97].

The main green cryostat system uses a GM cryo-cooler and Helium-4 compressor to cool both the superconducting magnet coils and the sample space mechanically down to temperatures of 1.6 K. The system in St Andrews is also equipped with a Helium-3 insert which extends the accessible temperature range all the way down to 300 mK. Combine this with the superconducting magnet coils, which can generate fields within the range $(-7 \leq B \leq 7)\ T$, and the result is a versatile and easy-to-use workhorse for investigating a range of different low temperature phenomena. The cryostat is interfaced with a Keithley current source and nano-voltmeter pair which provide the means to measure the transport characteristics down to a typical voltage noise level of 10 nV [98].

A great deal of effort has been invested into the ease of day-to-day running of this system. A full suite of custom software has been designed to operate all the standard measurement schemes (resistance-temperature (RT), resistance-applied magnetic field (RH) and upper critical field-temperature ($H_{c2}T$)) in a safe and reliable way. The temperature stability is routinely of the order $\pm 0.1\ mK$ with little evidence of thermal lag; making the system ideal for measuring sharp superconducting transitions.

2.2.2 Sample environment and connections

The samples of study in all later chapters are superconducting thin films of niobium which are usually in direct contact with normal metal and/or

---

[22] Owing to its colour this system is affectionately known as the green cryostat.

ferromagnetic layers. Their typical superconducting transition temperatures and upper critical fields sit within the range $(7.5 \leq T_c \leq 8.7)\ K$ and $(1 \leq H_{c2} \leq 3)\ T$ respectively and so are comfortably measurable with the green cryostat system. Here a brief description of the sample environment and connection procedure is provided for reference. Unless otherwise stated all transport data presented in the later chapters were collected under these conditions.

The thin film samples are grown, using DC magnetron sputtering, on simple silicon substrates of $(2 \times 2)\ cm^2$ in area. Given the limited size of the sample space in the green cryostat it is necessary to trim a small piece of the sample off using a diamond cutter.[23] The resulting sample is typically a bar of $(2 \times 8)\ mm^2$ in size which fits snugly on the standard sample holder. Once trimmed to size the samples are stuck down to the sample puck using glue and contacts made, in a standard 4-point arrangement [99], to gold-plated bonding pads. The inset on the right of figure 2.10 shows a schematic of the result.

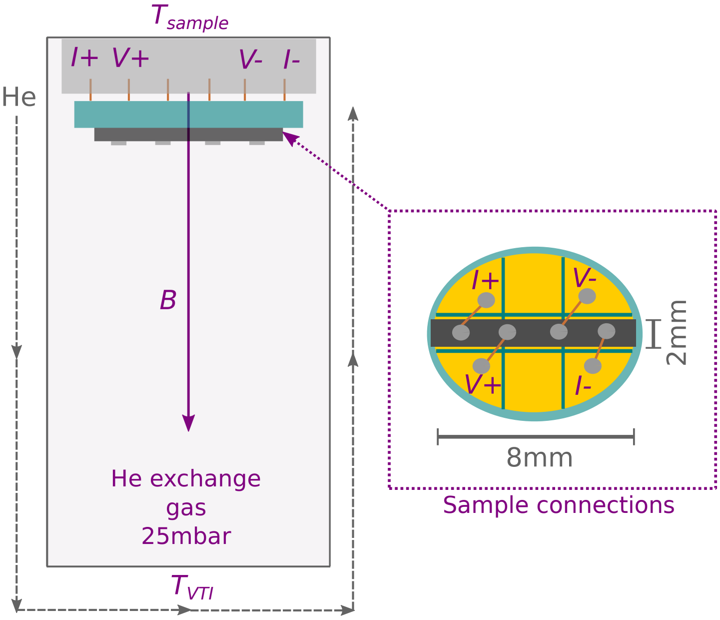

Figure 2.10: A schematic diagram of the green cryostat sample environment. The left panel shows a cross section of the sample space set up for He-4 operation. The applied field is perpendicular to the sample surface in the standard geometry. On the right a sketch of a typical sample in dark grey is shown with the usual 4-point connections indicated on the sample.

---

[23] In general, the measured segment is always cut from near the centre of the sample for consistency and to avoid any non-uniformity in film thickness at the edges. Needless to say this is performed after the LEμSR measurements have been performed.

The contacts are formed from a fine polymer coated cryogenic wire using the indium press method. The result is a durable low temperature contact.

The sample puck is gold-plated for thermalisation purposes and has a total of six conducting pads. Each pad connects to a corresponding pin which mates with a terminal on the sample probe. This is shown in the main panel of figure 2.10. These connections are then wired up to the Keithley current source and nano-voltmeter pair. A source current of $\pm 0.01\ mA$ is applied at $I+$ and collected at $I-$. The corresponding voltage measurement is taken across $V + V-$ using the low noise Deltamode feature [98]. It is important to note that such a low measurement current in known, from detailed tests, not to significantly effect the superconducting transition through heating.[24]

Once mounted up and connected to the Keithley arrangement the sample space is sealed and pumped out to high vacuum. A helium exchange gas pressure of 25 $mbar$ is used during standard operation to provide good thermal contact between T_{VTI} and T_{sample}. The cooling power is provided by the low pressure flow of He-4, regulated by a simple needle valve, around the outside of the sample space. At low system temperatures it then becomes possible to apply an external magnetic field. In the standard geometry this is perpendicular to the plane of the sample, as labelled by B in figure 2.10, though alternative sample holders can be used where a different orientation is desired.

---

[24] The tests found currents of up to 1 mA did not provide significant heating during measurements conducted on our thin film superconducting samples.

2.3 MPMS measurements

For those samples which contain ferromagnetic components it is important to characterise their behaviour in an applied field. It is useful to know, for example, what the magnetic state looks like at the muon measurement field and in cases where there are multiple ferromagnetic layers one might also like to know the different switching fields such that relative orientations can be tuned. Additionally, in chapter 5, where insulating oxide barriers were grown atop a ferromagnetic Co layer, it was important to look for any signs of cobalt-oxide formation since this is known to be antiferromagnetic and could have effected the physics of the overall system (see for example [100–103]). In all cases this was achieved simply by measuring MH loops in a standard Quantum Design Magnetic Properties Measurement System (MPMS) [104]. This section gives a brief overview of the procedure followed for these simple measurements.

2.3.1 MPMS measurement and data fitting

Within the MPMS system there is an arrangement of superconducting detection coils through which a magnetic sample can be passed; inducing an electric current. The coils are connected, *via* a superconducting wire to a SQUID sensor. The current generated in the coils by the passing magnetic moment is inductively coupled to the SQUID which when correctly configured produces a voltage directly proportional to the current flowing. In this sense the system operates as a highly sensitive current to voltage converter allowing magnetic moments of the order of 0.1 μemu to be detected [105]. The system in the lab in St Andrews offers the opportunity to measure over standard temperature and field ranges of $(2 \leq T \leq 400)\ K$ and $(-5 \leq B \leq 5)\ T$ respectively.

On the left of figure 2.11 a sketch of the internal coil configuration is shown. This comprises a set of three coils of superconducting wire: the top and bottom each being a single anticlockwise winding and the centre coil two clockwise windings as indicated. This configuration is known as a second derivative gradiometer and acts to reduce noise associated with variations in the flux density whilst still measuring the local changes in flux density associated with the moving dipole field of the sample.[25]

---

[25] In the ideal case any changes in the applied field due to relaxation of the magnet will

The sample, labelled in figure 2.11 by "S", is mounted on a rigid rod which is passed up and down along the axis of the coils over some scan length where the sample position is aligned with the centre of the coils at the centre of the scan window. The motion of the sample through the coils is controlled by a stepper motor and occurs in a series of discrete steps. A change in the sample position causes a change in the persistent current flowing within the superconducting coil, since variable flux will thread each loop, which in turn causes a change in the voltage detected at the SQUID sensor. At fixed positions along the scan length the sample is stopped and several voltage readings are taken and averaged. The signals on the right of figure 2.11 show the resultant voltage as a function of scan position, x, for the ideal case of a point magnetic dipole.

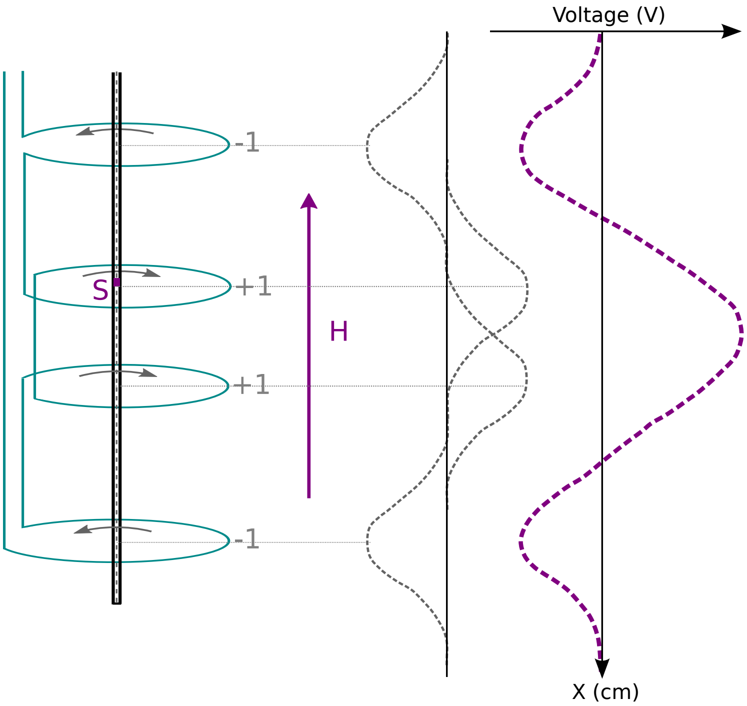

Figure 2.11: A schematic diagram of the SQUID magnetometer. On the left is shown the superconducting detection coils, a set of three, which are wired as a second-derivative gradiometer configuration. The arrows show the direction of the wire turn and S indicates the position of the sample on the quartz sample stick which passes up and down through the coils. H represents the externally applied field which can be tuned through ±5 T. On the right is shown the expected voltage signal for a point magnetic dipole passing through the coils. The total signal (purple dashed) is the sum of the separate responses from each of the coil winds (grey dotted).

---

be uniform and so the contributions from the clockwise loops will be exactly cancelled by those of the anticlockwise.

In grey dotted lines are presented the individual responses from each loop of the superconducting wire as the point magnetic dipole passes through. The superposition of these responses gives the total signal which in this case is represented by the purple dashed line. In order to observe this ideal signal the sample must be of uniform magnetisation and be of a size that is much smaller than the spatial extent of the detection coil. Alignment is also important since any lateral or angular offset will effect how the flux threads the coils.

A typical measurement involves tuning through some parameter space, for example the externally applied magnetic field, and taking a position scan at each measurement point. The total voltage signal is collected and can then be fit to extract the magnetic moment of the sample. Providing the sample size, magnetisation and alignment requirements are met the total signal can be fit with the standard form for a magnetic dipole passing through a second order gradiometer coil [106, 107]. In the standard approach to data analysis this form is fitted, using simple linear regression, directly to the SQUID output signal using inbuilt software. This method requires an accurate knowledge of the centre of the sample which is easily determined during a carefully conducted set up phase for each sample measurement.

2.3.2 Sample mounting and measurement considerations

As described in section 2.3.1 it is important to take appropriate action to ensure the sample being measured can be treated successfully as a point magnetic dipole. Here a brief account of the typical sample preparation and mounting procedure is given along with some specific experimental considerations for superconducting-ferromagnetic thin film samples.

Before a sample is mounted it is first trimmed using a diamond cutter into a square $(3 \times 3)\ mm^2$ in size. This can then be fixed securely to the sample holder. Often a plastic straw is used but where alignment is crucial, as it has turned out to be for these SF thin films which can have a strongly angular dependent response and small signal amplitude, a rigid quartz rod is used instead. This results in a uniform background along the scan length and prevents any bending of the sample holder as the magnetic field is applied or the sample moved through the coils. The optimal alignment of the sample within the plane of the external field ensures the longitudinal component dominates and is not polluted with the transverse response. When interested purely in the magnetic character of the sample it is important to measure above the relevant superconducting transition to avoid any additional signatures of superconductivity being measured. Typically all the measurements presented here were carried out at a constant temperature of 10 K with the applied field varied and the resultant MH loop extracted from the SQUID responses as previously described.

3 | Anomalous Meissner Screening in SF systems

The work presented in this chapter is based on that published in [60] and follows directly on from the observations made in “Remotely induced magnetism in a normal metal” [39]. In this paper the authors reported an anomalous magnetic flux lowering within the N layer of an NSFnF spin valve structure measured using low energy muon spin rotation (LEμSR). The observed flux lowering showed a degree of dependence on the collinearity of the two ferromagnetic layers and could not be explained by an ordinary Meissner screening effect or by the quasiclassical theory framework for SF proximity systems. Since LEμSR does not directly distinguish between spin and orbital contributions to the magnetic flux profile and given the relatively complex sample structures; these initial measurements left open many possible origins for the observed effect. In a bid to uncover the source of the anomalous flux lowering we have therefore conducted a series of systematic experiments on simple S, NS and NSF thin film systems to disentangle the various contributions to the muon signal. We have observed the following:

i) The single layer S films expel the least flux, exhibiting a weak Meissner effect, the magnitude of which is set by λ_L.

ii) In the case of the NS bilayer, the N layer becomes fully proximitised such that the Meissner screening extends across the full sample in a near symmetric fashion. This can be successfully modelled using the quasiclassical theory and depends largely on the mean free path of N.

iii) In the case of the NSF trilayer samples the addition of a thin ferromagnetic layer surprisingly results in a further enhancement to the magnetic flux expulsion. This was unanticipated by theory and is contrary to the ideas of SF pair breaking.

When taken together these observations have allowed the origin of the anomalous effect to be pinpointed to the addition of the thin ferromagnetic layer though the underlying mechanism could not be identified at the time the analysis was carried out. The results of this study highlighted a gap within the existing theory of SF proximity systems and strongly suggest a degree of cooperation between the superconducting and ferromagnetic orders which is an essential ingredient for application to superconducting Spintronics. Following the publication of this work in [60] there was a flurry of activity within the the SF theory community which culminated in the development of a new theory of electromagnetic proximity [40–42] which will be discussed in detail in chapter 4 within the context of this work.

3.1 Introduction

As previously discussed within chapter 1, when a material becomes superconducting it loses all electrical resistance [5, 6, 108, 109] and develops the ability to expel magnetic fields through the Meissner effect [30]. Whilst detection of zero resistance is these days quite often a simple affair; the direct measurement of the flux profile across a superconductor is still a challenge. If one can measure the flux profile of a mesoscopic system, however, the reward is great. Even in the simple case of a thin film superconductor the response to an applied field can be very different to the bulk behaviour, depending on how the London penetration depth (λ_L) compares with the film thickness [47, 110], and in normal metal - superconductor bilayers the Meissner response can be highly non-trivial. In such a system, depending on the relative material parameters and interface resistances, it is possible for the normal metal to exhibit a Meissner screening response thanks to the propagation of superconducting correlations *via* the proximity effect [58, 59, 111–115]. This response can in some cases even be stronger than that of the thin film superconductor; an effect which largely depends on the mean free path of the normal metal [58, 60]. Things get even more interesting, however, when the normal metal is replaced with a thin ferromagnetic layer. This has the potential consequence of generating a net paramagnetic Meissner response [31], as opposed to the usual diamagnetic screening, thanks to the possibility of odd-frequency triplet correlations existing within the system. Additionally, it is possible to manipulate the superconductivity within these systems to tune between dominantly singlet or triplet behaviour. This has been demonstrated at spin active interfaces

[116–118] using, for example, non-collinear ferromagnets [24, 119–125] and within spin valve structures where the relative orientation of different ferromagnetic layers can be varied [75–81]. This tuning has a visible effect on the screening and so by probing the spatial flux profile one can therefore gain access to a wealth of information about the microscopic picture within these proximity systems. All this, however, requires a detailed knowledge of the underlying behaviour of each layer within the sample since it is imperative to be able to disentangle what contributions to the total signal come from which phenomena. The experiments must therefore be carried out in a careful and systematic way with a variety of corresponding control measurements on more simple systems.

As described in section 2.1 LEμSR offers a uniquely sensitive way to measure local flux within a sample. With this in mind and with the aim of understanding the anomalous behaviour reported by Flokstra *et.al.* in [39] the results of a systematic LEμSR study on simple thin films of copper (N), niobium (S) and cobalt (F) are presented within this chapter.

3.2 Samples

3.2.1 Sample design

In order to investigate the source of the anomalous behaviour observed in [39] a series of thin film structures of the form S, NS and NSF; where N = Cu(40), S = Nb(50) and F = Co(2.4) and the brackets indicate layer thickness in nanometers, were grown. Figure 3.1 shows a cross section of the sample layouts used for the study. The samples were grown atop conducting silicon substrates to prevent any charging and high voltage issues during the muon measurements. In the case of the NSF trilayer samples a thin, non-superconducting, buffer layer of niobium was deposited before any further growth occurred. This was necessary to ensure a smooth growth of the cobalt layer, and consequently a clean resultant magnetic state, since the niobium is well lattice matched contrary to the silicon substrate.

Two separate sample series were prepared. The first, Set I, was grown using a Nb target purity of 99.99 % compared with the 99.999 % purity used for sample Set II. The effect of the differing target purities we expect to be twofold. Firstly, the superconducting transition temperature (T_c) will be reduced where the Nb quality is lower and secondly, seeing as there will

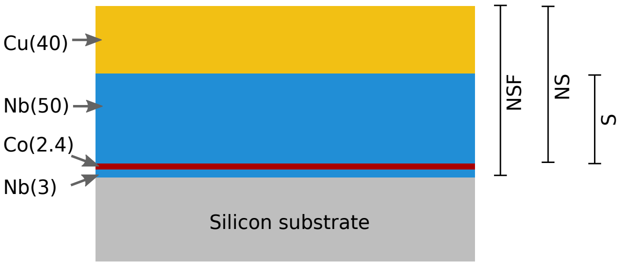

Figure 3.1: Schematic diagram of the S, NS and NSF sample structures. In the NSF case a thin niobium buffer layer is used to ensure smooth Co growth.

be more impurities present, the mean free path will be shorter resulting in a longer London penetration depth (λ_L). These differences ought to be reflected in both the transport measurements and in the LEμSR results, where we expect to see an increased Meissner screening response in Set II when compared with Set I. By growing these two variable Nb purity sets a more detailed understanding of the underlying thin film superconductivity and NS bilayer proximity effect can be developed. This is because there will be two data sets where the relative material parameters between the Nb and Cu are different and where consequently the systems may sit within a different regime of behaviour.

3.2.2 Sample growth

All samples were grown using DC magnetron sputtering [126, 127], with support from Dr Gavin Burnell and coworkers at the university of Leeds, at ambient temperature in a system with a base pressure of 10^{-8} $mbar$. The samples were grown atop Si(100) substrates which had been cleaned in a bath of alcohol before being loaded into the vacuum chamber. Each sample set was grown within a single vacuum cycle to ensure uniform sample quality and make for appropriate comparisons between the different sample structures. All growth was performed under an Ar flow of 24 $sccm$ at a rate dependent on the material being deposited. In order to determine the growth rate for each source single material layers were deposited, over a fixed period of time, and measured using low energy x-ray reflectivity (XRR) [128]. Some example data are shown in figure 3.2.[26] The thickness of each layer was extracted from fits to the Kiessig fringes and the growth rates subsequently determined and are displayed in table 3.1

---

[26] XRR data supplied by Dr Nathan Satchell, University of Leeds.

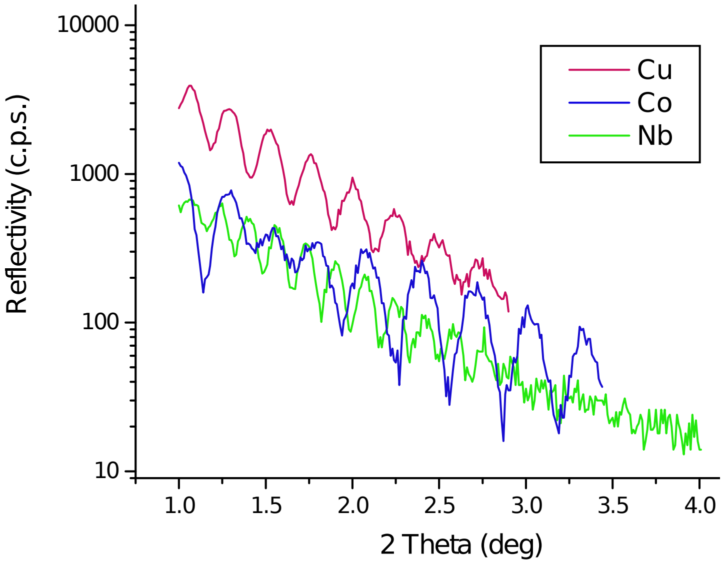

Figure 3.2: The XRR data from which the growth rates displayed in table 3.1 were extracted.

Table 3.1: Table of material growth rates

source	**growth current** mA	**growth time** s	**thickness** Å	**growth rate** Ås^{-1}
Co	50	300	260	0.9
Nb	100	200	520	2.6
Cu	50	100	350	3.5

3.3 Sample characterisation measurements

Once the samples had been grown, a number of characterisation measurements were performed ahead of the LEμSR beamtime experiments. These were carried out in St Andrews using both the MPMS SQUID magnetometer and the Cryogenic mini cryogen-free transport system. Please see sections 2.3 and 2.2 respectively for details of the experimental systems used.

3.3.1 Resistance and critical field measurements

Resistance and critical field measurements as a function of temperature are presented in figure 3.3 for sample Set II. These are representative of all measurements taken on both sets and further details regarding the measurements can be found in appendix B.

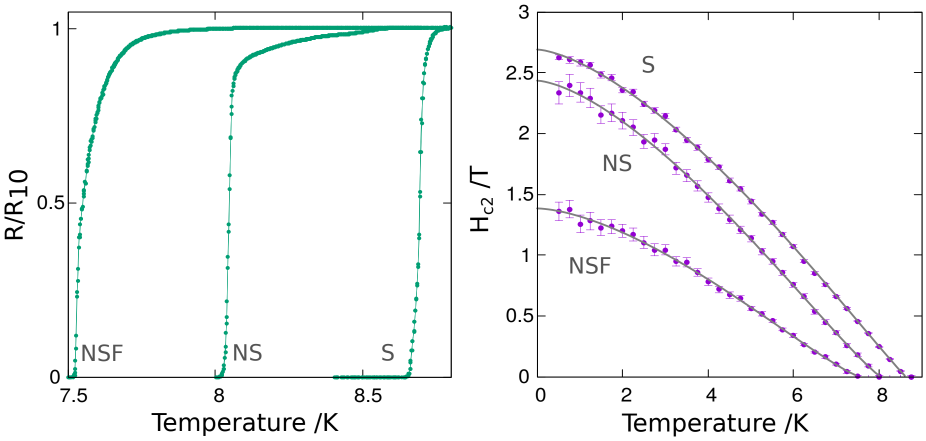

Figure 3.3: Transport data for the S, NS and NSF thin film samples from Set II. The left panel shows the resistance data, normalised to the normal state value measured at 10 K, and the right the upper critical field. The upper critical field measurements were carried out with the applied field direction perpendicular to the sample plane.

Table 3.2: Sample parameters extracted from transport measurements presented for sample sets I and II.

sample structure	T_c /K		**ΔT** /mK		H_0 /T		ξ_s /nm	
	I	*II*	*I*	*II*	*I*	*II*	*I*	*II*
S	8.35	8.69	42	72	2.58	2.69	11.3	11.1
NS	8.17	8.05	380	275	2.21	2.43	12.2	11.6
NSF	7.59	7.55	360	170	1.64	1.38	14.1	15.4

The left panel of figure 3.3 shows the resistance-temperature (RT) data, measured on an up and down temperature sweep at a current of 10 μA, for the N, NS and NSF samples. The resistance has been normalised to the normal state value measured at $T = 10\ K$ (R_{10}). As might be expected, the addition of both the N and F layers in direct contact with the superconductor results in a significant suppression of the superconducting transition temperature (T_c). This suggests that the interfaces between the different material layers are clean and allow for transport of superconducting correlations out of the Nb and into the neighbouring elements. From the RT plot the value of T_c and an associated transition width (ΔT) can be extracted. These values are shown in the first two columns of table 3.2 for both sample sets. More details about how these values were extracted from the data can be found in appendix B. For Set I, grown with the less pure niobium target, the T_c values are lower and the interface quality appears to be marginally worse. This is evident from the smaller shift in T_c and the larger broadening of the RT curves in those structures containing normal metal and ferromagnetic layers when compared with the bare superconductor. The behaviour of T_c and ΔT is qualitatively consistent between sets.

The right of figure 3.3 presents the upper critical field as a function of temperature for S(II), NS(II) and NSF(II). For all measurements the field was applied perpendicular to the sample plane. Each individual point was extracted from a resistance-applied field (RH) curve measured at constant temperature. The criterion used to define H_{c2} was that the resistance had dropped to 2% of R_{10}. The error bars were determined based on the field step size and the RH transition width which was typically broader for lower temperatures. Further details of the data analysis procedure used can be found in appendix B. The solid lines represent fits to the data using equation 3.1 where H_0 is the upper critical field at zero temperature and α and β are parameters associated with the dimensionality of the system [7, 47, 129]

$$H_{c2}(T) = H_0 \left(1 - \left(\frac{T}{T_c}\right)^{\alpha}\right)^{\beta} , \tag{3.1}$$

$$H_{c2}(T) = \frac{-\phi_0}{\mu_0 2\pi \xi_{GL}} \left(1 - \frac{T}{T_c}\right) , \tag{3.2}$$

$$\xi_S = \frac{2}{\pi} \xi_{GL} . \tag{3.3}$$

A standard Levenberg-Marquardt fit algorithm [95] was used to optimise the values of H_0, α and β with the value of T_c fixed to that extracted from the respective RT measurement. Equations 3.2 and 3.3 could then be used to determine the value of the superconducting coherence length ξ_S where ξ_{GL} is the Ginzburg-Landau coherence length and all other symbols have their standard meaning. The values of H_0 and ξ_s for each sample set are shown in columns 3 and 4 of table 3.2. All of the superconducting thin film samples result in ξ_s values of the order $10 - 15$ nm as opposed to values of up to 40 nm measured in high purity niobium [48].

3.3.2 SQUID measurements

The MPMS was used to characterise the magnetic behaviour of the Co within the NSF trilayer samples. The measurements presented here were taken at a temperature of 10 K such that the system was in the normal state.

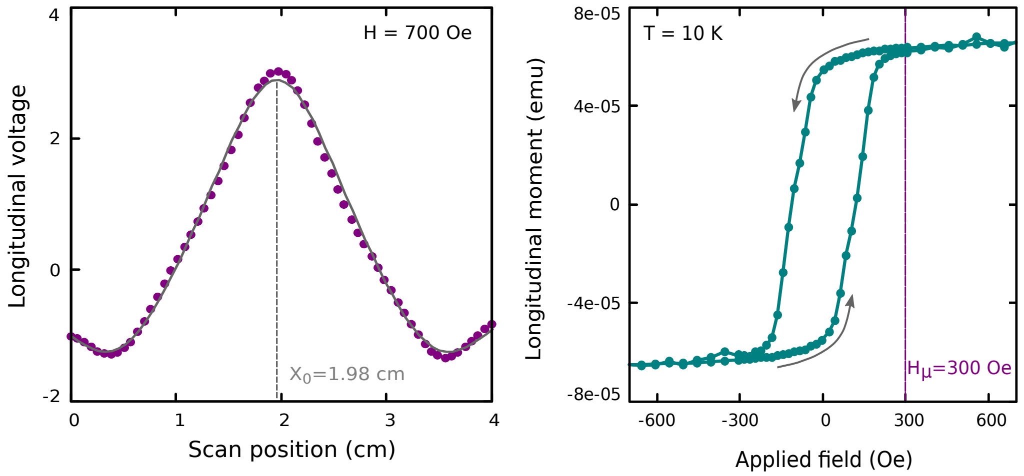

Figure 3.4: left panel: an example voltage - position curve for NSF(II). The data (points) are shown with the associated fit of the magnetic dipole model (line). The dashed line indicates the centre position. right panel: MH loop for NSF(II). The muon measurement field is marked with a vertical line.

The left panel of figure 3.4 presents a representative raw SQUID scan for the NSF(II) trilayer sample. The plotted points are the measurement data and the line shows a fit of the magnetic dipole model made to that data. From this fit to the raw scan the moment can be extracted and plotted as a function of the applied field which, for the example data set was set to 700 Oe. A series of such scans at different applied field were measured, fitted and used to plot the moment as a function of applied field curve shown in the right panel of figure 3.4. The arrows show the direction of the measured field sweep and the vertical line indicates the applied measurement field used for the LEμSR measurements which was typically set to 300 Oe.

The magnetic dipole model appears to be a good description of the scan data shown in the left panel of figure 3.4 with only small deviations from the expected behaviour evident round the peak. As expected, the extracted values of magnetic moment as a function of applied field presented within the right of figure 3.4 show the magnetic hysteresis typical for a ferromagnetic sample. Importantly, at an applied field of 300 Oe the ferromagnet has almost reached saturation and so the magnetic state should be saturated for LEμSR measurements conducted at applied fields of $\approx$ 300 Oe.

3.4 Low energy muon spin rotation measurements on S, NS and NSF thin film samples.

In this section the focus is on the experimental procedure and results specific to these S, NS and NSF thin film samples. As such only a skeleton of the technique and analysis is repeated for completion. For further information regarding muon spin rotation measurements and data analysis the reader is referred back to section 2.1 where these are discussed in detail.

All LE-μSR measurements were carried out on the μE4 beamline at the Paul Scherrer Institut [91]. As described in section 2.1.4 LEμSR allows the magnetic flux profile of a sample to be mapped out, to an energy dependent spatial resolution and field uncertainty of around 0.1 Gauss, over typical probing depths within the range $(10 \leq x \leq 100)\ nm$ [90]. The measurement involves a nearly 100% spin polarised beam of muons, of tunable energy, incident on the sample single muon at a time. Once implanted a muon will rapidly thermalise before Larmor precessing around the local magnetic field. At some later time the muon decays and emits a positron preferentially along its momentary spin direction which is collected at one of two positron counter detectors. By collecting the resultant positrons from a statistically significant number of events, in this case each spectrum comprises 2.5 million counts, the contained information about the local magnetic environment the muon ensemble experienced can be extracted [86].

In order to probe the screening behaviour of the sample an external magnetic field of 300 Oe is applied above T_c within the plane of the sample as sketched previously in figure 2.4. The incoming muon energy is varied, where for each energy a spectrum of 2.5 million events is collected both in the normal state ($T = 10\ K$) and the superconducting state ($T = 2.5\ K$), such that for each energy E at each temperature the average flux $\langle B(E) \rangle$ can be determined. A conversion from energy to spatial coordinates can then be carried out using the stopping profile of muons within that sample as calculated using a well-proven Monte Carlo algorithm [93, 94]. The result of this standard "averages" approach to the data analysis is an average spatial profile $\langle B(\langle x \rangle) \rangle$. Where the underlying flux profile is known, however, this can be imposed on the data and a full spatial dependence extracted from the weighted averages.

3.4.1 Single Nb layer: determining λ_L for each sample set

By first examining the data for the two simple thin film samples of niobium an indication of the "bare" superconducting response was determined. The corresponding penetration depths were extracted from the full spatial analysis of the average data within the London model. These results could then be used as a reference for the bilayer and trilayer sample analysis presented in sections 3.4.2 and 3.4.3 respectively. Figure 3.5 shows the results of the LEμSR measurements on the thin film niobium samples from Set I and II. Within this section each component of this plot shall be discussed in some detail.

A subset of the calculated stopping profiles for a 50 nm thick film of niobium are shown in the top panel of figure 3.5c).

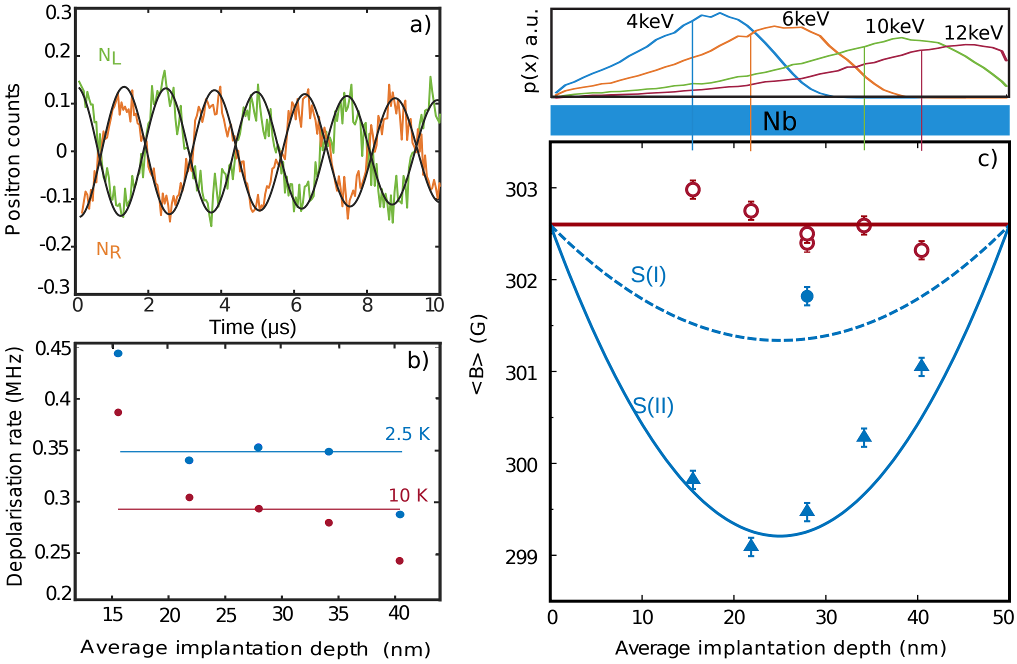

Figure 3.5: LEμSR results on thin film niobium. a) Example raw LE-μSR data. N_L and N_R are the left and right detector data respectively and the grey lines are fits to the data. The spectra shown are for S(II) measured at $E_\mu = 4\ keV$ and $T = 2.5\ K$. b) Depolarisation rate as a function of $\langle x \rangle$ above and below T_c for S(II). c) Top panel: muon stopping profiles for a range of energies. The vertical lines indicate the average probing depth in each case. Bottom panel: Average field as a function of average depth. The solid lines represent the best fit field profiles and the data points are the average values. Open (closed) data points correspond to normal (superconducting) state measurements taken at 10 K (2.5 K).

At the lowest easily accessible muon probing energy, $E_\mu = 4\ keV$, almost all of the muons stop in the top half of the niobium thin film. As the muon energy is increased the average stopping position shifts to higher depths and the profile becomes broadened such that a tail of the distribution always probes the top region of the sample. At $E_\mu \geq 12\ keV$ the muons begin to substantially sample the silicon substrate. This does not present a problem to our analysis, however, since silicon is known to trap muons within muonium states and so does not contribute to the total signal [130]. If one considers the stopping profiles, it is clear that by measuring a set of energies ($E_\mu = 4, 6, 8, 10, 12$) keV the full spatial extent of the niobium will be spanned in enough detail to map out a spatial profile. It is also important to note that where a single stopping profile spans the full extent of the sample, and the form of the underlying spatial profile is known, it is possible to reconstruct the spatial information from that single measurement alone (though with larger error).[27] With this in mind it is only necessary to measure the full set of probing energies for one of the thin film niobium samples since the average data immediately show the London profile is an appropriate description for these thin film systems. This is the strategy taken here where limited beamtime was available to complete the measurements.

The results of the conventional averages approach to the data analysis are shown as the plotted points in the bottom panel of figure 3.5c) where the corresponding error bars are taken directly from the results of the data fitting. As detailed in section 2.1.4 these average flux values are extracted from the measured raw detector spectra. A representative spectrum for S(II), measured at $E_\mu = 4\ keV$ and $T = 2.5\ K$, is presented in figure 3.5a). The left (N_L) and right (N_R) detector data are plotted separately with their associated fits shown as solid grey lines. There is a good correspondence between the data and the fit which has a resultant goodness of fit parameter $\chi^2 = 1.04$. All open symbols correspond to the normal state measurements where the applied measurement field of 302.6 Oe[28] was simply recovered. The superconducting state data are plotted separately in closed circles and

---

[27] This is possible because the stopping profile tells us how the sampling of the underlying flux profile across the full layer is weighted. Given the flux average across the layer, therefore, one need only tune the fit parameters of the known profile until its average best matches the measured flux average when sampled as dictated by the stopping profile.

[28] Although the measurement field was set to 300 Oe there is some room for error in the supply current. Once set this remains constant providing there are no changes made to the system. This discrepancy, and to attribute any measured changes to superconductivity, is why the normal state is measured for all samples as a reference.

triangles for S(I) and S(II) respectively. For both measured samples a small flux lowering is observed across all measured energies. This is due to the expected Meissner screening response which in the case of S(I) and S(II) is of the order of 0.1% and 1% respectively reflecting the difference in niobium quality and the consequent difference in the London penetration depth λ_L.

As discussed in section 2.1.6 it is often possible to spatially model the muon depolarisation rate (λ) such that it can be constrained or even treated as a fixed parameter. For a single layer sample, such as was measured here, this is very simple. Figure 3.5b) shows a plot of the λ values as a function of the probing depth. The plotted points are the unconstrained values obtained from the averages analysis where open circles are measured in the normal and closed circles the superconducting states respectively. In the normal state the average fit value for λ was around 0.3 MHz, which represents the nuclear depolarisation rate of the niobium, and in the superconducting state this increases slightly to 0.35 MHz due to the flux gradients now present within the system. Once determined it is then possible to fix the value of λ to its average value, in the case where it should remain constant across the sample, in an effort to constrain the fit. For these simple samples there is little point in carrying out this profile analysis but modelling λ will become very important in the following two subsections where there are multiple material layers and significant stray fields present across the sample.[29]

In the case of S(II) the full set of energies maps out the expected cosh-like shape of the Meissner profile for a thin film superconductor. This form is given by equation 3.4 where d_S is the thickness of the thin film [47].

$$B_S(x) = B_0 \cosh\left(\frac{x}{\lambda} - \frac{d_S}{2\lambda}\right) \cosh\left(\frac{d_S}{2\lambda}\right)^{-1} \tag{3.4}$$

As such it seems an appropriate choice to take this analytical form of $B_S(x)$ and impose it on the superconducting state data for both S(I) and S(II) such that in each case the full spatial profile can be extracted from the average data as described in section 2.1.7. The results of this analysis are shown in the bottom panel of figure 3.5c). In the normal state the field profile, represented by the solid red line, is constant across the sample at the average measured value of the applied field. In the superconducting

---

[29] The precise origins of the scatter in the average lambda values from the unconstrained fit is not clear. For higher energies the muons start to sample the substrate and for lower energies perhaps the vacuum interface plays a role in generating additional sources of depolarisation.

state the resultant best-fit profiles for S(I) and S(II) are represented by the dashed and solid blue lines respectively. The corresponding best-fit values of λ_L are shown in table 3.3.

Table 3.3: Table of best-fit λ_L values for S(I) and S(II).

sample	λ_L *nm*	$\pm\Delta(\lambda_L)$ *nm*	χ^2
S(I)	270	5	1.060
S(II)	160	2	1.045

It is clear from the successful data modelling that the choice of profile given by equation 3.4 is appropriate for these thin film systems.[30] As can be seen in table 3.3 the expected result, that λ_L(I) should be significantly longer than λ_L(II), was recovered from the analysis. When compared with the behaviour of clean niobium, where $\lambda_L \approx 30$ *nm*, [48–51] these dirty thin film systems produce a limited screening response due to their relatively short mean free paths which were measured, using a standard Van der Pauw method, at room temperature to be of the order of 1 *nm*. This in turn effects the London penetration depth, where values of up to 230 *nm* have been previously observed [52, 53], such that ultimately the applied field is only partially screened at an amplitude dependent on λ_L/d_S.

By successfully modelling the data in this way a benchmark value of λ_L, and consequently the Meissner screening amplitude, has been determined for each of the different niobium growth qualities. Given the same sample growth conditions the results on more complex structures can be compared against these values and the origins of any anomalous behaviour investigated in a more systematic way than was previously possible.

3.4.2 NS bilayer results and quasiclassical modelling

The natural extension to the thin film superconductor is the NS bilayer system to which we now turn our attention. Within this section are presented the results of the LEμSR measurements and analysis on NS(I) and NS(II). In the latter half of the section the focus is on using the quasiclassical formalism to model the behaviour of the bilayer systems. These calculations were carried out by Dr Machiel Flokstra using a self-built software suite

---

[30] Importantly, the average and full spatial approaches to modelling the data are distinct and the resultant values should not directly correspond to one another.

[131]. As shall be seen in what follows, this formalism can provide the opportunity to model the LEμSR data with great success but does require knowledge of many experimentally determined material parameters as input to the model. Some of these were extracted from transport measurements and some from the muon measurements on the bare niobium samples presented in the previous section.

Part I: LEμSR results

The results of the LEμSR measurements on NS(I) and NS(II) are presented in figure 3.6 where the best-fit London profiles for S(I) and S(II) are also shown, as dashed and solid grey lines respectively, for comparison.

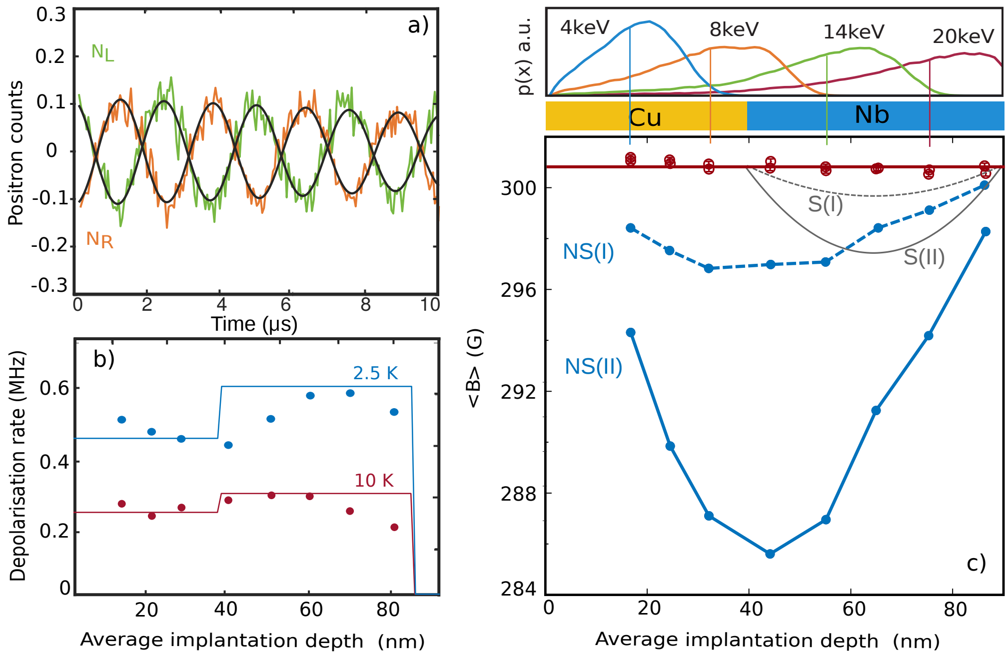

Figure 3.6: LEμSR results on the CuNb bilayer samples. a) Example raw LE-μSR data. N_L and N_R are the left and right detector data respectively and the grey lines are fits to the data. The spectra shown are for NS(II) measured at $E_\mu = 4\ keV$ and $T = 2.5\ K$. b) Depolarisation rate as a function of $\langle x \rangle$ above and below T_c for NS(II). c) Top panel: muon stopping profiles for several selected implantation energies with the lines indicating the corresponding average sampling depth. Bottom panel: Average field as a function of average depth. Open (closed) data points correspond to normal (superconducting) state measurements taken at 10 K (2.5 K). The lines are a guide to the eye. The best fit field profiles for S(I) and S(II) are shown in grey for reference.

As can be seen with reference to the top panel of figure 3.6c) the stopping profiles behave similarly to those described in section 3.4.1 for S(I) and S(II) but where now, due to the additional copper layer, the probing energy range required to sample the full bilayer has increased. A set of energies spanning the range $(4 \leq E_{\mu} \leq 23)$ keV is now required to sample the full extent of the bilayer where for $E_{\mu} \geq 20$ keV some of the muons are once again lost to the sample substrate. Importantly, at an energy of 4 keV all of the muons stop within the Cu(40) layer. This is important since any measured average signal will be associated only with that material layer allowing an immediate conclusion to be drawn as to whether or not the screening extends beyond the niobium layer.

The results of the conventional muon data analysis are presented in the bottom panel of figure 3.6c). Error bars, typically $(0.1-0.3)$ G, are plotted but in most cases are too small to be visible on the y-axis scale. The open data points plotted in red correspond to the normal state data which were measured at a fixed temperature of $T = 10$ K. The filled points plotted in light blue show the superconducting state data measured at $T = 2.5$ K. As previously discussed each data point represents an average field value at some corresponding average probing depth extracted from a fit to the raw detector data and the lines are just a guide to the eye. An example spectrum, measured using an energy $E_{\mu} = 4$ keV and at a temperature $T = 2.5$ K for NS(II), is shown for the left (N_L) and right (N_R) detectors separately in figure 3.6a) along with the associated fits to the raw data (grey lines). Seeing as the sample is now composed of two different material layers with different material properties one can consider modelling the data to allow for a different fixed depolarisation rate in each layer. In this case a simple step function approach was taken as shown in figure 3.6b) where the depolarisation rate (λ)[31] is plotted as a function of the average probing depth. The data points represent the average values extracted from the conventional approach to the data analysis and the solid lines are the optimised step function profiles. The step was fixed to be at the known interface position and the amplitudes either side treated as free fit parameters. As described in sections 2.1.6 and 2.1.7, the resultant best-fit profile then constrains the value of λ within the different regions which are sampled by the incoming muons in a manner weighted by the relevant

---

[31] Not to be confused with λ_L which is the London penetration depth.

stopping profiles. This allows a more accurate fit to the data to be achieved since the modelling now accounts for the material differences in a controlled way resulting in improved χ^2 values and consequently smaller error bars in the extracted average fields.

Considering again the results presented in the bottom panel of figure 3.6c) it can be seen that as expected the normal state measurements simply recover the applied field. In the superconducting state a flux lowering is observed for all measured energies for both NS(I) (points with a dashed blue line) and NS(II) (points with a solid blue line) which clearly shows the Meissner screening response extends well into the copper layer. Indeed if one considers the $E_\mu = 4\ keV$ data, which samples only the Cu(40) layer, the screening response built up over the stopping profile is roughly $3\ G$ and $7\ G$ for NS(I) and NS(II) respectively which strongly suggests the copper layer has been fully proximitised. This is echoed by the substantial increase, in both cases, of the overall screening amplitude that has built up across the full spatial extent of the bilayer. A quick comparison to the S(I) and S(II) data shows the amplitude is now approximately three times larger in both sets when compared to the bare response. Such an increase must be associated with a corresponding increase in the available screening volume. Within the bilayer system, therefore, the pairs are able to utilise the copper layer in an effort to screen the applied field more effectively such that λ_L/d_{NS} is now the relevant quantity in deciding what fraction gets screened away. How effective the copper layer is in boosting the screening is related to its mean free path since this will determine, for a given interface resistance, how well the screening pairs can propagate through the system. This shall be explored in more detail in part II, within the context of the quasiclassical formalism, and although the result seems counter-intuitive in fact it drops directly out of the theory and is in agreement with earlier work by Belzig et al. [58].

Part II: quasiclassical modelling of the flux profile

Whilst the results of the conventional approach to the LEμSR data analysis immediately provide evidence for a large increase in screening amplitude they do not give a detailed picture of how or why this is happening. Neither do they provide a full form for the spatial flux profile, $B_{NS}(x)$, which may be very different to that for the thin film superconductor given by equation

3.4. In both cases it is useful to turn to the quasiclassical theory for dirty thin film superconductors. In doing so, the theoretical response of the total system to an applied field can be calculated and compared with the experimental results. In this way the relevant tuning parameters can be identified and a clear picture of the numerical form of $B_{NS}(x)$ obtained. Within this subsection a brief description of the method and results of the modelling procedure will be presented along with some discussion of their implication to the LEμSR data analysis in later chapters.

The calculations involve using the quasiclassical theory in the dirty limit to determine the system Green's functions. Once these are known the response to a small externally applied field can be determined *via* the linear response theory. The result is a numerical spatial profile for the flux across the sample which can then be directly compared to the experimental data. As stated previously the calculations presented here are the work of Dr Machiel Flokstra and in what follows a sketched outline of the method he used will be given.[32]

A system's Green's functions describe how, under the influence of interactions, particles propagate through that system. Since the samples of interest here are superconducting, the single particle, $G_{\alpha,\beta}(x,x^{'})$ and $\bar{G}_{\alpha,\beta}(x,x^{'})$, and the anomalous Green's functions, $F_{\alpha,\beta}(x,x^{'})$ and $\bar{F}_{\alpha,\beta}(x,x^{'})$, are required to describe their behaviour. These are defined as

$$\begin{aligned}
G_{\alpha,\beta}(x,x^{'}) &= -i\left\langle T_t\left(\psi_\alpha(x)\psi^\dagger_\beta(x^{'})\right)\right\rangle \ , \\
\bar{G}_{\alpha,\beta}(x,x^{'}) &= -i\left\langle T_t\left(\psi^\dagger_\alpha(x)\psi_\beta(x^{'})\right)\right\rangle \ , \\
F_{\alpha,\beta}(x,x^{'}) &= -i\left\langle T_t\left(\psi_\alpha(x)\psi_\beta(x^{'})\right)\right\rangle \ , \\
\bar{F}_{\alpha,\beta}(x,x^{'}) &= -i\left\langle T_t\left(\psi^\dagger_\alpha(x)\psi^\dagger_\beta(x^{'})\right)\right\rangle \ .
\end{aligned} \tag{3.5}$$

The $\psi_{\alpha/\beta}$(x) and the $\psi^\dagger_{\alpha/\beta}$(x) are the electron creation and annihilation operators respectively for a state of spin axis α or β at coordinate $x = (\mathbf{r}, t)$ and T_t is the time ordering operator. The single particle Green's functions represent the motion of a particle from $x \rightarrow x^{'}$ whilst the anomalous Green's functions describe the coherent transport of correlated particle pairs which is

---

[32] With reference made to the following sources: [60, 131–135].

required for Cooper pair transport. Since the anomalous Green's functions describe the behaviour of the Cooper pairs they also give access to the order parameter of the system, Δ, which in the case of a conventional s-wave superconductor will only have elements involving electrons of opposite spin.

Equation 3.5 shows the real-time Green's functions though it is often convenient to work in terms of imaginary time in the Matsubara formalism. This involves a change of time coordinate $t \rightarrow \tau = it$ which transforms the time ordering operator $T_t \rightarrow T_\tau$ and results in the Green's functions only be defined over some finite time window $\frac{-\hbar}{k_B T} < (\tau - \tau^{'}) < \frac{\hbar}{k_B T}$. Within this formalism for a steady state problem it then becomes convenient to Fourier transform the Green's functions such that they are non-zero only for a discrete set of frequencies up to some cut-off defined by ω_{Debye}. These are the so-called Matsubara frequencies, ω_n, shown in equation 3.6 where n is some integer.

$$\hbar\omega_n = (2n+1)\pi k_B T \tag{3.6}$$

Note that as $T \rightarrow 0$ then $(\tau - \tau^{'}) \rightarrow \infty$ and the discrete set of Matsubara frequencies becomes a continuum. The Matsubara formalism is computationally advantageous at finite temperatures where less frequencies are required to describe the system than in the real-time case. It can, however, only be applied to equilibrium systems such as that considered here where the goal is to calculate the screening response of a supercurrent.

It is often useful to write the Green's functions in spin space as 2 × 2 matrices whose elements represent all possible spin combinations as shown in equation 3.7

$$\begin{aligned}
\hat{G}(x,x^{'}) &= \begin{pmatrix} G_{\uparrow\uparrow}(x,x^{'}) & G_{\uparrow\downarrow}(x,x^{'}) \\ G_{\downarrow\uparrow}(x,x^{'}) & G_{\downarrow\downarrow}(x,x^{'}) \end{pmatrix} , \\
\hat{\bar{G}}(x,x^{'}) &= \begin{pmatrix} \bar{G}_{\uparrow\uparrow}(x,x^{'}) & \bar{G}_{\uparrow\downarrow}(x,x^{'}) \\ \bar{G}_{\downarrow\uparrow}(x,x^{'}) & \bar{G}_{\downarrow\downarrow}(x,x^{'}) \end{pmatrix} , \\
\hat{F}(x,x^{'}) &= \begin{pmatrix} F_{\uparrow\uparrow}(x,x^{'}) & F_{\uparrow\downarrow}(x,x^{'}) \\ F_{\downarrow\uparrow}(x,x^{'}) & F_{\downarrow\downarrow}(x,x^{'}) \end{pmatrix} , \\
\hat{\bar{F}}(x,x^{'}) &= \begin{pmatrix} \bar{F}_{\uparrow\uparrow}(x,x^{'}) & \bar{F}_{\uparrow\downarrow}(x,x^{'}) \\ \bar{F}_{\downarrow\uparrow}(x,x^{'}) & \bar{F}_{\downarrow\downarrow}(x,x^{'}) \end{pmatrix} ,
\end{aligned} \tag{3.7}$$

where the ↑ and ↓ subscripts indicate the spin direction. In the case of a superconducting system it is then convenient to go one step further and transform to the Nambu $\otimes$ spin space. This allows the Green's functions to be written as the single 4×4 matrix shown in equation 3.8

$$\check{G}(x,x^{'}) = \begin{pmatrix} \hat{G}(x,x^{'}) & \hat{F}(x,x^{'}) \\ \hat{\bar{F}}(x,x^{'}) & \hat{\bar{G}}(x,x^{'}) \end{pmatrix} \tag{3.8}$$

$$\text{with particle-hole convention: } \begin{pmatrix} \psi\psi^{\dagger} & \psi\psi \\ \psi^{\dagger}\psi^{\dagger} & \psi^{\dagger}\psi \end{pmatrix} .$$

It is this final representation shown in equation 3.8 that is used when solving the Usadel equation [136].

Seeing as these thin film systems are in the dirty limit, that is to say the coherence length is much longer than the mean free path, the system Green's functions will obey the Usadel equation which can be written as shown in equation 3.9 (see for example [137]).

$$i\hbar D\partial_x\left(\check{G}\partial_x\check{G}\right) = \left[\check{H}, \check{G}\right] \tag{3.9}$$

The coordinate system has been defined such that the x-axis is normal to the surface of the sample and all interfaces lie within the y-z plane in which translational invariance is assumed. A schematic diagram of this coordinate system is shown in figure 3.7.

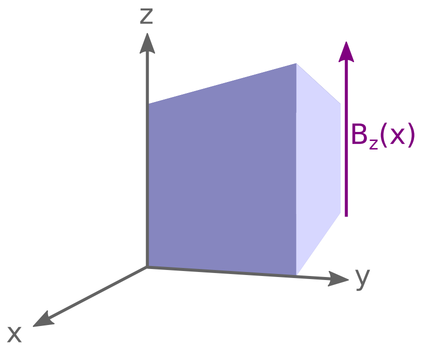

Figure 3.7: A sketch of the coordinate system used in the calculations. The x-axis is normal to the surface of the sample and all interfaces lie within the y-z plane in which translational invariance is assumed. The applied field is directed along z and screened along the x direction.

Equation 3.9 is defined within the Nambu $\otimes$ spin space as discussed above and D is the diffusion constant describing transport within the dirty system. The form of the Hamiltonian, $\check{H}$, depends on the system under consideration. In this case, to include the effects of a thin ferromagnetic layer with a homogeneous exchange field along z, J_z, $\check{H}$ can be written as shown in equation 3.10.

$$\check{H} = i\hbar\omega_n\left(\tau_3 \otimes \sigma_0\right) + \check{\Delta} - J_z\tau_0 \otimes \sigma_3 \tag{3.10}$$

The σ_i and τ_j are the usual Pauli matrices for the spin and Nambu space respectively and $\check{\Delta}$ is the superconducting gap function, or order parameter, expressed within the Nambu space. This system of equations must then be solved[33] such that the order parameter obeys the self-consistent gap equation given in equation 3.11.

$$i\Delta(x) = \frac{\pi k_B T}{\ln\left(\frac{T}{T_{c0}}\right) + \sum_n\left(\frac{1}{|2n+1|}\right)}\sum_{\omega_n} F_{\uparrow\downarrow}(x,\omega_n) \tag{3.11}$$

$\Delta(x)$ is the spatial profile of the gap across the sample and T_{c0} is the superconducting transition temperature of the bulk. Once this has been solved one has knowledge of the system Green's functions and can therefore calculate the response of the system to a small externally applied magnetic field.

As shown in figure 3.7, the applied field is directed along the z-axis and the screening response occurs along the x-direction. This coordinate system is chosen to be consistent with the results of the LEμSR measurements and allows for direct comparison to experiment. In order to determine the spatial flux profile one has to find the vector potential. According to linear response theory the screening current density, j_y, that develops in response to the presence of a vector potential, A_y is given by equation 3.12 [139].

$$j_y = -\frac{N_0 e^2 D}{\hbar} A_y \pi k_B T \sum_{\omega_n} \Re\left(F_{\uparrow\downarrow}\bar{F}_{\downarrow\uparrow} + F_{\downarrow\uparrow}\bar{F}_{\uparrow\downarrow}\right) \tag{3.12}$$

N_0 is the density of states near the Fermi level and $\sum_{\omega_n}\Re\left(F_{\uparrow\downarrow}\bar{F}_{\downarrow\uparrow} + F_{\downarrow\uparrow}\bar{F}_{\uparrow\downarrow}\right)$ is the sum of the real parts of the opposite spin terms of the anoma-

---

[33] This is solved using the interface boundary conditions as formulated by Nazarov in reference [138],

lous Green's functions. In addition, from Maxwell's equations $\mu_0\mathbf{J} = \nabla \times (\nabla \times \mathbf{A})$ and so by combining these two expressions is it possible to solve for the vector potential and thus, since $\mathbf{B} = \nabla \times \mathbf{A}$, the magnetic flux profile can be determined.

In order to make a direct comparison between the calculated and experimentally derived flux profiles the model system's material parameters need to be tuned to match the measured sample. A useful strategy is to first calculate the flux expulsion for a single niobium layer. Since the values of T_{c0} and ξ_{GL} are known only the niobium density of states is left as a free parameter. This can be used to tune the calculated profile such that it matches the corresponding $B_S(x)$ extracted from LEμSR measurements. For sample S(I) the known values are $T_{c0} = 8.5\ K$ and $\xi_{GL} = \frac{\pi}{2}\sqrt{\frac{\hbar D}{2\pi k_B T_{co}}} \approx 10\ nm$ which gives a resulting Nb density of states $N_0 = 4.0 \times 10^{28}\ \mathrm{m}^{-3}$. This value of N_0 can then be used as input for the corresponding bilayer NS(I) modelling. In order to determine the interface resistances the boundary conditions are tuned to predict the measured value of the bilayer T_c. This results in interface resistances of the order of $\mu\Omega cm$, where the transparency is set to unity, and a copper density of states $1.2 \times 10^{28}\ m^{-3}$. Since the diffusion constant in the copper can be written $D = \frac{v_F l_{Cu}}{3}$, where $v_F = 1.57 \times 10^6\ ms^{-1}$ is the Fermi velocity of copper [140], a value for the copper mean free path can be extracted and for NS(I) was found to be $l_{Cu} = 22\ nm$ which is very close to the experimentally determined value of 20 nm measured *via* the Van der Pauw method for sample Set II. Whilst this set of parameters best describes our experimental system it is also possible to use the copper mean free path as a means to tune through different transport regimes and to see what effect this will have on the screening response.

The results of these calculations are shown, alongside the experimental data, in figure 3.8. The set of curves labelled $1-5$ show the calculated flux profiles for corresponding copper mean free path values of $l_{Cu} = (5, 11, 16, 22, 34)\ nm$. The results show that the amplitude of the screening response across the full bilayer depends very strongly on the material parameters of the copper. For the shortest mean free path tested, curve 1, the resultant flux profile is almost identical to the London profile found experimentally for S(I) but with a small additional tail extending into the normal metal. The diffusion of the Cooper pairs into the copper is strongly suppressed where the mean free path is short but as the value of l_{Cu} is increased pairs are allowed to better diffuse into the normal metal.

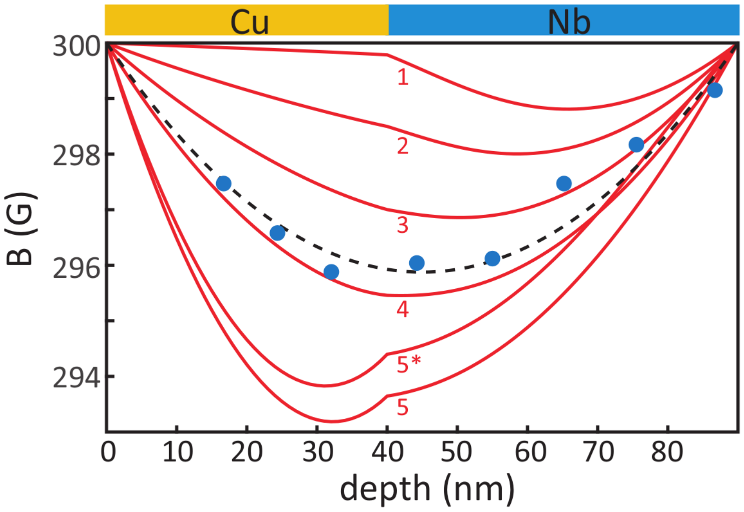

Figure 3.8: Calculated flux profiles for a Cu(40)Nb(50) bilayer sample with material parameters fixed to those of NS(I). Curves 1-5 correspond to different values of the Cu mean free path $l_{Cu} = (5, 11, 16, 22, 34)$ nm. The grey dashed line represents the profile calculated for a 90 nm film of Set I quality Nb for comparison with the NS(I) data plotted as the blue points. Curve 5^* shows the result of adding a thin cobalt layer to form a Cu(40)/Nb(50)/Co(2.4) trilayer sample where $l_{Cu} = 34$ nm.

and their ability to screen consequently increases. This continues until eventually the pairs within the copper layer expel flux more efficiently than an equivalent thickness of bare Nb. This is represented by the dashed line which shows the calculated flux profile for a 90 nm thick film of Nb(I). Interestingly, the average flux values derived from LEμSR measurements, represented by the blue data points, appear to sit at the crossover point between niobium and copper dominated screening.

The results presented in figure 3.8 have interesting consequences for how best to approach modelling the LEμSR data. Whilst a numerical form for the flux profile has been successfully determined, and could in principle be imposed upon the measured flux averages, for the combination of sample material parameters found within these sputtered thin films it turns out the resultant profile is highly symmetric. In this case, where the bilayer is as effective at screening as an equivalent thickness of niobium, a simple extension of the London model can be implemented whereby rather than being confined to the superconductor the profile extends over the full bilayer thickness, d_{NS}. This is clearly an approximation but has the benefit of providing a simple description with fewer fit parameters.

3.4.3 NSF trilayer results and modelling discrepancy

The final objective of this chapter is to address what happens to the Meissner screening profile after the addition of a thin ferromagnetic layer is made to the underside of the bilayer section. It would be expected that, due to the presence of the ferromagnetic exchange field, the superconducting gap would be reduced within the region close to the SF interface, weakening the superconductivity and reducing the total number of screening pairs present within the system. Additionally, the exchange field opens up the possibility of generating odd-frequency pairs which are known to produce a paramagnetic screening response. The net result would be a reduction in the overall flux expulsion with a bias to a loss in amplitude towards the ferromagnetic layer. These expectations are recovered by calculations, the results of which are shown alongside the NS(I) profiles in figure 3.8. Curve 5^* represents the effect of adding the thin Co(2.4) layer to the underside of the bilayer sample corresponding to curve 5. Additional parameters are required to describe the cobalt layer. The exchange field, J_z, was taken to be 321 meV (see for example [141]) and the coherence length within the ferromagnet $\xi_F = \sqrt{\frac{\hbar D_F}{J_Z}} = 1\ nm$ (see for example [8]). A clear reduction in the overall flux expulsion is visible and most pronounced within the niobium layer as reasoned above. As will become immediately obvious, however, the LEμSR measurements on NSF(I) and NSF(II) highlight a surprising discrepancy between the quasiclassical theory calculations and the extracted flux averages. Whereas the theory predicts a decisive reduction flux expulsion the measurements show a substantial increase approximately corresponding to a further 50% increase when compared with the corresponding bilayer sample.

The results of the LEμSR measurements on NSF(I) and NSF(II) are shown, with S(II) and NS(II) as grey lines for reference, in figure 3.9. The stopping profiles in the top panel of figure 3.9c) are largely consistent with those of the bilayer but where before sampling the substrate a fraction of muons for $E_\mu \geq 20\ keV$ will stop within the Co layer. These muons will be immediately depolarised but represent a relatively small fraction of the those stopping within the sample. More importantly, the stray fields generated by the ferromagnetic layer will cause an increase in the depolarisation rate which will extend across most of the bilayer section. The result being a more strongly damped total signal and larger error bars in the extracted field values especially for average depths close to the cobalt.

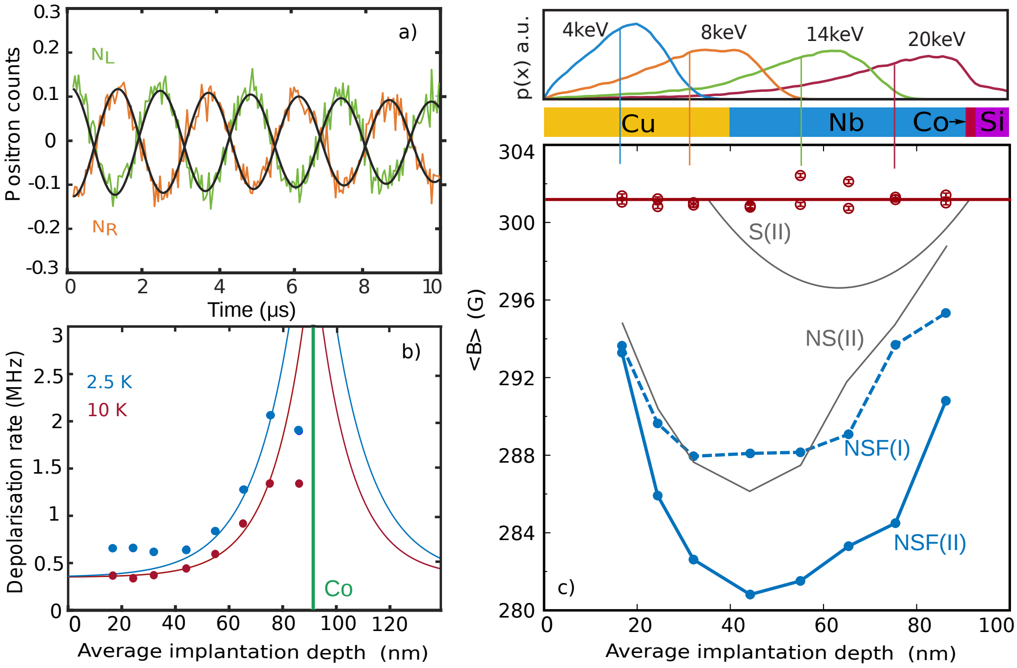

Figure 3.9: LEμSR results on the CuNbCo trilayer samples. a) Example raw LE-μSR data. N_L and N_R are the left and right detector data respectively and the grey lines are fits to the data. The spectra shown are for NSF(II) measured at $E_\mu = 4\ keV$ and $T = 2.5\ K$. b) Depolarisation rate as a function of $\langle x \rangle$ above and below T_c for NSF(II). The position of the Co layer is marked in green. c) Top panel: muon stopping profiles for several selected implantation energies with the lines indicating the corresponding average sampling depth. Bottom panel: Average field as a function of average depth. Open (closed) data points correspond to normal (superconducting) state measurements taken at 10 K (2.5 K). The lines are a guide to the eye. The best fit field profiles for S(II) and NS(II) are shown in grey for reference.

Figure 3.9a) shows an example raw spectrum measured for NSF(II) at a muon energy of $E_\mu = 4\ keV$ and a temperature of $T = 2.5\ K$. As before, the two detector signals are plotted separately with their associated fits shown as solid grey lines. Whilst there is no clear difference in the damping rate visible in the raw data at this energy when compared with the bilayer data in figure 3.6a) this data corresponds to a probing energy that focuses far from the Co layer. The reader is referred to appendix C for a comparison of the raw signal for different probing energies. The effect of the stray field from the cobalt layer is clearly visible, however, in figure 3.9b) which presents how λ changes as a function of the average probing depth for NSF(II). In the average values found both in the normal (red points) and superconducting (blue points) states the value of λ rises as the probing depth approaches the

Co layer (marked in green). This can be modelled, using an exponential profile as discussed in section 2.1.6, the result of which is plotted in each case as the solid line of corresponding colour. A good correspondence can be seen, particularly for the normal state data, between the model profile and the results of the average fitting. The extracted fit parameters of the model profile, an amplitude (λ_0) and decay length (ξ_λ), are shown in table 3.4 for both NSF(I) and NSF(II). The values of both λ_0 and ξ_λ are consistent across the two sample sets which would be expected since the procedure of cobalt growth was the same for each sample series. The decay length of around 15 *nm* suggests that the effects of the stray field are largely confined to a region of the niobium within 20 *nm* of the cobalt layer.

Table 3.4: Table of extracted depolarisation amplitudes and decay lengths for NSF(I) and NSF(II)

sample	λ_0 MHz	$\pm\Delta\lambda_0$ MHz	ξ_λ nm	$\pm\Delta\xi_\lambda$ nm
NSF(I)	3.2	0.1	13	1.5
NSF(II)	3.4	0.1	14	2.0

The flux averages extracted using the conventional approach to the muon data analysis are presented in the bottom panel of figure 3.9c). As always the normal state measurements have simply recovered the applied field. Upon cooling to below the superconducting transition a flux lowering is once again observed across all measured energies. Surprisingly this is in fact enhanced when compared with the screening amplitude of the respective bilayer. This rather interestingly is in direct opposition to the theoretical calculations presented in figure 3.8.

A crude comparison of the data for NS(II) and NSF(II) is presented in figure 3.10. This plot simply shows the point-by-point difference in the Meissner screening amplitudes as a function of the average probing depth. These amplitudes are calculated for each sample by taking the difference between the corresponding normal and superconducting state measurements presented in figure 3.9. The results presented in figure 3.10 clearly show the difference is largest within the region close to the SF interface and tapers off with distance towards the surface.

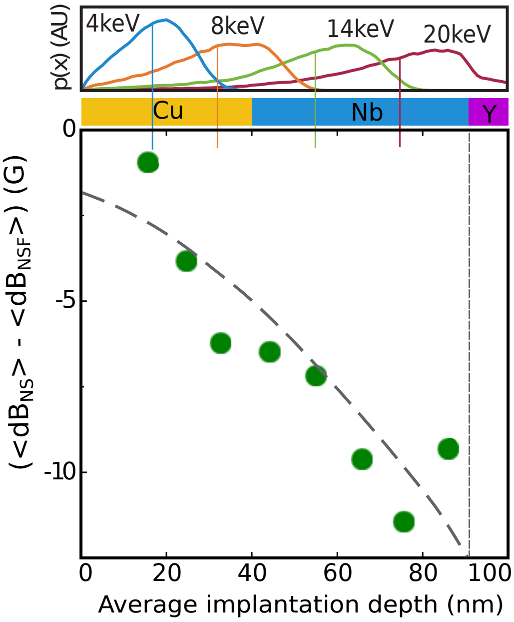

Figure 3.10: The data points represent the point-by-point difference in the average flux lowering between NS(II) and NSF(II) plotted as a function of the average probing depth. Here Y represents either Si or Co(2.4)/Nb(3)/Si depending on the sample. The vertical dashed line represents the interface and the dashed profile is a guide to the eye indicating how the additional amplitude might role off spatially.

At the very highest probing energy, $E_\mu = 23\ keV$, care needs to be taken not to over-interpret the slight uptick in the data. This is because the stopping profile for the NSF structure begins to appreciably probe the cobalt layer which will effect the validity of taking a direct difference in amplitude to the NS sample. The top panel of figure 3.10 presents the stopping profiles for reference. At an energy of $E_\mu = 20\ keV$ there is only a small tail extending beyond the bilayer section but for higher energies this fraction will increase and may begin to substantially effect the simple comparison being made since the spatial information is no longer the same.

Whilst highly simplified this method of comparison is nevertheless useful in providing some information as to the origin of the observed discrepancy between theory and experiment. Whatever the underlying effect, it appears to have its origins at the SF interface and extends across the sample decaying in amplitude as it goes. The lengthscale over which the additional component decays is much greater than the superconducting coherence length which suggests that the measured response cannot be associated with the inverse proximity effect due to spin polarised pairs existing close to the S/F interface. In addition, whilst the stray fields originating from the cobalt layer extend across the full NS section there is no evidence for any associated influence on the behaviour of the sample in the normal state. This strongly suggests that stray field does not play a role in generating the additional component to the screening.[34]

3.4.4 Temperature and field dependence

As discussed in section 2.1 instead of varying the muon energy one can sit at a fixed position within the sample and change the temperature or applied field. In order to further investigate the anomalous flux expulsion within the NSF samples both temperature and field dependent measurements were taken. The results of these are presented in figure 3.11.

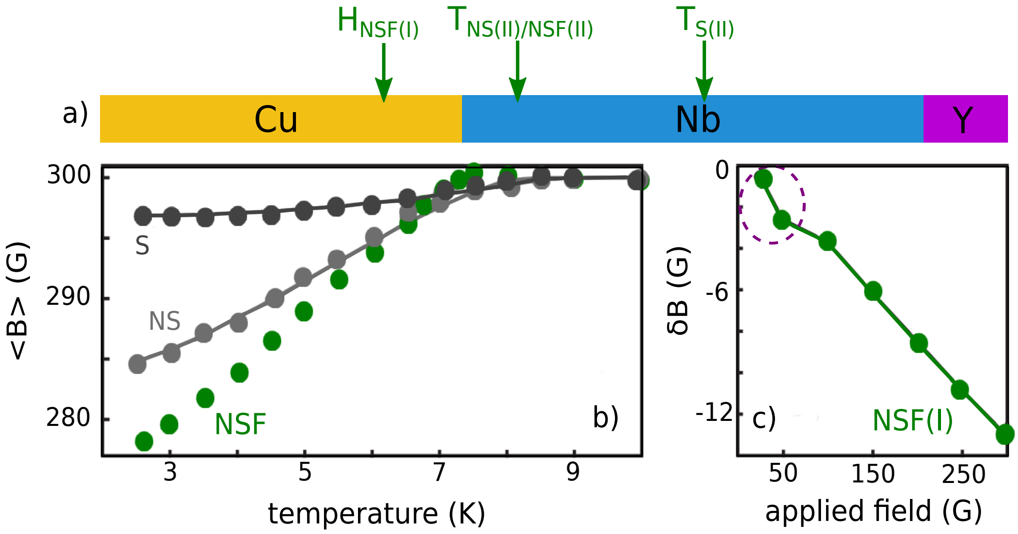

Figure 3.11: Temperature and field dependence of the LEμSR response. a) shows a schematic of the sample structure with the average probing position for each measurement indicated. b) The extracted $\langle B \rangle$ as a function of temperature are plotted as points for each of S(II), NS(II) and NSF(II). The solid lines represent the model responses calculated using the quasiclassical framework with all parameters determined from the S and NS modelling. c) flux lowering amplitude, $\delta B = \langle B_{2.5K} \rangle - \langle B_{10K} \rangle$, as a function of the applied field for sample NSF(I). The circled points highlight the results where the fitting becomes challenging. For lower applied field the error bars are therefore larger but still smaller than the symbol size.

---

[34] Indeed subsequent measurements, presented within chapter 5, on samples with insulating oxide barriers show unambiguously that the stray field is not the origin of the measured effect.

Figure 3.11a) shows a schematic of the general sample structure. The green arrows in each case indicate the average probing position of the LEμSR measurements. The results of the temperature scans are shown in figure 3.11b) where the plotted points represent the extracted $\langle B \rangle$ values and the solid lines show the quasiclassical calculations where all of the model parameters were fixed to experimentally determined values. For all the measured samples it is clear that the flux expulsion begins to develop for temperatures $T < T_c$. This can be seen in more detail within appendix D where the LEμSR data is shown alongside the corresponding transport T_c for each measured sample. In the case of S(II) and NS(II) the expected screening response with temperature was calculated, within the quasiclassical framework, and corresponds very closely with the experimental data. The measurements on NSF(II) could not be modelled in this way since it has already been shown that the quasiclassical description is not sufficient to describe the physics of this system. It is clear, however, that the screening response appears to increase linearly with decreasing temperature down to the base temperature of the system and shows no sign of levelling off. Figure 3.11c) presents the results of the field scan which was measured on sample NSF(II) at an average probing position as labelled by $H_{NSF(I)}$. The plotted points show the flux lowering amplitude, $\delta B = \langle B_{2.5K} \rangle - \langle B_{10K} \rangle$, as a function of the applied field. The results strongly suggest a linear dependence down to an applied field of 20 G and the data looks to extrapolate to $\delta B(0) = 0$ G. It is important to note, however, that transverse field μSR measurements become challenging for low applied field, see appendix E, since the spectra become more difficult to fit with certainty. Caution is therefore required when interpreting the circled data points. A more thorough investigation at zero field and in a different geometry would be necessary before any firm conclusions could be drawn regarding the zero field behaviour.

3.5 Discussion of the results on simple S, NS and NSF thin films

Whilst the results for the S and NS samples, that the flux expulsion of a mesoscopic superconductor can be greatly enhanced *via* proximity to a normal metal, may be surprising they can be very successfully modelled within the quasiclassical theory framework for dirty superconductors. Both the enhancement to the Meissner screening profile and the temperature dependence of the LEμSR response observed in experiment are highly consistent with the quasiclassical modelling where the parameters are fixed to values derived from the transport and muon measurements on these thin film systems. The NS sample structures appeared to be in a regime of behaviour where the bilayer screening response was equivalent to the corresponding thickness of bare niobium. This has important implications for the future modelling of LEμSR measurements on these systems where a London-like approximate profile can be imposed across the full bilayer. An approach which has the advantage of simplicity whilst still largely capturing the physics of the system. Within the following experimental chapters this approach has been applied to the data with great success allowing a more detailed quantitative analysis of the spatial data to be carried out. Whilst the NS proximity phenomena modelled within this section have been known about for some time, and probed *via* experiments on normal-metal clad superconducting wires [111–113], these measurements mark the first direct observation of the resultant spatial flux profile which shows excellent agreement with theory.

Extension of the quasiclassical theory modelling to include the effects of a ferromagnetic exchange field found a reduction in the flux expulsion which was associated with pair breaking effects. This, however, was not reflected in the total amplitude of the LEμSR experiments carried out on the NSF thin films where an anomalous enhancement was instead observed. This suggests that the quasiclassical theory description of these SF systems, and thus the model used to describe the experiments, is missing an important element. The linear response of the total trilayer amplitude with applied field is reminiscent of standard Meissner screening and suggests an orbital origin for the additional amplitude. The linear temperature dependence, on the other hand, does not immediately support this since a Meissner screening response to an applied field should be related to the pair density which does not develop linearly with temperature.[35] Unfortunately, the transverse field LEμSR measurements cannot distinguish between orbital and spin related phenomena since the probe is only sensitive the local flux. From these measurements alone, therefore, it is impossible to determine whether the anomalous amplitude is due to a screening current or, for example, a net magnetisation attributed to aligned spins within the system.

---

[35] The difference in the temperature dependence of NS(II) and NSF(II) suggests the additional effect increases linearly with decreasing temperature down to the lowest measured temperatures.

3.6 Conclusions and the electromagnetic proximity effect

In summary, low energy muon spin rotation has been used to observe the spatial distribution of magnetic flux within simple S, NS and NSF thin film structures. The measured samples belonged to two different growth series, sets I and II, each corresponding to a different growth quality of niobium. In the Nb(50) films a weak Meissner response was observed, $(0.3-1)\%$ of B_0, the amplitude of which was dependent on the niobium purity. Through modelling the spatial profile using the London theory, the penetration depths were determined to be 270 nm and 160 nm for S(I) and S(II) respectively. In the case of the Cu(40)/Nb(50) samples a significant increase in the flux expulsion was observed which extends across the full spatial extent of the bilayer. This effect could be successfully modelled and understood within the quasiclassical framework for dirty superconductors where many of the model parameters could be fixed to experimentally determined values. For the Cu(40)/Nb(50)/Co(2.4) thin films, in each case a further enhancement to the flux expulsion was observed. This was found to be inexplicable within the quasiclassical theory which instead would predict a reduction in the screening due to the pair breaking effects of the exchange field. Understanding the origins of this anomalous behaviour is vital since it represents a form of cooperation between ferromagnetism and superconductivity, where in the presence of the exchange field the properties of the superconductor appear to be enhanced, which is of fundamental importance to developing superconducting spintronics.

Following the publication of the results presented within this chapter [60], and other experimental results [39, 82], a flurry of theoretical papers have been published [40–42]. The focus of this theoretical work has been to describe the underlying mechanism through which the superconductivity is apparently cooperating with the ferromagnetism. In this new body of work a hitherto unknown type of proximity, the so-called electromagnetic proximity effect, has been described for the first time. Within the next chapter the results of analysing the LEμSR measurements within this new picture are presented.

4 | The electromagnetic proximity effect in SF thin film structures

The content of the present chapter largely comprises material published in [84]. This work takes the anomalous LEμSR results on the NSF thin film samples, discussed in chapter 3 and published in reference [60], and seeks to model them within the new theory of electromagnetic proximity. This presents an opportunity to test the new theory and to potentially understand the physical origins of the anomalous effect observed in [60]. In order to test the new theory one is required to demonstrate that the effect originates at the S/F interface, rolls off exponentially over a lengthscale dictated by the London penetration depth and is of a sign dependent on the orientation of the magnetisation of the F layer. To that end a series of experiments have been performed to test these three aspects of the theory within the context of our LEμSR measurements. The study comprises the following parts:

i) In the first part of the chapter the LEμSR data on the NSF(I) and NSF(II) thin films is re-analysed within the EM theory model. This involves imposing a slightly modified flux profile as will be discussed within section 4.3.1. In doing so, it is clear that the spatial dependence and lengthscale of the anomalous enhancement is well described by the EM theory.

ii) Whilst item **i)** provides evidence to support the origin of the anomalous enhancement being the S/F interface, in order to gain more resolution within this region of the sample an “upside down” trilayer structure is measured and modelled in the same way. The profile from part i) can be recycled and used to describe, to excellent accuracy, the results on the upside down structure. This strengthens the conclusion that the S/F interface region is the spatial origin for the enhancement.

iii) In the final segment of this chapter the focus is on whether or not the sign of the amplitude depends on the orientation of the magnetisation of the ferromagnet. In order to investigate this, LEμSR measurements were performed on a pseudo spin valve structure where the relative orientation of two ferromagnetic layers can be manipulated using an externally applied magnetic field. A change in the signal amplitude is observed as the two layers are rotated from a parallel to an antiparallel state. This provides a clear indication that the magnetisation is directly effecting the amplitude of the observed signal.

The results presented within the three parts of this chapter indicate that the newly described electromagnetic proximity effect is indeed a valid description of the anomalous enhancement observed in [60] and may, therefore, also be responsible for describing the behaviour observed in [39]. It is important to note that whilst the results presented here provide evidence for the observed enhancement being due to an additional source of vector potential at the S/F interface it cannot be definitively concluded from these results alone that the only source is the magnetisation of the F layer. There may, for example, be other contributions from spin-orbit or Rashba type effects at the interface which here cannot be distinguished.

4.1 Introduction

The interaction between superconductivity and ferromagnetism can be characterised by the competition between the superconducting gap, Δ, and the exchange energy, E_{ex}, of the ferromagnet. Within carefully engineered S/F thin films this has interesting consequences on the type of superconductivity present within the system. Ordinarily, the Cooper pairs within the superconductor are comprised of electrons with opposite spin and linear momenta but the ferromagnetic exchange field acts to align spins. The net result is a conversion of a fraction of the pairs from the conventional singlet state to an s-wave triplet state with odd frequency character. This has many repercussions for the behaviour of the superconductivity within the system and notably, especially within the context of the LEμSR measurements used here to probe these systems, the response of the condensate to an applied external field can be substantially altered from the conventional Meissner effect. Within the last chapter, an anomalous enhancement to the screening observed within NSF thin films, when compared with their NS counterparts of corresponding niobium purity, was reported. This was surprising since the quasiclassical calculations suggested a reduction in the screening amplitude, due to the pair breaking effects of E_{ex} strongly suppressing Δ near the S/F interface, ought to be observed instead. From these experiments, and others [39, 82, 85], it was concluded there was a vital element missing within the theory of S/F proximity systems. In an effort to fill this gap a new theory of electromagnetic proximity within S/F systems has since been developed which describes the leakage of a magnetisation from the ferromagnetic layer into the superconductor via the interaction of the condensate with the vector potential at the S/F interface.

Within this chapter the results of analysing the NSF trilayer data using the new theoretical perspective are discussed. In addition, a series of further LEμSR measurements which seek to test the main aspects of the new EM theory model will be presented. These involve probing the lengthscale, origin and magnetisation dependence of the anomalous trilayer enhancement by measuring a range of S/F hybrid structures using TF LEμSR.

4.2 Electromagnetic proximity

Before presenting the results of the LEμSR study a short synopsis of the new electromagnetic proximity theory, and how it relates to the direct and inverse proximity effects, is included for reference. The development of this theory provides a recent example of how theory and experiment can work well together to discover an entirely new and hitherto unknown effect. During the course of a single year a series of landmark theory papers have been published [40–42] in response to puzzling experimental results [39, 60, 82, 85]. The net result is a completely new understanding of S/F proximity systems which will prove to be crucial in further development of related technologies.

4.2.1 EM proximity phenomena within SF systems

When a superconductor is in direct contact with a ferromagnet, and electronic transport occurs across the interface between the two, unconventional superconducting states are generated. The mixing of the S and F orders involved in direct proximity is well understood and results in a number of interesting transport phenomena. These include, oscillations in critical temperature T_c (see for example [7–12]) and critical current (for example [13–16]), π phase shifts [17–20], colossal T_c suppression [21] and long range triplet supercurrents [22–29], and all rely on the conversion of some conventional singlet pairs into the odd-frequency s-wave triplet state. In addition to the direct proximity at the S/F interface the inverse proximity effect, which describes how through the transfer of spin polarised Cooper pairs across the interface the superconductor acquires a small net magnetisation, has been predicted [33–35] and until recently was thought to be the only mechanism through which a magnetisation could be transferred from the ferromagnet into the superconductor. This effect occurs over a lengthscale governed by the superconducting coherence length, ξ_s, which is typically only of the order of 10 nm. In more recent times, a series of puzzling experimental observations, made using neutron scattering [82, 85] and μSR [39, 60], as discussed within the previous chapter, have been published. These papers reported the long range transfer of a magnetisation to the superconductor which occurred over lengthscales far exceeding any coherence length phenomena and which therefore could not, at the time of publication, be explained within the existing body of theory. These results have motivated the development of the new theory of electromagnetic proximity [40–42].

In essence, the electromagnetic (EM) proximity effect describes how the interaction of a superconductor with the vector potential of a ferromagnetic layer influences its screening response. In the initial theory work the authors consider a simple S/F bilayer system and show that coupled to the direct proximity effect there is an additional electromagnetic component [40]. Within such a system, whenever transfer of electrons from S to F is allowed there will immediately be, as described in section 1, electron pair correlations induced within the ferromagnet. Since the ferromagnetic layer has a vector potential associated with its magnetisation, a screening current must then be induced in response over a lengthscale λ_L into the superconductor. This occurs as a consequence of the full system (superconducting layer and S/F interface) being described by a common superconducting wavefunction [40]. Since the lengthscale over which the condensate responds to this vector potential is governed by λ_L, where for a dirty system $\lambda_L \gg \xi_s$, this picture provides a natural framework in which to interpret the experimentally observed long range effects referenced previously. It is crucial to note that direct electronic contact between S and F is required to generate this effect because there must be superconducting currents inside the ferromagnet which experience its vector potential and consequently induce the screening response.

The new electromagnetic proximity mechanism is thus responsible for a modification to the orbital screening profile across the superconductor even in zero field. The spatial form of the induced response within the superconductor due to the EM proximity component is given by the expression shown in equation 4.1 [40]

$$B_z(x) = A_{EM} \exp\left((x - d_S)/\lambda_L\right) , \tag{4.1}$$

where A_{EM} is the strength of the EM proximity. The form given by equation 4.1 can be simply deduced using Maxwell's equations and the London relation though a more proper microscopic treatment using the Usadel formalism [136] has been shown to arrive at a consistent result [40, 41]. The EM amplitude, A_{EM}, is proportional to both the magnetisation of the ferromagnetic layer and to how the thickness of that layer compares with the coherence length within it. It therefore follows naturally that these parameters will determine both the sign and magnitude of the resultant effect and that consequently, depending on the material parameters of the system, the EM proximity amplitude may be paramagnetic or diamagnetic. A simple back-of-the-envelope estimate for a strong ferromagnet demonstrates that $A_{EM} \approx (10 - 100)\ Oe$ which is easily comparable the anomalous screening amplitudes discussed within section 3 [40].

Based on the discussion above it would be naively expected that in a spin valve structure, such as those studied experimentally in reference [39], the EM contribution would be maximised for a collinear arrangement of the ferromagnetic layers. This is in fact the opposite of what has been experimentally observed. In a detailed follow up work [41] the authors of the theory address the specific case of how the EM proximity manifests within these SFF spin valve structures and find, in fact, due to the appearance of additional equal spin triplet correlations the EM component to be maximised in the case of the noncollinear arrangement which agrees with the experimental results presented here.

4.2.2 Testing EM proximity within SF thin films

The EM proximity effect describes the spread of a magnetisation out of the ferromagnet and into the superconductor as a consequence of the condensate feeling the vector potential at the S/F interface. The main predictions of the EM proximity theory regarding the resultant modification of the spatial flux profile across the sample are as follows:

1) There should be an amplitude, originating at the S/F interface, that represents a non-zero offset in the flux profile when compared with the standard Meissner screening which necessarily goes to zero at the S/F and vacuum interfaces.

2) This amplitude should decay away exponentially over a lengthscale of the London penetration depth, λ_L, which is typically much longer than the superconducting coherence length, ξ_S.

3) The sign and magnitude of the EM amplitude should depend on the thickness of the ferromagnetic layer and the direction of its magnetisation.

When one considers these consequences of EM proximity, it becomes clear that LEμSR, being sensitive to the local flux, is the ideal choice of technique with which to probe the theory and as previously demonstrated in chapter 3 has been used extensively to measure novel effects within these S/F thin film systems.

4.3 Analysis of LEμSR measurements on SF thin films within the EM theory model

Within this section the results of modelling the LEμSR measurements within the new theory picture are presented. A good agreement between theory and experiment is observed for a range of different hybrid structures. Each of the different sample architectures allows a different aspect of the theory to be probed. In what follows they will each be addressed individually as a means to validate the new theory description.

The measured samples, as discussed in the previous chapter, fall into two different sets grown with differing niobium target purity. The analysis on the S(I) and S(II) samples allowed corresponding λ_L values of 270 nm and 160 nm to be determined. All other S/F sample architectures presented within this chapter fall into one of those two sets and will be compared against the relevant S and NS control samples. Since the measurements presented here were performed on samples from the same growth cycles corresponding to sets I and II from chapter 3 the reader is referred to sections 3.2 and 3.3 for information regarding the sample growth and characterisation respectively.

4.3.1 A new expected flux profile

In light of the results of the quasiclassical modelling presented in chapter 3 and the new theory of electromagnetic proximity, it is now possible to construct a model profile which captures both the Meissner screening response of the full bilayer section and the EM contribution originating at the S/F interface. This latter contribution we know to arise as the result of spontaneous screening in response to the vector potential of the magnetisation of the F layer. This generates a magnetic flux inside the superconductor over a characteristic lengthscale given by the London penetration depth. The results of the LEμSR measurements on NSF thin film structures in an applied external field will therefore represent the sum of these two contributions. In this section the form of the total expected flux profile for our thin film samples will be given such that in later sections it may be imposed upon the data.

As previously discussed in chapter 3, the form of the Meissner screening profile for a superconductor with vacuum interfaces is given, within the London theory picture, by equation 3.4. The analysis on thin film niobium samples presented in the previous chapter demonstrated that this form provides an appropriate description of the behaviour of the systems studied. The results of the LEμSR measurements on the NS bilayer systems and the corresponding quasiclassical modelling illustrated that for the specific combination of sample material parameters within these measured systems the screening profile extends across the full spatial extent of the bilayer in a near symmetric fashion. As such, the Meissner part of the flux profile can be modelled, to good approximation, using the form in equation 4.2

$$B_{NS}(x) = B_0 \cosh\left(\frac{x}{\lambda_L} - \frac{d_{NS}}{2\lambda_L}\right) \cosh\left(\frac{d_{NS}}{2\lambda_L}\right)^{-1} , \qquad (4.2)$$

where as usual λ_L is the London penetration depth, which may now be altered with respect to the original niobium thin film, and d_{NS} is the full thickness of the bilayer section. In order to describe the full profile for the NSF trilayer samples the form of equation 4.2 is modified to account for the EM proximity contribution which occurs at the S/F interface and decays exponentially over a lengthscale governed by the London penetration depth as shown in equation 4.3

$$B_{NSF}(x) = B_{NS} + A_{EM} \exp\left((x - d_{NS})/\lambda_L\right) , \qquad (4.3)$$

Where A_{EM} represents the strength of the electromagnetic proximity effect.

Figure 4.1 presents a plot of the full flux profile given by equation 4.3 that has been scaled to the usual applied LEμSR measurement field.

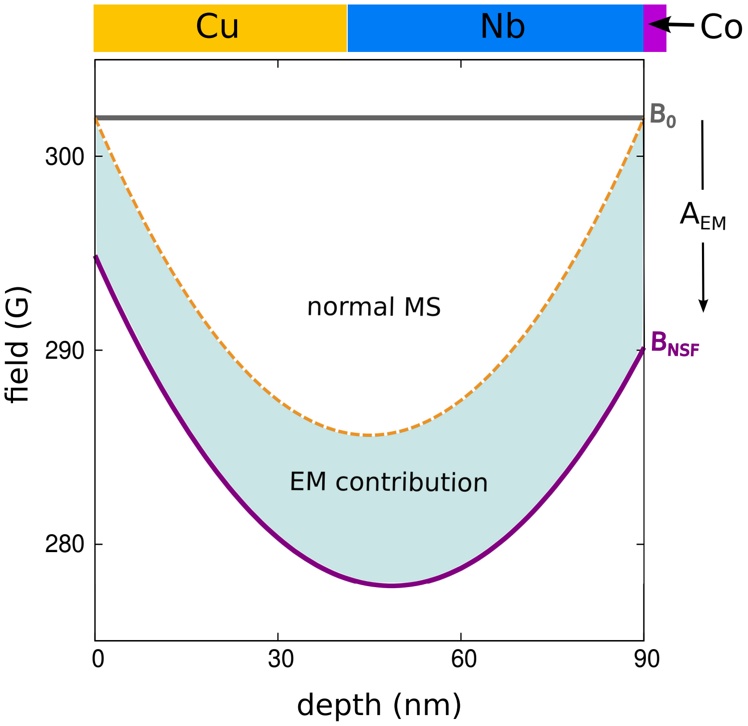

Figure 4.1: A schematic of the full model screening profile, B_{NSF}, decomposed into its Meissner (dashed line) and EM (shaded region) contributions. The profile has been scaled to the applied measurement field.

B_0 is the externally applied magnetic field which is recovered in the normal state measurements. B_{NSF} is the full superconducting state profile which is decomposed into its constituent parts: the Meissner screening of the NS bilayer section (dashed line) and the EM contribution (shaded region) of amplitude A_{EM}. A simple direct comparison of the B_{NSF} profile plotted in figure 4.1 with the trilayer results in figure 3.9c) immediately shows the new expected flux profile has the potential to describe the observations made through experiment. In addition, if one refers back to figure 3.10, where the difference in bilayer and trilayer signals was plotted as a function of the average probing depth, it is clear the proposed EM contribution could describe the spatial dependence of the anomalous discrepancy, at least at first glance.

4.3.2 Modelling NSF(I) and NSF(II)-magnitude and spatial dependence

Within this first section the LEμSR results on NS and NSF thin films from the previous chapter are reanalysed. The new data analysis involves taking a similar approach to that used in section 3.4.1 where a full spatial profile was imposed on the measured averages. As discussed within section 4.3.1, if one inspects the previously discussed results of the conventional analysis, and considers the shape of the profiles hinted at by the average results, it is clear the Meissner profile given by equation 4.2 is an appropriate choice for the bilayer[36] and that the addition of an EM term seems appropriate to describe the observed discrepancy for the trilayer samples. This suggests we ought to expect a good agreement between the new flux profiles and the average results presented in the previous chapter. Here the profiles, given by equations 4.2 and 4.3, are imposed on the measured flux averages in order to investigate whether the origin and spatial dependence of the measured effect is consistent with the EM theory.

Before the results are presented it is important to discuss how the profiles were imposed on the data. It is of course true that an additional term, such as the one in equation 4.3, will provide additional fit parameters and may therefore provide an improved fit by virtue of an additional freedom within the model. Importantly, in this case the new tuning parameter provides the means to directly describe a new effect and so is physically justified. It is im-

---

[36] This is also clear from the results of the quasiclassical modelling as previously discussed in chapter 3

portant to stress, therefore, that should the fit be improved, it is so because the new model accounts for new underlying physics occurring at the S/F interface and its resultant effect on the spatial flux profile. However, it is still important to take a careful and consistent strategy when imposing the profiles on the measured data. The approach taken here was to first fit the Meissner profile to the bilayer sample for each of Sets I and II. In doing so a value for λ_L, and a subsequent normal screening amplitude, was determined for each niobium quality. The Meissner term of the full EM profile, given by equation 4.3, could then be fixed to that form for the corresponding trilayer samples such that the only tuning parameter for the NSF structures was the strength of the EM proximity, A_{EM}. This approach of course assumes the effect of pair breaking on the screening profile is negligible.

Figure 4.2 shows the results of analysing the NS bilayer and NSF trilayer samples using the new approach outlined above.

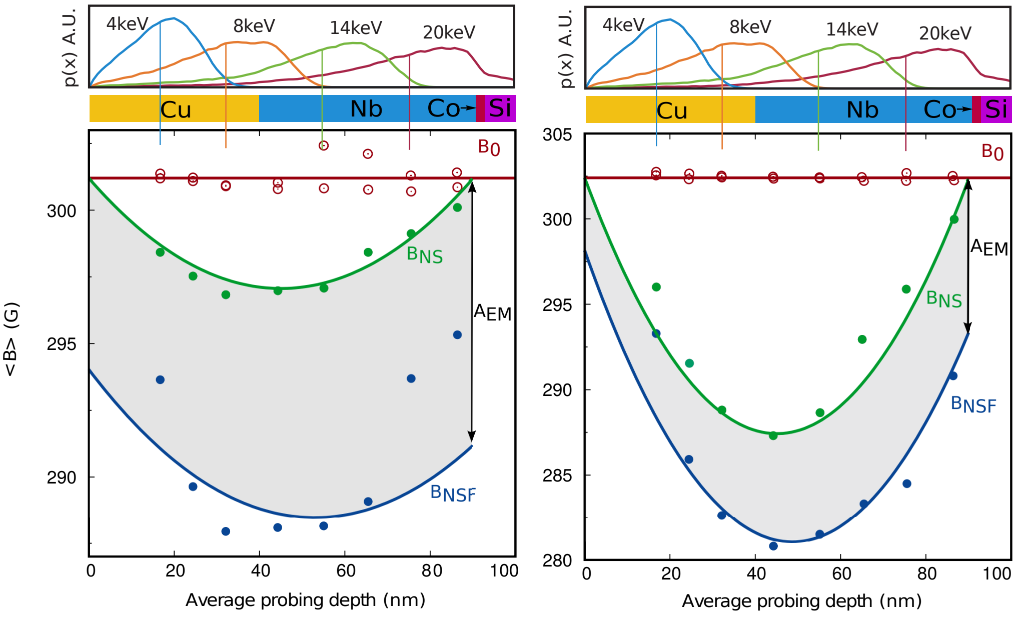

Figure 4.2: The results of imposing the EM model on left: NSF(I) and right: NSF(II). In each case the top panel presents some sample muon stopping profiles with the vertical lines indicating the corresponding average probing depths. For both sets, the normal (superconducting) state averages are plotted in open (closed) symbols and the solid lines show the resultant best fit profiles imposed on the data. B_0 is the constant normal state profile whilst B_{NS} and B_{NSF} are the data for the bilayer and trilayer respectively. In each case the shaded region represents the EM proximity contribution of amplitude A_{EM} found from the fits.

The results for sets I and II are shown in the left and right panel respectively. In the top segment of each panel are plotted the usual sample stopping profiles with the vertical lines indicating the average probing depths for each energy. The solid lines in each of the bottom panels represent the best fit profiles, B_0, B_{NS} and B_{NSF}, found from imposing the analytical form of B(x) on each measured data set as appropriate. All normal and superconducting state averages, found from the conventional approach to the analysis, are also plotted in open and closed symbols respectively for comparison to the profiles. As always, the normal state measurements were conducted at a temperature of $T = 10\ K$ and the superconducting state was measured at $T = 2.5\ K$. In the case of the normal state measurements, as would be expected, the externally applied field is recovered which in each case was set to approximately 300 Oe. For the two bilayer samples the analytical form shown in equation 4.2 was imposed on all data simultaneously using λ_L as the tuning parameter. The best-fit λ_L for each bilayer would be expected to be shorter than the corresponding values for the single niobium layers, which were found to be $(270 \pm 5)\ nm$ and $(160 \pm 2)\ nm$ respectively, since the copper boosts the screening response significantly. For sets I and II the extracted values of the penetration depth were $(240 \pm 3)\ nm$ and $(140 \pm 1)\ nm$ which when compared with the single niobium layers are indeed shorter. In each of the left and right panels a close correspondence between the best fit profiles and the flux averages is evident across all energies for the bilayer samples showing the choice of flux profile is indeed an appropriate one. The extension to the modelling of the trilayer data then involved imposing equation 4.3, where the London term was fixed to the corresponding bilayer result, on all the measurements for a given sample simultaneously. The resultant best fit profiles correspond to EM proximity amplitudes of $A_{EM} = (10.4 \pm 0.5)\ G$ and $A_{EM} = (10.0 \pm 0.2)\ G$ for sets I and II respectively. The extracted average flux values reflect the same underlying shape but with differing amplitudes due to the variable Nb quality. For these trilayer samples the correspondence between the two methods of analysis is not uniform across the full set of measurement energies. In particular, at the lowest and highest muon probing energies for each sample the average result falls more rapidly towards zero than the spatial profile would suggest. This reflects the simplicity of the imposed model with its underlying assumption that the standard screening is symmetric. Neither the possibility of pair breaking nor the effect of limited sample thickness on the decay of A_{EM} is explored within the current model.

The results of modelling the trilayer profiles, B_{NSF}, highlight some interesting points for discussion. For both sample sets the extracted values of A_{EM} are within error or each other. This would be expected since the Co layers are of equivalent thickness and were grown under the same conditions. The only difference between the samples is the quality of the niobium layer. As is evident from equation 4.3 this will have an effect on the lengthscale over which the amplitude rolls off since this is given by λ_L. This is also visible in the data. When one considers the overall shape of the shaded region for each sample set, much of the amplitude rolls off over the thickness of the bilayer section in the case of NSF(II) but not for NSF(I) where the EM contribution is largely flat. This is also visible in the marked asymmetry in the profile for NSF(II) which resulted in a much easier and more reliable fit since the EM contribution is very distinct from the symmetric Meissner part. In the case of the higher purity niobium target the best fit profile is a close match to the behaviour of the flux averages across most energies with the exception of the point at $E_{\mu} = 4\ keV$. Here the model profile starts to deviate from the average data which closely coincides with the Meissner model of the bilayer. In order to investigate this in more detail it is possible to impose the model function, equation 4.3, on each measured spectrum independently such that a plot of the EM amplitude as a function of the average probing depth can be determined. Figure 4.3 shows the result.

The plotted points in figure 4.3 represent the extracted values of A_{EM} as a function of the average probing depth. These values are the result of finding the best fit of equation 4.3 individually for each measurement energy. The dashed line indicates the value of A_{EM} found when all measurement energies were fitted simultaneously. Two things become apparent when one considers the results of this energy dependent analysis. Firstly, when A_{EM} is treated as a free parameter for each probing energy individually it is clear that towards the surface region of the sample the EM amplitude is rolling off much more rapidly than expected. Indeed for $E_{\mu} = 4\ keV$, the point corresponding to the smallest average probing depth, there is almost no EM contribution remaining whilst for all other measured energies the value of A_{EM} sits within the range $(-10 \pm 2)\ G$. Secondly, there appears to be a reduction in the extracted amplitude for the higher probing energies when compared with those primarily sampling far away from the ferromagnetic layer. It seems likely this is due to the effects of pair breaking at the S/F in-

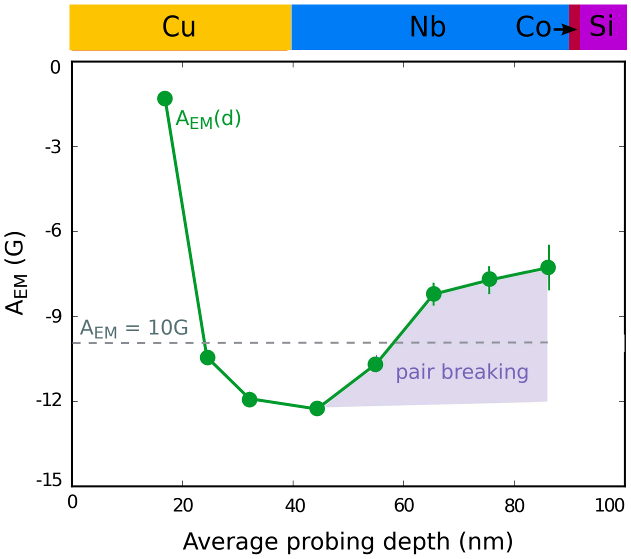

Figure 4.3: A plot of A_{EM} as a function of the average probing depth. The plotted points show the extracted values of A_{EM} from the fit made to each probing energy individually. The dashed line indicates the best fit A_{EM} from the analysis which imposed the profile on all energies simultaneously. The shaded region represents the possible effect of pair breaking.

terface.[37] In the implementation of the model used here, such pair breaking effects would manifest as a reduction in the amplitude of A_{EM} for sampling energies which probe close to the interface region since the Meissner contribution is fixed to the bilayer response. This trend is indicated by the highlighted region in figure 4.3.

The sizeable diamagnetic amplitude, with an origin seemingly localised to the S/F interface, and the decay lengthscale being consistent with the field penetration depth rather than any coherence length provides good initial evidence for the EM proximity theory. Unfortunately, seeing as the thickness of the bilayer section of the measured samples is less than the respective value of λ_L it is not possible to conclude with complete certainty that the amplitude rolls off over λ_L. Indeed the theory is for a system where $d_S \gg \lambda_L$ and so it is not known how the bilayer thickness will limit the EM proximity effect. From the results presented in figure 4.3 it appears, however, that the model is an excellent description for all energies except 4 keV which suggests the EM component rapidly goes to zero near the vacuum interface where $d_{NS} < \lambda_L$. Further experimental evidence for this is shown in appendix F where some data on gold capped samples is presented. The

---

[37] This hypothesis is tested further within chapter 5.

thickness of the measured NSF samples is somewhat limited by the need to probe the physics close to the S/F interface. The incoming muons are of energies within the range $(4-24)$ keV which corresponds to probing depths of up to 100 nm. If the combined thickness of the copper and the niobium is too great then the muons cannot reach the S/F interface region. Additionally, as the muon energy increases the stopping profile spreads out which results in a lower spatial resolution. In light of this, within the next section the results of measurements on a reversed trilayer structure, where the S/F interface region is probed in more detail, are presented.

4.3.3 Reversed trilayer sample: the Nb/Co interface in more detail

In order to investigate the S/F interface in more detail a reversed trilayer sample was grown and measured in the same way as the standard layout. This sample was grown using the lower purity niobium target, with a known penetration depth of $\lambda_L = 270$ nm for a single Nb(50) layer, in the same vacuum cycle as NSF(I) which is therefore the relevant sample for comparison. The full sample structure was as follows: Cu(40)/Co(2.4)/Nb(50)/Cu(40)/Si, where the bracketed numbers indicate the layer thicknesses in nanometers. The top copper layer acts both as a protective cap and ensures the muons are slowed down and stop predominantly within the S/F interface region. When the muons are incident on this sample layout they first encounter the copper capped cobalt layer, rather than the bilayer section of the sample, and can therefore probe the S/F interface with a greater precision since the stopping profiles are sharper for lower probing energies. Due to the finite sampling width of each stopping profile it is not possible to probe the interface region with complete certainty but by scanning the incoming muon energy an effective spatial resolution of $(10-20)$ nm can be achieved. The results of the energy scan on the reversed trilayer structure are presented in figure 4.4. In the top panel are shown the stopping profiles for the reversed trilayer which look quite different from those for the standard layout. For each sampled energy the vertical lines indicate the corresponding average stopping position. At energies $E_\mu \leq 5$ keV all of the muons stop within the copper capping layer. As the probing energy is increased the stopping profiles start to sample both the interface region and the superconducting layer. The bottom panel of figure 4.4 presents the results of the LEμSR measurements on the inverted trilayer structure along with a direct comparison to the best fit profile found for the corresponding standard trilayer NSF(I). The data points represent the extracted flux averages found from the conventional analysis. The open symbols are for the $T = 10\ K$ normal state measurements, where the applied field B_0 was once again recovered, and the closed symbols correspond to the superconducting state measurements conducted at $T = 2.5\ K$. At the lowest sampled muon energy, $E_\mu = 5\ keV$, the superconducting and normal state average flux values coincide with each other within error. This suggests that little to no screening current manages to pass through the cobalt layer into the copper cap.

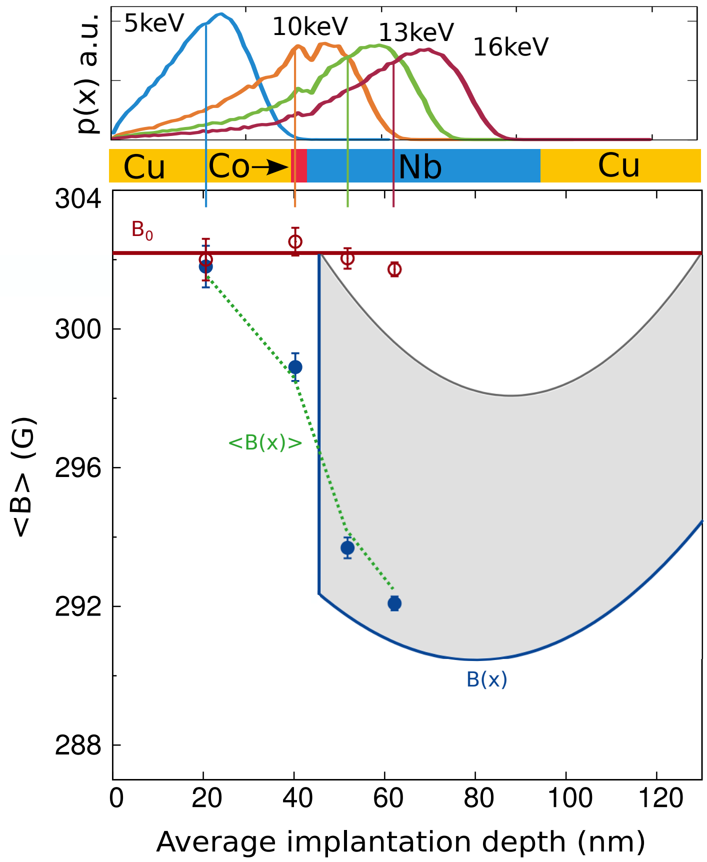

Figure 4.4: LEμSR results on the inverted trilayer. Top panel: stopping profiles with the average probing depths indicated by vertical lines. Bottom panel: results of imposing the best fit $B(x)$ of NSF(I) on the reversed trilayer data. The open (closed) symbols represent the flux averages measured in the normal (superconducting) state. B_0 is the applied field and B(x) is the field profile found for NSF(I), the averages of which ,$\langle B(x)\rangle$, match well the reverse trilayer data. The shaded region shows the EM contribution.

This would be expected since the coherence length of the pairs within the strongly ferromagnetic Co layer is only of the order of a nanometer. As the muon energy is increased and the stopping distributions start to sample the S/F interface and superconducting layer a strong diamagnetic signal rapidly develops before beginning to level off at the higher measured energies. In order to compare these results with the NSF(I) standard trilayer sample a direct comparison was made to its best fit form of equation 4.3. To achieve this the best fit profile was inverted to match the new structure and the applied measurement field adjusted to match the precise value used for the measurements on the inverted trilayer. The resultant profile is plotted in figure 4.4 and labelled as $B(x)$. The shaded region represents the EM contribution to this profile and the standard Meissner component is indicated by the cosh form plotted across the bilayer section. It is difficult to tell simply by looking at the form of $B(x)$ whether or not it describes the average data well. It becomes much more apparent when one calculates, using equation 2.11 as described in section 2.1.7, the average of the full form of $B(x)$ sampled by the relevant stopping profiles $p(x)$. The results of this analysis are indicated by the green dashed line labelled $\langle B(x) \rangle$. For all measured energies $\langle B(x) \rangle$ shows an excellent correspondence to the flux averages.

The analysis presented within figure 4.4 provides very strong evidence for the EM theory description being at the very least a realistic description of the data. Simply by taking the best fit model $B(x)$ found for the NSF(I) standard trilayer sample, inverting the profile in x and adjusting the value of B_0 to match experiment, the data on the inverted sample can be described to an excellent degree of accuracy. In this inverted structure the S/F interface region is probed in more detail and the model still describes the data extremely well. It is important to note, however, that due to the finite width of the muon stopping profiles it is possible that the feature at the S/F interface could be more smoothed out. For example, there could be a rapid decay of the amplitude into the copper layer. This seems unlikely given the lowest measured data point matching the applied field so well but cannot be completely ruled out due to the limited spatial resolution of $(10-20)$ nm. It is clear, however, that the behaviour is highly distinct from the standard Meissner response which goes to zero at the S/F interface and which could therefore not describe the observed data points alone.

4.3.4 Pseudo spin valve structures and the dependence on orientation

The final aspect of the LEμSR observations to be tested within the context of the EM theory is whether or not the flux lowering changes sign with the magnetisation of the cobalt. In order to investigate this a pseudo spin valve involving two ferromagnetic layers was developed. This involved taking the usual trilayer layout and inserting a second thinner cobalt layer at the top with an additional copper cap. The full structure, Cu(40)/Co(2)/Cu(40)/Nb(50)/Co(2.4)/Nb(3)/Si, was grown as part of sample Set I. In making the top cobalt layer thinner it is possible to switch between a parallel and an antiparallel alignment of the exchange fields of the ferromagnetic layers simply by sweeping the field. This relies on the two ferromagnetic layers having different switching fields. The switching behaviour of the pseudo spin valve is illustrated in the top right panel of figure 4.5 which presents an MH loop measured at a temperature of 50 K using the SQUID magnetometer. At an applied field of -500 Oe both the top and bottom cobalt layers are saturated and have an orientation parallel to the applied field. As the external field is swept upwards, the Co(2.4) switches first at around 50 Oe. The system is now in the antiparallel configuration (AP) since the orientation of the Co(2) layer is still opposite to the applied field. As the field is further increased to 300 Oe the thinner Co(2) layer finally switches and the parallel state (P) is recovered. LEμSR measurements were therefore performed at $B_0 = 150$ Oe in the AP state and $B_0 = 300$ Oe in the P state with saturation performed at $B_0 = 500$ Oe between measurements. The pseudo spin valve sample layout allows a number of important aspects of the EM proximity theory to be investigated. The system comprises two separate regions of interest: the Co(2)/Cu and Nb/Co(2.4) interfaces. Owing to the different switching fields for the two cobalt layers the dependence of A_{EM} on the orientation of the magnetisation at the Co(2)/Cu interface can of course be tested. Additionally, since the two ferromagnetic layers are of different thickness and the theory expects the sign of A_{EM} to flip as d_F is tuned through a lengthscale of ξ_F, which for these layers is around 1 nm, the signals coming from each Co interface could be very different.

The results of the LEμSR measurements conducted to probe these effects are presented in figure 4.5. For both of the measurement orientations the Co(2.4) layer is parallel to the applied field and the Co(2) is either parallel or antiparallel as indicated. The top left panel of figure 4.5 presents some sample muon stopping profiles for the pseudo spin valve structure. For most energies the majority of the muons stop within the two copper layers, only reaching the niobium layer for $E_\mu \geq 20\ keV$. Seeing as a small fraction of the muons stop within the Co(2) layer, and the depolarisation rate is higher due to stray fields, the error bars on the average field values are expected to be larger for lower probing energies. In order to combat this a higher number of counts, 9 million events compared with the usual 2.5 million, were detected for the lower probing energies to improve the statistics. The results of the muon energy scans for the parallel (left) and the antiparallel (right) states are presented in the bottom panel of figure 4.5. The results of the conventional averages approach to the data analysis are represented by the plotted points.

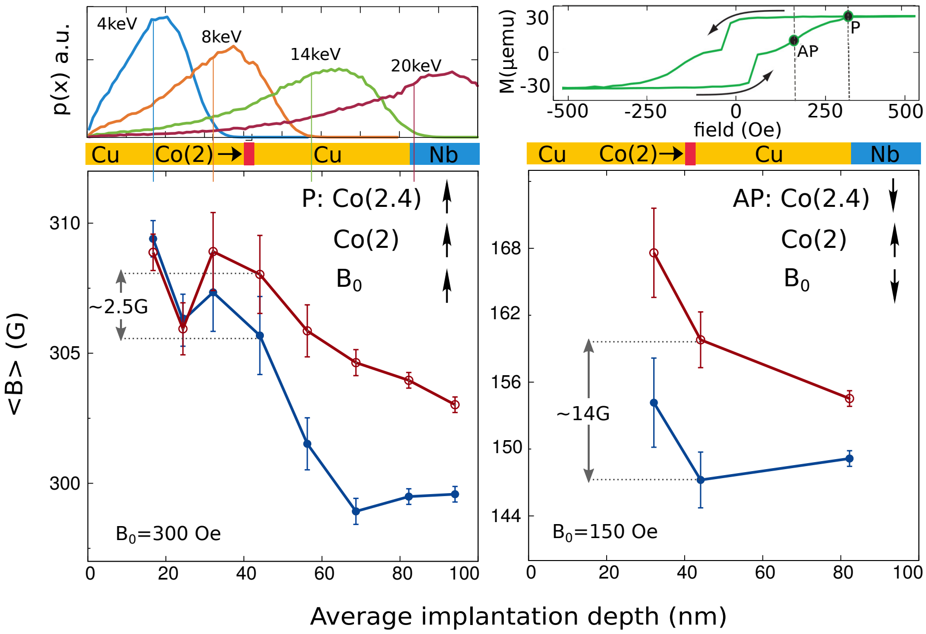

Figure 4.5: Measurement results for the pseudo spin valve structure. Top left: sample muon stopping profiles for the pseudo spin valve structure. Top right: magnetisation measurements showing the switching behaviour of the Cobalt layers. The two measurement fields are marked P and AP and indicated by the dashed lines. Bottom panel: LEμSR results for the parallel (left) and antiparallel (right) states of the pseudo spin valve. All open (closed) symbols correspond to the normal (superconducting) state results which were measured at $T = 10\ K$ and $T = 2.5\ K$ respectively. The lines are a guide to the eye and the key indicates the relative orientation of the exchange fields with the applied field B_0.

The open and closed symbols correspond to the normal and superconducting state measurements which were conducted at $T = 10\ K$ and $T = 2.5\ K$ respectively. In all cases the lines are just a guide to the eye. It is immediately clear that the flux expulsion measured in the superconducting state at 2.5 K, when compared with its respective 10 K normal state value, is significantly larger in the AP state than it is in the P state. This is especially marked close to the Co(2)/Cu interface. Here in the P state the total flux expulsion almost entirely disappears ($\approx 2.5\ G$ as marked) where in the AP case it looks to be maximal ($\approx 14\ G$ as marked). It is important to stress how dramatic this effect is given that the AP state was in fact measured at half the applied field of the P state. Interestingly, when one compares the results in the parallel geometry to the measurements on the bilayer from sample set 1 it can be seem the observed signal amplitudes, 4.5 G for NS(I) and 5.5 G for the P state of the pseudo spin valve, are closely comparable. It seems highly plausible therefore, given that the behaviour of the Nb/Co(2.4) interface is well characterised, in the P state there are two approximately equal but opposite EM contributions which cancel each other out. The two interfaces behave differently. Whether or not the difference in the contributions observed for the P state is because of the thickness of the respective cobalt layers or to, for example, a different behaviour at the Co(2) interface due to the proximity induced superconductivity in the copper cannot be determined with certainty at this stage.

When taken together these results allow the character of the superconducting pairs present at each cobalt interface to be ascertained since singlet and triplet pairs produce a diamagnetic and paramagnetic screening response respectively. In the case of the Nb/Co(2.4) interface, where the cobalt layer magnetisation is aligned with the applied field, a large diamagnetic contribution to the overall muon signal is observed. This can be deduced most cleanly from the measurements on the standard trilayer structures presented in section 4.3.2. In light of the diamagnetic contribution this implies the screening pairs close to the Nb/Co(2.4) interface are predominantly of singlet character. Conversely, the results of mapping out the screening profile for the pseudo spin valve suggest the dominant pairing at the Co(2)/Cu interface is of a triplet nature. This can be concluded since the contribution at this top interface is opposite and the overall amplitude of the signal in the P state is reduced when compared with the AP state.

These results hint at several possibilities to utilise the EM proximity effect. Firstly, it appears to provide a proxy to measure the pairing character present within a given system. Secondly, the results on the pseudo spin valve in particular, and on previous measurements made on similar S/F systems [39], hint at the possibility of a device where the presence of a spin polarised supercurrent running along an interface, in this case the Co(2)/Cu, can be controlled simply by tuning an applied external field. This latter statement requires further carefully controlled measurements of how the EM contribution depends on the ferromagnetic layer thickness and on the relative orientation of the exchange and externally applied fields. These measurements therefore provide a good first proof of principle for such a scheme, and provide further evidence for the applicability of the new EM theory model to these proximity systems, but more systematic measurements would be required before such a device could be designed.

4.4 Conclusions of the EM proximity modelling and further experimental tests

LEμSR has been used to map out the spatial flux profile across a variety of different S/F hybrid systems. Through careful modelling of these results, accounting for the new theory of electromagnetic proximity, a strong correspondence between the experimental observations and the theory has been demonstrated. This is particularly evident when one considers the spatial origin and decay lengthscale of the previously anomalous component to the measured flux profile which, as is expected of an EM proximity effect, appears to be well described by an amplitude originating at the S/F interface that decays away spatially over a lengthscale comparable to λ_L. This EM component is found, through measurements on a pseudo spin valve structure, to be dependent both on the thickness of the associated ferromagnetic layer and on the orientation of its exchange field. When taken together all of these observations demonstrate the accuracy of the main predictions of the new EM proximity theory and show its relevance in describing the physics within S/F hybrid systems. Furthermore, the results on the pseudo spin valve structure imply the possibility to both use the EM proximity amplitude as some measure of the dominant pairing character at a given interface and to tune, using an applied external field, a spin-polarised current running along an F/N interface. These two observations are of essential interest to superconducting spintronics.

Where the previous theoretical picture could not capture the additional screening component at all, this new theory goes a long way to successfully describing the experimental observations. It does, however, pose some new questions. In particular, the theory would predict a non-zero screening response at zero applied field. To date this has not been observed and is not accessible to this measurement technique, in this measurement geometry, since it requires the application of a weak transverse field. In fact, if anything the results presented within this chapter, and the previous, seem to tentatively suggest the observed EM component disappears in the absence of an applied field. Moreover, the results presented in appendix F on the Au(5)/Nb/Co trilayer show the striking reduction in the EM amplitude to $\approx 1\ G$ when compared with the $\approx 10\ G$ measured for these NSF trilayer systems. In this case, the absence of a thick normal metal cap prevents the boosting effect to the Meissner screening amplitude provided by the normal metal proximity effect. The circulating screening current is therefore weaker, only managing to screen $\approx 0.3\%$ of the applied field, and a greatly reduced EM component appears at the Nb/Co interface. These observations, in combination with the field dependence results on NSF(I) presented in chapter 3, strongly imply the Meissner current is somehow driving the EM effect in these systems. This is contrary to the existing theory picture which states the origin of the EM proximity effect is simply the superconducting condensate interacting directly with the vector potential of the ferromagnetic layer. It is important to note that the measurements presented within this chapter cannot and do not definitively pin down the source of the EM proximity effect. Further measurements, both in zero field and which explore the details of the physics occurring at the S/F interface, are required to draw firm conclusions regarding the origin of the observed EM component.

Although not explored within this chapter, the results reported in reference [39] on pinned superconducting spin valve structures which initially motivated these measurements on more simple structures can also be naturally explained within this picture of electromagnetic proximity. The experimental observations indicate a substantial diamagnetic enhancement to the measured flux profile in the non-collinear state when compared with the collinear state. As has been demonstrated in reference [41], using realistic sample parameters for the gold, niobium and cobalt layers, this is precisely what the theory would predict. As discussed in section 4.2.1, although surprising in the sense one might naively expect a maximal response for a maximal magnetisation (i.e. the parallel state) this is due to the generation of equal spin triplet pairs in the presence of an inhomogeneous exchange field. These act to boost the EM response since they provide an additional net magnetisation.

Finally, theory suggests that the magnetic field induced in the superconductor by the presence of the ferromagnet has both a long range and short range component [42]. The short range component is related to the inverse proximity effect which extends only over a lengthscale of ξ_s which for these sputtered niobium thin films is only $\approx 10\ nm$. The long range component, on the other hand, is generated by the EM proximity effect over λ_L. It seems that for realistic material parameters, at least for strong ferromagnets where the exchange energy is large, the long range component dominates [39, 41, 60]. Irrespective of the relative size of the two contributions it is also important to note that due to the nature of the muon stopping profiles specific information about the short range spin component of the signal would likely be washed out. In light of this is is highly likely that any measurements of the spatial flux profile will detect at best the sum of all the terms and would be very hard pushed to disentangle the different contributions to the signal. Additional evidence for this can be seen when one considers the shape of the standard Meissner component of the signal in the NSF system. Despite there being a pair breaking effect near the S/F interface, which effects the amplitude of the total signal as shown in figure 4.3, the overall shape remains relatively symmetric. This implies the spatial resolution near the buried S/F interface is not sufficient to capture phenomena occurring over a coherence length within these systems.

5 | Controlling EM proximity by tuning the mixing between superconducting and ferromagnetic orders.

The results presented in the previous chapter show the new EM proximity theory can be used to successfully model the influence of the interaction between superconductivity and ferromagnetism on the flux profile. The main aspects of the new theory were tested and the spatial dependence, magnitude and magnetisation dependent sign of the EM effect were all readily demonstrated. This indicates that the effects reported in references [39, 60], which at the time of their publication were anomalous, can be explained within this new theoretical picture. In order to investigate the S-F coupling dependence and origin of the EM effect, however, a more systematic study is required.

Within this chapter, to test the origin of the EM amplitude at the S/F interface, the degree of coupling between S and F is controlled through the insertion of insulating oxide barriers (I) of variable thickness. The aim being to push beyond the theory and investigate how the EM proximity develops as a function of the mixing strength between superconducting and ferromagnetic order and how it relates to the direct proximity effect. Since direct proximity is dependent on the contact term in a known way it ought to be possible to disentangle the effects of EM proximity and pair breaking on the flux profiles such that knowledge of how the two effects relate to one another can be accessed. To achieve these aims low energy muon spin rotation measurements were carried out on a set of NSIF thin film structures with variable insulator thickness. The full screening response of the proximitised system was determined in each case and a non-monotonic behaviour of the total flux expulsion as a function of the insulator thickness observed. This total signal can be decomposed into two separate components: the effect of pair breaking on the normal Meissner screening, which was eluded to in the previous chapter, and an EM proximity contribution. The amplitude of each contribution as a function of the insulator thickness could then be determined. Curiously, whilst the pair breaking amplitude decays away with increasing barrier thickness as expected, the EM amplitude appears to be relatively constant up to thicknesses of 4 nm before diminishing to zero for thicker barriers.

The work which forms the basis of this experimental chapter can be found published in [83]. It highlights the need to extend the theory further such that the interplay of the two proximity mechanisms: the pair breaking effects which result from direct proximity and the electromagnetic proximity effect itself, can be described. The results suggest the possibility to design devices where the pair breaking mechanism can be minimised whilst still maintaining a maximal electromagnetic effect.

5.1 Samples and experimental design

In order to control the degree of coupling between the superconducting and ferromagnetic layers, insulating barriers of variable thickness were used as spacer layers. The full sample structures were of the form NSIF where N = Cu(40), S = Nb(50), F=Co(2.4) and I = $\mathrm{AlO}_x(\mathrm{d}_\mathrm{I})$ with dI = (0,2,4,6,8) and all bracketed thicknesses in nanometers. The samples were once again grown on Si(100) substrates using the same growth systems and procedures as described in previous chapters. The one difference now being the addition of the insulating layer, the reasoning behind which was to mediate the contact term between the superconducting condensate and the vector potential of the ferromagnetic layer. The purpose of this systematic set of samples was to investigate the origins of the EM proximity effect and its relation to direct proximity. In order to achieve this aim, a careful control of the oxide barrier growth and the niobium quality was required. Within this section details of the sample growth and characterisation are given such that the results of the muon experiments in the later subsections can be successfully interpreted.

5.1.1 Oxide barrier growth and sample characterisation

Growth of all the material layers was carried out at ambient temperature, at a base pressure of 10^{-8} $mbar$ and under a standard Argon flow of 26 $sccm$. All samples measured as part of this study were grown in two separate vacuum cycles with corresponding control samples to allow comparison between the sets. The cobalt layers were deposited atop a 3 nm thick non-superconducting niobium buffer layer. The purpose of this seed layer was to provide a lattice matched substrate on top of which the cobalt could be grown cleanly. This ensured the magnetic and structural roughness around the SIF interface region was minimised and consequently that the associated generation of stray fields would also be kept to a minimum. Whilst this is usually done simply to reduce the muon depolarisation rate, and therefore improve the measurement signal, for this study it is of particular significance since any sample to sample variation in stray field generation should be minimised to rule out any associated influence on the observed flux profile. As such a fine control of the sample structure is required such that to good approximation only the thickness of the oxide barrier changes. As described previously, the growth rates of each target were calibrated through fits to Kiessig fringes measured *via* low angle X-ray reflectivity on single material layers. Once known, these calibration rates were used to determine a growth time for each layer given its desired thickness. The growth of the oxide barriers was performed *via* a similar method to that described in references [142, 143]. It was crucial that the resultant barriers were fully oxidised and as uniform as possible. In order to ensure this was the case all oxide barriers were grown in stages of 2 nm thickness as follows. A 2 nm thick layer of aluminium was first deposited. The resultant Al(2) layer was then exposed to an oxygen flow of 76 $sccm$ for 60 s to ensure a thorough and uniform oxidation of the whole layer. This process was repeated n times until the desired thickness of oxide had been deposited on each of the substrates. Following the deposition of the oxide barriers, and before any further growth of the constituent sample layers took place, the growth chamber vacuum was restored. This was to ensure the purity of the metallic layers, in particular the niobium, was not effected by residual oxygen in the chamber.

Characterisation measurements were carried out, prior to the muon beamtime, using both the low temperature transport system and the SQUID magnetometer as described in sections 2.2 and 2.3 respectively. The samples were grown using the 99.999% high purity niobium target and so the superconducting transition temperatures were expected to be similar to those displayed in the left panel of figure 3.3. Indeed all of the T_c values sat within the range $(7.6 - 8.7)\ K$, with the lower extreme being the trilayer and the upper the single niobium control layer, and had typical transition widths of $(0.05 - 0.1)\ K$. Additionally, upper critical field measurements were performed and fitted, as described previously in section 3.3, and the value of ξ_s determined to be $(11.5 \pm 0.3)\ nm$ as before for the same quality niobium target measured in chapter 3. Further characterisation was performed to determine the uniformity of the cobalt layer between samples. This was of particular importance since the aims of the study involve making a comparison across a set of different structures where only the oxide barrier is supposed to change. Should the magnetisation alter significantly across the samples, for example, this would need to be accounted for explicitly in the muon data modelling. Moreover, cobalt oxide is a known antiferromagnet (see for example [100–103]). Since it was possible a thin layer of the cobalt may oxidise during the deposition of the AlO_x barrier it was important to determine whether or not there was any signature of antiferromagnetism in the samples.

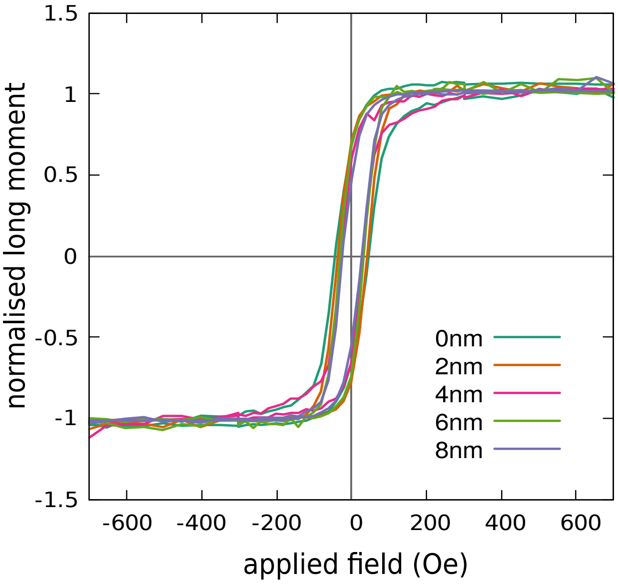

Figure 5.1: Normalised moment as a function of in-plane applied field, measured using the SQUID magnetometer, for each barrier thickness in the NSIF sample set. In each case the data has been normalised to the corresponding saturisation magnetisation (m_S) values displayed in table 5.1.

Table 5.1: Area and saturation magnetisation values for the NSIF samples

$d_I (nm)$	0	2	4	6	8
$area (mm^2)$	4.4	5.8	6.25	4.0	7.8
m_s (μemu)	19	20	21	17	27
$m_s/area$ ($\mu emu/mm^2$)	4.3	3.5	3.4	4.2	3.5

Figure 5.1 presents the results of the SQUID measurements on each of the NSIF samples. The plot shows the normalised moment measured on the longitudinal coils as a function of the in-plane applied measurement field. For ease of comparison the y-axis has been normalised to the corresponding saturation magnetisation values (m_s) displayed in table 5.1. All of the MH loops are of a uniform shape and centred around zero as expected. Additionally, one can note that at the standard muon measurement field of 300 Oe all samples have reached, or are close to reaching, saturation. The absolute values of saturation magnetisation (m_s) appear to vary across samples though not in a systematic way. When one divides these values by the sample area, which as seen in table 5.1 was not held constant, there is a variation of ≈ 30 % from the average value. Though this is not systematic with the oxide thickness it is important to keep this in mind when interpreting the results of the LEμSR measurements.

5.1.2 Transmission electron microscopy and elemental analysis

The work presented within this subsection was carried out with the aid of Dr David Miller from the electron microscopy lab in the School of Chemistry at the University of St Andrews. These measurements have been immeasurably useful in providing the means to both characterise the oxide barriers and determine layer thicknesses for use within muon data modelling. This section is organised into two parts. Within the first some example transmission electron microscopy results are presented. These measurements are then supplemented by the results of x-ray absorption analysis presented within the second part [144, 145].

Part I: Transmission electron microscopy

In order to perform the desired transmission electron microscopy (TEM) measurements a cross section of each sample first had to be milled out of its respective substrate. This was achieved through the use of the FEI Scios dualbeam set-up in the electron microscopy suite in the School of Chemistry. This system combines a high resolution scanning electron microscope (SEM) for imaging with a gallium focused ion beam (FIB) for milling the sample. By tuning the FIB current within the pico- to nano-amp range, it is possible to either mill away material rapidly (high current) or to carefully microstructure the sample (low current). The apparatus is also equipped with a gas injection system that allows the deposition of both platinum and carbon. These materials can be used to both protect the sample during milling and to provide additional contrast for the imaging process. Through application of the SEM and FIB subsystems concurrently it is possible to prepare a clean cross section and image sub-surface features or even fabricate nanostructures.

The aim for this study was simply to extract and polish a thin cross section of the sample for TEM measurements such that the quality and composition of the layers could be determined. The process through which this was achieved is illustrated in figure 5.2.

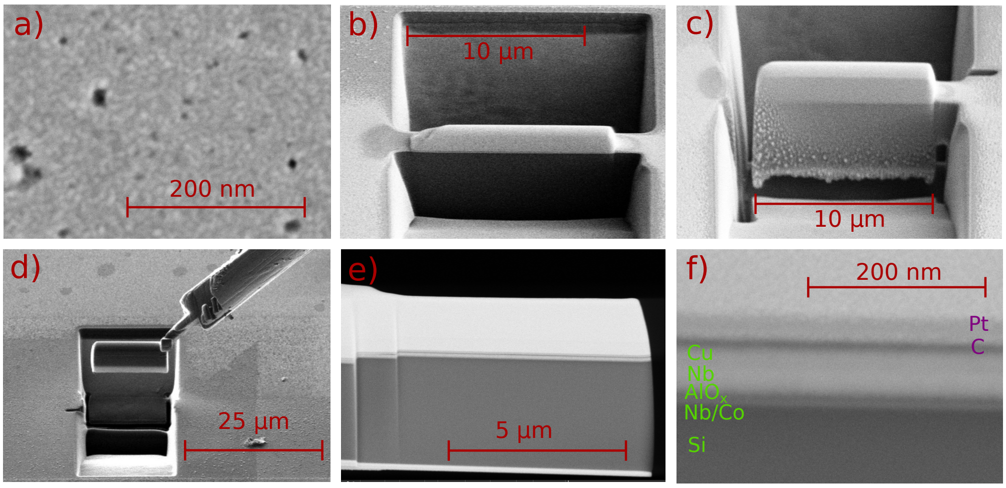

Figure 5.2: SEM images of the cross section preparation process. a) The copper surface of the sample onto which the protective layers of carbon (for contrast) and platinum were deposited. b)-e) The ion milling process. b) Deep wells were cut into the sample to mill out a thin bar which could then be cut out from the substrate as seen in c). d) The resultant thick cross section was detached and fixed to a TEM sample stage. e) Part way through the thinning process and f) An TEM image of the cross section taken part way through the thinning process. The sample layers are indicated in green and the protective caps in purple.

The sample was first loaded into the system and the SEM used to identify a suitable region of the sample to be extracted. Figure 5.2a) shows a representative region of the sample surface. The dark patches are pits in the surface of the copper layer that formed during the sputter growth. Prior to any milling taking place both a thin layer of carbon and a thick bar of platinum were deposited onto the sample. The carbon was used to provide good image contrast and the thick platinum bar was essential to protect the sample cross section during the ion milling process. In order to extract a sample cross section the FIB was used to mill away trenches of material either side of the platinum bar, as shown in figure 5.2b), before the whole slice could be cut out and detached from the substrate as illustrated shown in panels c) and d) respectively. Once detached the slice was transported and fixed to a TEM stage for thinning and polishing. Figure 5.2e) shows the sample part way through the thinning process. The staggered nature of the cuts into the slice were to prevent bending and ensure stability of the final sample. A sample TEM image of the cross section, taken during the thinning process, is shown in figure 5.2f). The sample and coating layers are clearly visible and labelled in green and purple respectively.

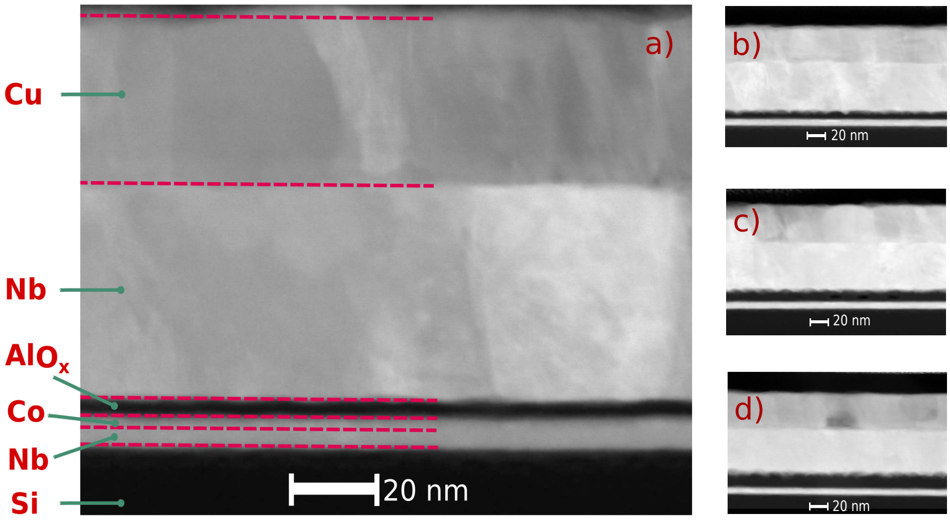

Figure 5.3: TEM images showing the Cu/Nb/AlO$_x$(d_I)/Co samples where a) $d_I = 2\ nm$, b) $d_I = 4\ nm$, c) $d_I = 6\ nm$ and d) $d_I = 8\ nm$. Light and dark areas correspond to conducting and insulating regions respectively.

Once the milling process was completed the final thickness of the cross section was around 100 *nm* and no further imaging using the SEM could take place. This was to prevent the polished surface from becoming damaged. Whilst the SEM image in figure 5.2 already shows all of the material layers, a more detailed understanding of the structure and conducting behaviour of the sample can be gleaned from the TEM measurements presented in figure 5.3. These images were measured using the Jeol JEM-2011 transmission electron microscope within the school of Chemistry's electron microscopy suite. The light and dark areas of the images correspond to conducting and insulating regions respectively. The panels a) through d) of figure 5.3 correspond to images of the Cu/Nb/AlO$_x$(d_I)/Co samples where a) $d_I = 2$ *nm*, b) $d_I = 4$ *nm*, c) $d_I = 6$ *nm* and d) $d_I = 8$ *nm*. From these images it can be concluded the AlO$_x$ barriers are uniformly deposited and oxidised throughout though some roughness does develop at the Nb/AlO$_x$ interface for thicker barrier layers. Additionally, these images allow an accurate determination of the layer thicknesses of Nb and Cu for use within the muon data modelling. For example from figure 5.3a) the thickness values for the $d_I = 2$ *nm* NSIF sample were determined to be (38 ± 2) *nm* and (51 ± 2) *nm* for the copper and niobium layers respectively.

Part 2: Elemental analysis results

The Jeol JEM-2011 transmission electron microscope used to measure the TEM images presented in figure 5.3 is also equipped with an x-ray detector for EDX analysis of the sample composition. The excitation electrons are emitted from a lanthanum hexaboride source and are incident on the TEM cross section. The absorbed electrons excite characteristic transitions within the sample emitting x-rays which are subsequently detected by an Oxford ISIS EDX system. By scanning across the sample surface and detecting a portion of the x-ray emission, a map of the elements present within the sample can be built up and their relative compositions estimated as a function of position. Both of these measurement procedures were carried out on all of the Cu/Nb/AlO$_x$(d_I)/Co samples within the NSIF set. The aim of these measurements was to gain a rough idea of the purity of each of the layers, in particular the quality of the niobium, and to estimate the composition of the oxide barrier. Figure 5.4 shows representative data for the a) $d_I = 4$ *nm* and b) $d_I = 8$ *nm* samples.

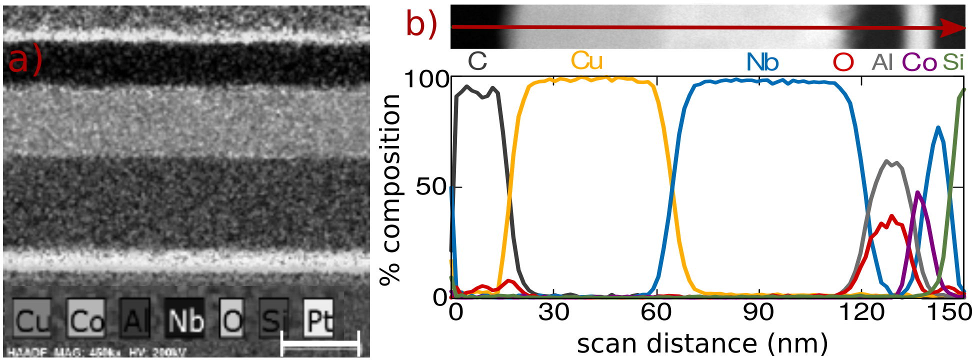

Figure 5.4: Example composition analysis of the Cu/Nb/AlO$_x$(d_I))/Co samples where a) displays the composition map for $d_I = 4$ nm with the scale bar corresponding to 15 nm and b) the line cut % composition analysis for $d_I = 8$ nm. The bar at the top of panel b) shows the line scan corresponding to the extracted % composition. The arrow indicates the scan direction.

Figure 5.4a) displays the resultant composition map of the cross section for the Cu/Nb/AlO$_x$(4 nm)/Co sample. In this case the scale bar corresponds to a distance of 15 nm. The key at the bottom indicates which layer largely corresponds to which sample element. The contrasting carbon cap is not included within the key but is visible as the dark capping layer on top of the copper feature. All of the sample layers are clearly distinct from one another. There is a visible oxygen background across the entire sample with a particularly strong presence at both the surface of the copper and throughout the niobium. This is not surprising since the copper surface had been exposed to air for some time and niobium is notoriously quick to bind to oxygen. At first glance the aluminium oxide barrier appears to be uniformly oxidised as was indicated by the direct TEM image presented within figure 5.3b) for the $d_I = 4$ nm sample.

In order to gain more information of the composition of the sample as a function of the position a simple line scan was performed from the top of the cross section down to the silicon substrate. This process was carried out for each sample in the set and a representative result for the $d_I = 8$ nm sample presented within figure 5.4. The top panel of figure 5.4b) indicates the position and direction of this line scan. All along this line scan an elemental analysis was performed and the corresponding percentage mass composition estimated from the resultant data. The plot of the percentage composition as a function of position along the line scan is presented in the bottom panel of figure 5.4b). From the compositional analysis it is clear the thick Cu(40) and Nb(50) layers are close to 100% pure across most of their bulk but with a small background of oxygen dispersed throughout. This likely formed during the original growth. The suspected CuO cap, which will have formed over time through exposure to air, is visible within the percentage composition data as indicated by the oxygen peak at a scan position around 20 nm. Examination of the thinner layers: the $\mathrm{AlO}_x(8)$; the Co(2.4) and Nb(3), shows significant spreading of material between adjacent layer depositions. The interface regions are extended and significant mixing of the materials is evident. This is also visible within the line scan image in the top panel of figure 5.4b) where there is evidence of roughness around the $\mathrm{Nb}/\mathrm{AlO}_x$ interface. Part of this apparent spreading of material around the thinner layers could be related to instrument resolution which was around 0.5 nm. From the percentage mass composition of the oxide barrier at its centre, indicated by the peak positions of Al and Co, the composition ratio was estimated to be Al(2):O(2.2) meaning the aluminium is not quite fully oxidised.

The results of the low temperature transport, SQUID and electron microscopy measurements demonstrate that, whilst the interface regions are quite protracted, the overall sample quality is good. The superconducting transition temperatures, coherence lengths and magnetic characteristics are all comparable to the samples from set II measured in chapter 3. The ferromagnetic layer appeared to behave consistently across samples though there was a significant, but not systematic with oxide thickness, variation in m_s/area. This is important given the EM effect depends critically on the magnetisation of the ferromagnet and should be taken into account when interpreting the muon results. The TEM and elemental analysis measurements demonstrate that the oxide barriers are in general uniformly deposited and oxidised throughout but that there is some roughness at the S/I interface region. This is present in all samples, however, and so should not effect the comparison of behaviours across the different sample structures.

5.2 LEμSR measurements as a function of the oxide barrier thickness

As in previous chapters the low energy muon measurements were carried out on the LEM beamline at the Paul Scherrer Institut. Unless otherwise stated the experiments were set up and the data analysis methods applied as discussed in section 2.1 of chapter 2. For this study, systematic measurements of the flux profile across each of the samples were made in the hope of tracking both the direct and electromagnetic proximity effects as a function of the coupling between the superconductor and the ferromagnet. This present section is divided into three parts. Firstly, following on from the results presented in chapter 4, a new way of modelling the flux profiles is formulated such that the pair breaking, and consequently the direct proximity, can be accounted for. This new method is then applied to the data in the second subsection and quantitative measures of the pair breaking and EM proximity effects extracted. Finally, within the final subsection, the effects of stray fields generated at the SIF interface are discussed and ruled out as the cause of the experimental observations.

5.2.1 Accounting for the effects of pair breaking

In light of the results discussed in chapter 4, where there appeared to be a measurable effect of pair breaking near the S/F interface, and given that the present study involves a systematic comparison of the muon signal as a function of S-F coupling strength, a new method for modelling the flux profiles is needed. Details of the new approach are given within this subsection and later applied to model the LEμSR data as discussed in section 5.2.2.

As has already been discussed, the expected screening profile across a thin film superconductor with vacuum interfaces follows directly from the London theory and is given by the form shown in equation 3.4. It was demonstrated in chapter 3 that this profile describes the sputtered niobium control samples very successfully, allowing the determination of the corresponding λ_L values for each different sample purity. Following the results of the quasiclassical calculations presented in figure 3.8 it became clear that extension to the NS bilayer case could be approximated simply by replacing d_s with d_{NS} in the London equation. This is possible since for the particular combination of sample material parameters present in the measured systems the copper layer becomes fully proximitised and screening develops near symmetrically across the full spatial extent of the bilayer. Further to this extension in chapter 4, in light of the development of the new electromagnetic proximity theory, an additional term was added to equation 3.4 to model those systems where a ferromagnet was in direct contact with the superconducting layer. This additional term, taking the form of an amplitude at the S/F interface which decays away exponentially over λ_L, was included to account for the electromagnetic proximity effect at the S/F interface as shown in equation 4.3. The results of imposing the relevant model profiles on the bilayer and trilayer samples presented within chapter 4 demonstrated that the new theory was capable of successfully and consistently describing the experimental observations.

The inclusion of the ferromagnetic layer to the underside of the superconductor ought to have a further consequence on the flux profile. In addition to the EM proximity effect, the direct proximity between the superconductor and ferromagnet will result in the suppression of the superconducting condensate within the region close to the S/F interface due to pair breaking effects. The result is a depletion of superconducting pairs near the interface and a corresponding reduction in the Meissner screening amplitude. As can be seen from the quasiclassical calculations in figure 3.8, this occurs asymmetrically with the loss of amplitude biased towards the region near the ferromagnet. The net impact of this being a shift of the now less pronounced minimum towards the normal metal layer. Some evidence of this effect was observed in chapter 4 and is presented in figure 4.3. By allowing the amplitude of the EM proximity effect, A_{EM}, to vary as a function of the average muon probing depth a loss of amplitude was observed for those energies which sampled around the S/F interface. Seeing as the pair breaking effects should occur within about a coherence length (ξ_s) of the interface it seems the likely cause. In the present study, a systematic decoupling of the ferromagnetic exchange field from the superconducting condensate will result in these pair breaking effects no longer being constant across the different samples. In order to make a successful comparison of EM proximity as a function of coupling strength therefore it is key these direct proximity effects are also accounted for.

In order to capture the effect of direct proximity on the flux profile the following assumption is made. Since the asymmetric depletion of amplitude occurs over too spatially narrow a region to observe directly it is modelled as a reduction in amplitude of the Meissner term which itself remains symmetric. The reduction in the standard Meissner response, to one which is now labelled B^*_{NS}, is accounted for within the model through the use of an effective penetration depth, λ_{eff}, that will be longer than that of the bilayer. The resultant profile used to model the NSIF samples within this chapter is therefore given by the form presented in equation 5.1.

$$B_{NSIF}(x) = B^*_{NS} + A_{EM} \exp{(x - d_{NS})/\lambda_{eff}} \tag{5.1}$$

Where A_{EM} is the strength of the electromagnetic proximity which now decays over the effective penetration depth λ_{eff}. As before there are two terms. The first describes the standard Meissner screening, with the effects of pair breaking parameterised a simple reduction in the symmetric amplitude, and the second term is the EM proximity contribution.

A schematic of the field profile given by equation 5.1 is shown in figure 5.5. The various plotted profiles have been scaled to the external field typically used for the measurements. In the normal state the expected flux density is constant at the applied measurement field. This is indicated by B_0. In the superconducting state the full flux profile, B_{NSIF}, is composed of two constituent components: The normal Meissner term (B^*_{NS}) and the EM component (shaded region). The effect of pair breaking is parameterised by the direct proximity amplitude, A_{SF}, which is simply the difference between the bilayer response (B_{NS}) and B^*_{NS} at the screening minimum. The second parameter of interest is of course A_{EM} which is the EM amplitude.

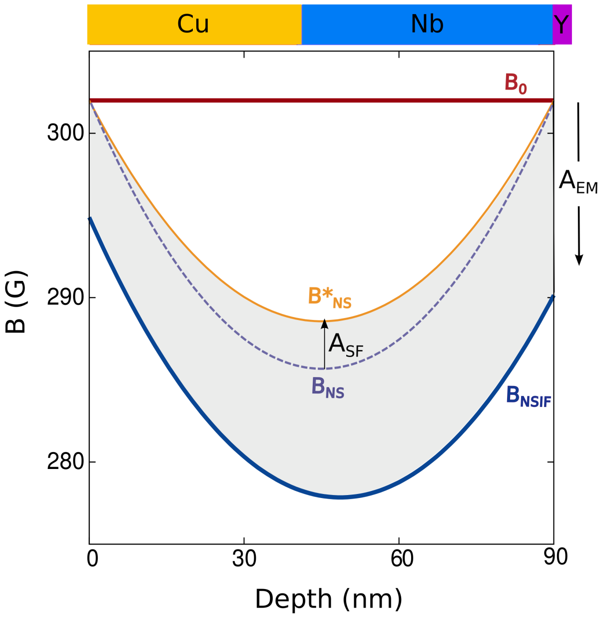

Figure 5.5: A schematic of the full model screening profile, B_{NSF}, decomposed into its Meissner (dashed line) and EM (shaded region) contributions but including the effects of pair breaking at the S/F interface. The profile has been scaled to the applied measurement field.

In order to model the NSIF sample series the form of equation 5.1 is imposed on the measurement data. Both λ_{eff} and A_{EM} are treated as free fit parameters such that the resultant profile best predicts the extracted flux averages. Within this model there is now an additional fit parameter when compared with the treatment applied in chapter 4. It is important to note that in treating the data this way the fit is not expected to be improved simply because of an additional fit parameter but rather because the underlying physics is now being directly accounted for. In doing so a quantitative measure of two different but related proximity effects can be extracted in the form of the two amplitudes A_{EM} and A_{SF}.

5.2.2 Extracting the SF and EM proximity amplitudes as a function of barrier thickness

As described within the previous section, the form of equations 3.4 and 5.1 are imposed on the relevant muon data such that they best predict the measured flux averages. In the case of the NS bilayer sample, the simple London profile is used to model the data with the only fit parameter being the λ_L value. Once the bilayer profile is known this acts as a control for the NSIF samples and defines an upper limit for the expected standard Meissner component of the total flux profile. It also provides a baseline with which to compare the results of modelling the NSIF data. The full form in equation 5.1 is imposed on all samples containing a ferromagnetic layer. As discussed at the end of section 5.2.1, for these samples there are two free fit parameters used to describe the data: λ_{eff} and A_{EM}, which correspond to the Meissner and EM components respectively. By modelling the muon data associated with each oxide barrier thickness, and determining the corresponding values of A_{EM} and A_{SF} where the latter is found through comparison to the bilayer response, the effects of both pair breaking and EM proximity can be tracked as a function of the S-F coupling strength. The results of carrying out this analysis are presented within this section. Firstly, some representative data are shown alongside the resultant best fit profiles for a subset of the measured samples. This is included simply to better illustrate the data analysis procedure. The second part of the section then focuses on the barrier thickness dependence of the two proximity amplitudes. It is found that the EM amplitude significantly outweighs the effects of pair breaking until for thicker barriers the bilayer result is recovered.

Figure 5.6 presents some example results of imposing the flux profiles on the LEμSR data. The data shown correspond to a set of samples of the form Cu(40)/Nb(50)/Y where Y = Si, Co(2.4)/Nb(3)/Si and Al_2O_x(2)/Co(2.4)/ Nb(3)/Si for the NS, NSF and NSIF samples respectively. As in previous chapters the top panel presents some sample muon stopping profiles. In each case the corresponding vertical line indicates the average stopping position for muons of that energy within the sample structure shown. At the lowest measured energy the muons stop only within the Cu layer. As the probing energy is increased the stopping profiles start to spread out and shift to higher average probing depths whilst a tail remains in the Cu. For $E_\mu \geq 20\ keV$ the muons begin to sample the "Y" layers of each structure.

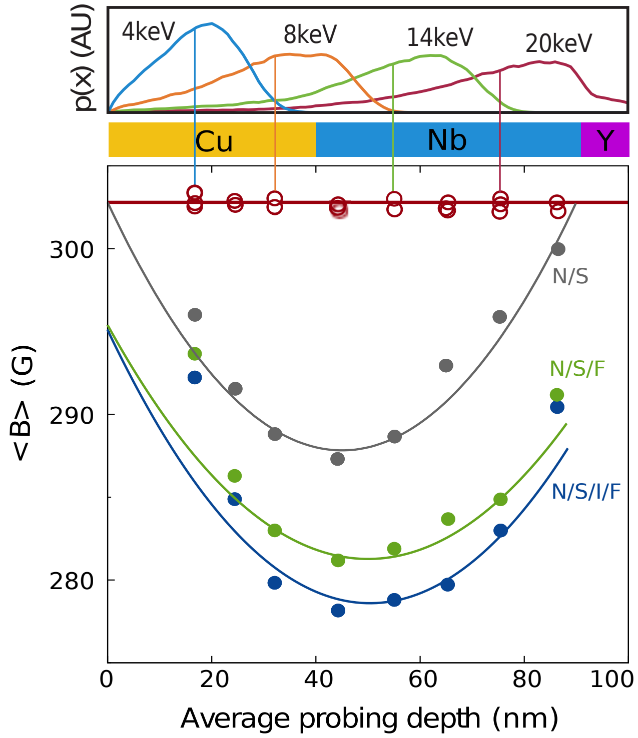

Figure 5.6: The effect of an oxide barrier on the LEμSR results. Top panel: sample muon stopping profiles for a range of incident muon energies. The vertical lines in each case indicate the average probing depth with the profiles for $E_\mu \geq 20\ keV$ beginning to extend into the Y layers. Bottom panel: representative results of the LEμSR results performed on the NSIF sample structures in an applied field of 302.4 Oe. The solid lines represent the results of imposing the spatial flux profile on each NSY structure where Y = Si, Co(2.4)/Nb(3)/Si and Al_2O_x(2)/Co(2.4)/ Nb(3)/Si for the NS, NSF and NSIF samples respectively. The average field values are plotted as open (closed) circles for the normal (superconducting) state data which were measured at 10 K (2.5 K).

The results of imposing the underlying field profiles, given by equations 3.4 and 5.1 for the bilayer and NS(I)F samples respectively, are indicated by the labelled solid lines in the bottom panel of figure 5.6. The results of the conventional averages approach are also included for comparison and are indicated by the open and closed circles for the normal and superconducting state measurements respectively. All normal state measurements were conducted at a temperature of 10 K and the corresponding superconducting state data taken at 2.5 K. For each data point the corresponding error in the average field, typically found to be within the range $(0.1-0.3)$ G, is also plotted but is too small to be visible on the scale of the symbol size in this case. In the normal state, for all measured samples, a constant flux density is observed which simply corresponds to the applied measurement field of 302.4 Oe. From the superconducting state measurements it is clear that in all samples, across all probing energies, a flux lowering is observed. As has been previously observed and modelled within chapter 4, the NS data show the standard Meissner screening response extending across the full spatial extent of the proximitised bilayer. The best-fit cosh profile in this case corresponds to a penetration depth of $\lambda_L = 140$ nm. Also modelled within the previous chapter is the NSF trilayer result which shows a significant increase when compared with the bilayer due to the EM proximity effect. Here the best fit profile corresponds to fit parameter values of $\lambda_{eff} = (156 \pm 1.5)$ nm and $A_{EM} = (-13 \pm 0.7)$ G. The NSIF data show an overall enhancement to the flux lowering. When one considers the shape of the average data it is clear this is due to a partial recovery in the normal Meissner screening, thanks to the partial decoupling between S and F, and that the EM component remains relatively constant. This is reflected in the results of the profile modelling where the best-fit result for NSIF corresponds to fit parameter values of $\lambda_{eff} = (151 \pm 1.1)$ nm and $A_{EM} = (-14 \pm 0.5)$ G. The effective penetration depth has started to recover and move back towards the bilayer result whilst the two EM amplitudes are within error. This naively suggests that the degree of coupling between the superconductor and ferromagnet has been altered sufficiently to affect the pair breaking but not the electromagnetic proximity.

When one compares the results of the conventional averages approach with the best-fit profiles found from imposing the expected full spatial dependence a good correspondence between the two is observed across most energies. As was discussed previously within section 4.3.2, the model profiles for the NSF and NSIF samples begin to deviate from the averages at the lowest probing energy. This is most likely due to the EM component rolling off more rapidly than expected within these systems where the thickness is less than the penetration depth. In order to confirm this further measurements on thicker samples would be required. It is clear from these example data sets that the averages approach to the data analysis captures the physics of the system well, and given the right framework for interpretation, provides a good physical understanding of the system. The full spatial analysis, however, offers the opportunity to identify and extract a quantitative measure of each proximity effect and to track, given measurements and analysis across the full sample set, their behaviour as a function of the coupling strength as was the aim of this study. The same analysis as presented in figure 5.6 for the Cu(40)/Nb(50)/Al$_2$O$_x$(2)/Co(2.4)/ Nb(3)/Si sample was therefore performed on the muon data for all other oxide thicknesses and the corresponding best fit values of A_{SF} and A_{EM} extracted for each. The results of this analysis are shown in figure 5.7 where both proximity amplitudes are plotted as a function of the insulator thickness, d_I, which is used as some measure of the coupling strength.

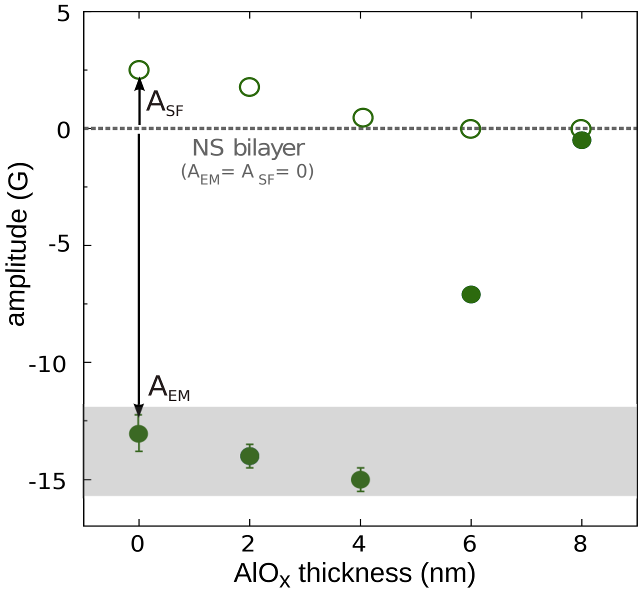

Figure 5.7: The extracted proximity amplitudes as a function of d_I which corresponds to a changing S-F coupling strength. The open (closed) symbols correspond to the extracted A_{SF} (A_{EM}) values. The NS bilayer control, for which both amplitudes are zero, is represented by the dashed line. The light shaded region indicates the approximately constant A_{EM} for $d_I \leq 4\ nm$.

The open and closed symbols correspond the the extracted values of A_{SF} and A_{EM} respectively. The plotted error bars take account of both the error associated with the data fitting and any variation between samples in $T_c - T_s$; where T_s was the sample measurement temperature. This was achieved using the known temperature dependence of the total amplitude for these sample structures as presented in appendix D. The horizontal dashed line represents the NS bilayer control result for which both A_{EM} and A_{SF} are of course zero. When the niobium and cobalt are in direct contact, for $d_I = 0\ nm$, there is both a small reduction of about 15% in the standard Meissner screening response, which can be determined from the corresponding A_{SF} value, and a substantial diamagnetic enhancement (A_{EM}) due to the EM proximity. As the degree of coupling between the Nb and Co layers is reduced, through the insertion of the insulating oxide barriers, the direct proximity weakens and the suppression in the standard Meissner screening reduces until for $d_I \geq 4$ nm $A_{SF} = 0$ G and the NS bilayer result is recovered. The behaviour of the EM proximity appears to be rather different. The value of A_{EM} appears to be approximately constant for barrier thicknesses of $d_I \leq 4$ nm. This is indicated by the shaded band shown in figure 5.7. A further increase in the thickness of the $\mathrm{Al_2O}_x$ layer causes the value of A_{EM} to diminish back towards the bilayer control response.

Through careful modelling of the LEμSR data gathered for the full range of NSIF sample structures, the dependence of both the direct and electromagnetic proximity amplitudes on the insulating barrier thickness has been successfully extracted. Since both amplitudes return to the NS bilayer response as the barrier thickness is increased it seems the effects observed are due to the direct sampling of the ferromagnet by the condensate and are not related to any stray magnetic fields. In particular, as has already been seen in previous chapters the stray fields generated at the S/F interface effect the muon depolarisation rate strongly over lengthscales closer to 15 nm whereas here both proximity contributions have disappeared for $d_I = 8$ nm. Through modelling of the muon depolarisation rate as a function of d_I any potential influence of stray fields can be explored in more detail. This is the subject of the following subsection where it is explicitly demonstrated that stray fields play little or no role in the observed physics.

5.2.3 Ruling out the effect of stray fields

It has been discussed in previous chapters that in the absence of ferromagnetism the nuclear moments are the main source of magnetic inhomogeneity in these systems. This leads to a constant nuclear depolarisation rate, λ, within each material layer. On the other hand, for any system in which a ferromagnetic layer is present the spatial dependence of λ becomes dominated by the effect of the stray field originating at the S/F interface. In these cases, an approximately exponential decay profile for λ which is maximal at the surface of the ferromagnet and decays away over typical lengthscales of up to 20 nm is found to describe the data very successfully. It is therefore possible, through a careful analysis of the data, to model λ as a function of d_I and compare the depolarisation amplitudes, λ_0, and decay lengthscales, ξ_λ, across the different samples to see how random fluctuations in the local field vary. This is achieved through imposing the profile given by equation 2.8 on all the measured data and the results are presented in figure 5.8.

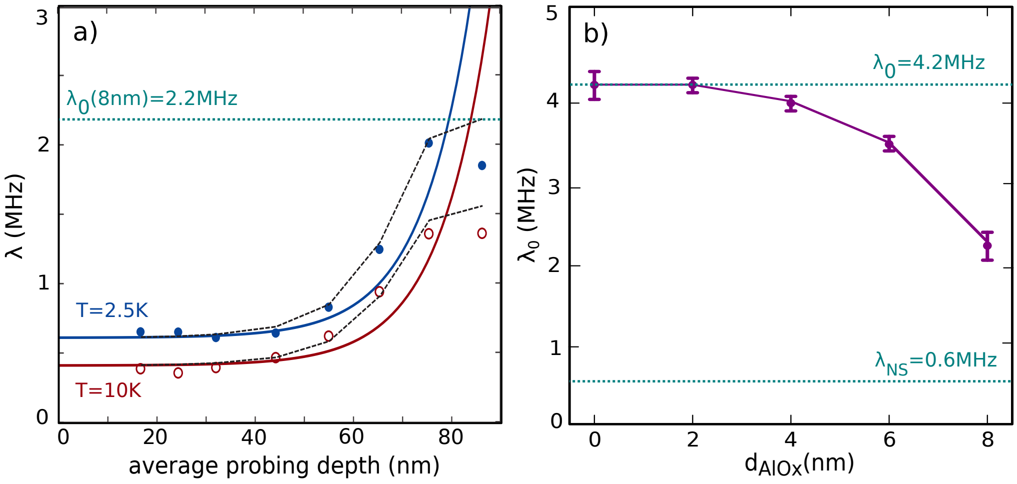

Figure 5.8: Results of modelling the depolarisation rate at the interface as a function of oxide thickness. a) depolarisation rate as a function of the average probing depth for the $d_I = 8\ nm$ sample. The solid lines show the best fit model profiles and the open (closed) symbols show the corresponding averages measured at T= 10 K (T= 2.5 K) in the normal (superconducting) state. The black dotted lines show the result of "predicting" the averages from the full spatial profile. The horizontal dashed line indicates the position at which the amplitude, λ_0, was extracted. b) the plotted points show the depolarisation amplitude (λ_0) as a function of the oxide barrier thickness (d_I). The solid line is a guide to the eye and the dashed lines represent the maximum depolarisation amplitude which corresponds to the $d_I = 0\ nm$ sample and the NS control value for reference.

Figure 5.8a) presents the results of modelling the depolarisation rate data for the Cu(40)/Nb(50)/Al_2O_x(8)/Co(2.4) sample. The quality of the data and the imposed fit profile are representative of all the measured samples within the set. The solid lines correspond to the best fit form of equation 2.8 and the open and closed symbols correspond to the results of the averages analysis for the 10 K normal state and 2.5 K superconducting state measurements respectively. As would be expected there is an enhanced depolarisation rate below the superconducting T_c due to increased flux gradients associated with screening. The black dashed lines represent the result of calculating the spatial averages directly from the optimised profile as described in section 2.1.7. There is an excellent correspondence between the measured average flux values and those determined from the best fit profile for the data taken both above and below T_c which validates the practical use of this phenomenological model. The horizontal dashed line indicates the definition of λ_0, the depolarisation amplitude at the SI interface, which for this sample was found to be 2.2 MHz. The same analysis was carried out for all other barrier thicknesses and the value of λ_0 extracted for each. The resultant plot of the depolarisation amplitudes as a function of the barrier thickness is shown in figure 5.8b) where the connecting line is just a guide to the eye. The dotted lines represent the maximum observed value, which corresponds to both the $d_I = 0$ nm and $d_I = 2$ nm samples, and the NS bilayer result which is significantly lower than even the result for the $d_I = 8$ nm sample. Any increase in the barrier thickness from $d_I = 2$ nm results in a slight drop off of the value of λ_0 but at no point does it come close to approaching the bilayer value of ≈ 0.6 MHz in the superconducting state. In addition, for all samples the decay lengthscale, ξ_λ, of the depolarisation amplitude was found to be within the range $\xi_\lambda = (12 \pm 1)$ nm. When taken together this suggests the observed flux lowering attributed to EM proximity is not due to a stray field effect. Whilst there is some variation in λ_0 it does not correlate to the behaviour of the extracted values of A_{EM} which settle back to the bilayer response for $d_I = 8$ nm, a lengthscale over which the stray fields still significantly effect the depolarisation.

5.3 Discussion of the S-F coupling dependence of EM proximity.

The modelling of the full spatial dependence of the LEμSR data is consistent with there being an additional source of vector potential at the SIF interface which in turn generates an additional component to the orbital screening. These observations are in line with current thinking regarding the expected electromagnetic proximity effects that ought to take place wherever a ferromagnet comes into contact with a superconductor. Indeed the experimental observations that: the additional response requires the presence of the ferromagnet; depends unambiguously on the direct sampling of F by the superconducting condensate and has its spatial origins at the SIF interface, are direct predictions of the theory. The measurements themselves provide excellent evidence against stray fields being related to the measured effect since for thick oxide barriers $A_{EM} \rightarrow 0$ and the bilayer result is recovered whilst the stray fields are still significantly higher than the bilayer case. Furthermore, the modelling of the muon depolarisation rate has shown that the stray fields decay over a longer lengthscale than the barrier thickness required to quench the observed additional screening component. It is also important to note that the observed dependence of A_{EM} on the oxide thickness is not systematic with the observed variations in m_s/area displayed in table 5.1 so cannot simply be due to variations in the magnetisation of the F layer. For thinner oxide barriers, $\mathrm{d_I} \leq 4$ nm, a constant value of A_{EM} was observed. The origin of this is currently unknown and is not explicitly explored within the existing theory. Naively A_{EM} ought to depend on both the superconducting gap and on the contact term between the superconductivity and ferromagnetism. The latter gradually reduces as the thickness of the insulating barrier increases and the former correspondingly strengthens due to a diminished effect of pair breaking. The interplay of these two effects is not currently explored within the theory and it is possible the result may be an approximately constant value of A_{EM} though this remains an open question. The observation does, however, suggest the possibility to design a device in which the electromagnetic component can be maximised whilst minimising the effects of pair breaking.

The experimentally determined behaviour of the direct proximity, parameterised through A_{SF}, as a function of the coupling strength makes intuitive sense. The 15% reduction in the standard Meissner screening response observed in the absence of an insulating barrier, and the steady loss of this amplitude as the S-F coupling is reduced such that for $d_I \geq 4$ nm the bilayer Meissner screening was recovered, was clearly anticipated. The novel piece of understanding to come out of this observation is really that, given appropriate control samples, a full spatial analysis of the kind carried out here provides access to quantitative measures of how the proximity effects develop within these systems. Additionally, the relative strengths of the pair breaking and the EM proximity suggests the importance of accounting for these electromagnetic effects in both the interpretation of experimental results and in the design of new S/F devices. Indeed as discussed within chapter 4 this new model provides a framework in which to interpret a number of previously published anomalous results within the field [39, 60, 82, 85].

It is important to note that whilst the suggested supply of additional vector potential is the local magnetisation of the ferromagnet this has not been unambiguously determined through these measurements. The asymmetric spatial profile of the additional screening, which originates from the SIF interface region and disappears once the ferromagnet becomes isolated, is highly consistent with the theoretical predictions. It is perfectly possible, however, that there are additional contributions to the vector potential as discussed within section 4.4. It is likely that further theoretical developments will steer new experimental efforts to identify and disentangle possible contributions.

5.4 Conclusions on the use of oxide barriers to manipulate EM proximity

Within the present chapter, the influence of inserting insulating oxide barriers between superconducting and ferromagnetic layers on the direct and electromagnetic proximity effects has been studied. A full set of samples of the form NSI(d_I)F were measured using LEμSR and the data analysed within a model consistent both with pair breaking effects and the new EM proximity theory. A non monotonic dependence of the total flux expulsion as a function of the barrier thickness was observed. This could be decomposed into two distinct and opposing contributions: the first, parameterised by A_{SF}, arising from the anticipated pair breaking of the ferromagnetic exchange field, and the second the EM proximity effect. The latter being of strength A_{EM} was, for the combination of material parameters present within these sample systems, persistently diamagnetic and substantially larger than the corresponding effect of pair breaking. Both of these observed contributions were ultimately suppressed, and the bilayer response recovered, through insertion of a thick insulating oxide barrier at the S/F interface. This strongly suggests stray fields are not substantially contributing to the physics. For all of the measured samples the imposed model was an excellent description of the spatial dependence and magnitude of the observed flux lowering. The use of an effective lambda (λ_{eff}) and an EM proximity strength (A_{EM}) provided the means to extract a quantitative measure of both proximity effects without the need to model explicitly the full quasiclassical profiles. This type of systematic analysis could prove to be invaluable in the study of more complex devices which seek to exploit these proximity effects.

Whilst in general an excellent correspondence between theory and experiment was found there do remain some open questions. In particular, there are two points arising from this work which require further experimental and theoretical investigation to address. Firstly, the approximately constant value of A_{EM} for barrier thicknesses of $d_I \leq 4\ nm$ came as a surprise. The origins of this dependence are currently unknown and are not easily accessible within the existing theory. Further calculations are required to determine explicitly how a stronger gap function, resulting from the decoupling of the ferromagnetic layer from the superconductor, may effect the generation of the EM proximity amplitude. Secondly, these measurements still do not confirm for certain the source of the additional vector potential at the SIF interface. Whilst it seems likely to be the magnetisation of the ferromagnet further measurements, possibly conducted in zero applied field, are essential to test the details of the source of the large EM effect observed within these systems.

6 | Platinum within N/S/F heterostructures

The work presented in this final experimental chapter marks somewhat of a departure from the themes of the previous studies contained within this thesis. Whereas the content of chapters 3, 4 and 5 was focused on understanding new fundamental proximity effects within mesoscopic S/F hybrid thin films this chapter has been largely motivated by the interesting material properties of platinum. The work on platinum containing samples presented here can be broadly split into two parts. The first deals with the effect of inserting platinum spacer layers at both the S/F and N/S interfaces within the general Cu/Nb/Co sample structures studied previously. The second seeks to replace the copper normal metal layer with platinum to form NS and NSF bilayer and trilayer systems. These are found to behave very differently from the comparable gold and copper based systems.

Within the first section, measurements on both N/Pt(10)/S/X and N/S/Pt(2)/F systems, with X=(Si,F), N=Cu(40), S=Nb(50) and F=Co(2.4), demonstrate that even a thin layer of platinum can have a profound effect on the measured response of the sample to an applied field. By simply placing a 2 nm thick platinum spacer layer between the niobium and cobalt layers not only does the usual EM proximity contribution associated with the Co(2.4) layer get partially suppressed, or indeed cancelled out, but the temperature dependence of the signal is also greatly altered. Instead of immediately beginning to build up a diamagnetic screening response to the applied field, the sample demonstrates first a small paramagnetic uptick in the average flux before, at approximately 2 K below T_c, a bilayer-like screening response begins to develop. This is in contrast to a similar NSnF sample structure, where a Cu(2) spacer layer is used instead, as discussed in appendix G. If instead the platinum spacer layer is placed at the N/S interface then the standard normal metal proximity enhancement to the screening is largely destroyed despite clear evidence from STM measurements that there is a superconducting gap present at the sample surface. In addition, through comparison of results on NnS and NnSF sample structures, where n is a thin normal metal spacer, a reduced EM proximity amplitude appears to be present at the S/F interface within these systems. This provides further evidence that A_{EM} appears to scale with the Meissner screening current running along the S/F interface.

In the latter half of the chapter, results on systems where the normal metal has been completely replaced by platinum are presented. In both the measured bilayer and trilayer systems the normal metal - superconductor proximity effect behaves very differently. Most strikingly, in the case of the bilayer samples, it is not simply that the platinum layer does not exhibit a screening response but rather that the usual screening response of the niobium is completely absent, or more likely cancelled out by a paramagnetic feature, over a lengthscale of around 40 nm into the niobium layer. Moreover, comparable measurements on a platinum trilayer sample hint at a paramagnetic response at the Pt/Nb interface region and a diamagnetic screening within the niobium layer. Whilst the origin of these observations cannot be concluded for certain they only occur in systems containing platinum which suggests material specific physics, such as strong spin-orbit interaction or Stoner enhanced paramagnetism, may be at play.

6.1 Introduction to platinum in S/F hybrid systems

The work presented in experimental chapters 3-5 presents new and intriguing physics occurring at interfaces within mesoscopic superconducting systems. These are due, in large part, to fundamental proximity effects occurring at interfaces between materials widely utilised in more complex devices [1–3, 46, 72, 146]. Platinum is an interesting addition to these structures owing to its substantial set of unusual material properties all of which have the potential to influence any conventional and unconventional superconducting states found therein. It is interesting to pose the question of how known proximity effects: direct electronic, electromagnetic and inverse, will react to the presence of a high spin-orbit, short spin coherence length Stoner enhanced metal. Within this chapter LEμSR measurements are utilised in attempt to map out changes to the flux profile prompted by platinum.

Initial motivation for the presented work stemmed from the theory of weak and half-metallic ferromagnetism [69] as a means to generate unconventional superconducting states in S/F hybrid systems. Since within these systems the exchange field is weaker, the resultant damage to the pair amplitude is greatly reduced and the lengthscale over which induced correlations can propagate is increased [3, 46]. A number of experimental results have in fact reported the successful generation and manipulation of supercurrents over long lengthscales through these materials (for example [21, 73, 147]). Given that platinum is a Stoner enhanced metal [148, 149], meaning it has a high density of states at the Fermi level and consequently an extremely large magnetic susceptibility, one might expect that in the presence of an applied field platinum may induce phase shifts within Cooper pairs that are ordinarily associated with ferromagnetism. In such a system the exchange field would become tunable within applied field and temperature space both of which are highly accessible experimental parameters. In some ways the expected response is reminiscent of the properties of weak and half metallic ferromagnets within these systems but without the growth difficulties. There are potential downsides to platinum, however, its short spin diffusion length, for example, means it could be highly disruptive to the transmission of spin correlations generated through S/F interactions [150]. In addition, the coherence length of pairs within platinum is likely to be shorter given its shorter mean free path when compared with gold and copper [151]. This will likely effect the readiness with which proximity induced superconductivity penetrates platinum layers.

Finally and perhaps most interestingly, platinum is a heavy metal and hosts a high spin-orbit interaction. This makes it an attractive material within the conventional spintronic community where platinum is often used in conjunction with ferromagnetic and insulating thin films to generate strong Rashba fields. These are typically used as a means to manipulate spin polarised currents through various device architectures [152, 153]. The properties of platinum within superconducting spintronic devices are, however, comparatively little explored. It is intriguing to wonder how spin-orbit interactions may mesh with neighbouring superconducting layers in a hybrid system. The topic has indeed been the focus of a number of theoretical works [61, 62, 154, 155] which predict a whole host of unconventional effects somewhat akin to those predicted, and measured, within S/F systems (see for example [3]). In addition, the present focus on electromagnetic proximity within S/F hybrid systems provides a timely link between the two fields and initial experiments on mesoscopic superconductors interfaced with platinum suggest a wealth of rich physics waiting to be uncovered [156–163].

In light of the potential physics at play within platinum containing S/F thin films a number of sample systems have been designed and measured using LEμSR. These fall into two groups. The first seeks to investigate the effect of thin platinum layers on the proximity effects known to be generated at N/S and S/F interfaces within these devices. The second focuses on the proximity effects within simple thin film systems built around thick platinum layers.

6.2 Platinum at the interface

The results presented within the previous chapters have demonstrated that the observations made in simple NS and NSF thin films can be largely described using a combination of the quasiclassical and EM proximity pictures. In particular within chapter 3, the normal metal - superconductor proximity was successfully described within the quasiclassical framework where the resultant calculations were an excellent match to the measured data. The extension to include the effects of a strong ferromagnetic exchange field proved initially challenging, however, the new EM proximity theory has proven to be a natural description of the experimental results. Through modelling of the LEμSR data in a way consistent with the underlying theory it has been possible to disentangle the various contributions to the total muon signal and to go some way to determining their origins. This has only been recently possible thanks to both key theoretical developments and continued improvement of the experimental systems.

Direct and EM proximity phenomena depend crucially on the physics occurring at the N/S and S/F interfaces and on the material parameters of the elements involved. This poses the question of how the resulting contributions to the muon signal will be effected by manipulating the interface in different ways. Within chapter 5 a systematic study of how altering the coupling strength between S and F, which was controlled through the insertion of insulating oxide barriers of variable thickness, affected both the SF and EM proximity amplitudes. In this case it was possible to model the observations using the existing theory to great effect. Within this subsection the aim is instead to investigate the effect of inserting platinum spacer layers at both the N/S and S/F interfaces. Given the unusual material parameters of platinum this potentially offers the possibility to study how spin-orbit and enhanced Stoner paramagnetism may interact with both the normal-superconductor and superconductor-ferromagnet proximity effects.

6.2.1 Platinum and the normal metal proximity effect

The focus of the present section is to investigate the effect of inserting a thin platinum layer at the N/S interface on the screening response of the proximitised system. To this end, a set of two samples were grown using the same high purity niobium target as Set II from chapter 3. The sample structures, and corresponding experimental aims, were as follows:

i) A Cu(40)/Pt(10)/Nb(50)/Si system with which to investigate the effect of platinum on the normal-superconducting proximity. This structure will be labelled NnS in what follows with n representing the 10 *nm* thick platinum layer.

ii) In order to additionally study the EM proximity component a second sample of the form Cu(40)/Pt(10)/Nb(50)/Co(2.4)/Nb(3)/Si was developed and will be labelled as NnSF.

Whilst it is not possible to model the LEμSR signals using a full spatial profile, due in part to a lack of knowledge of the precise spatial contribution from the thin platinum layer[38] and because doing so could introduce a wealth of fit parameters leading to unstable results, it is possible to compare the extracted flux averages with those of the relevant control samples. In this case the samples for comparison are NS(II) and NSF(II), which were grown in the same vacuum cycle using the same niobium target purity, as studied in detail in chapter 3. Within this chapter LEμSR, low temperature transport and scanning tunnelling microscopy measurements (STM) are employed to investigate these NnS and NnSF systems such that appropriate comparison can be made to what is already known regarding the standard bilayer and trilayer structures measured previously.

---

[38] This would be very difficult to determine given that the spatial extent of the platinum layer cannot be uniquely sampled using the spatial resolution of a stopping profile ($\approx$ 20 *nm*)

The LEμSR measurements were conducted, and the associated conventional approach to the data analysis performed, according to the procedures discussed in section 2.1 of the experimental techniques chapter. In addition to the standard energy scans measured above and below T_c the temperature dependence of the muon signal at fixed probing energy was also recorded. The results of the muon measurements on both sample structures NnS and NnSF are presented within figure 6.1.

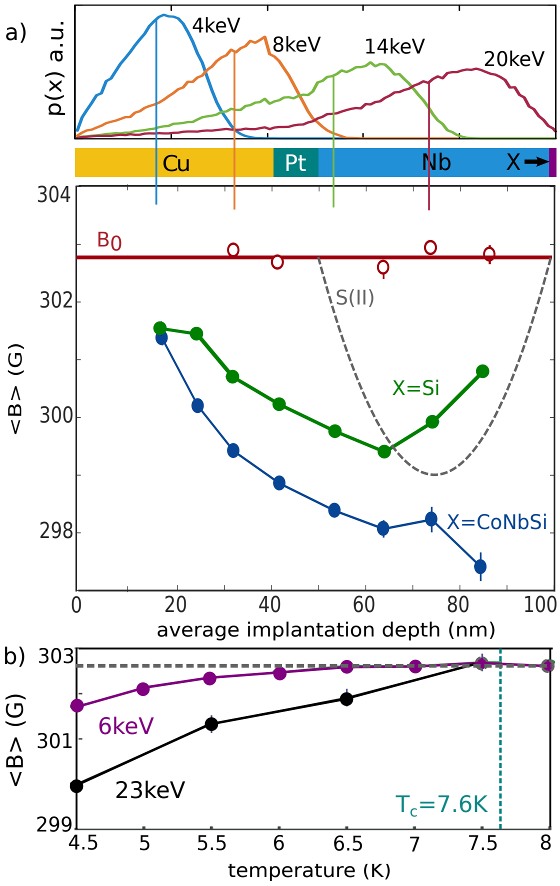

Figure 6.1: LEμSR results for the Cu(40)/Pt(10)/Nb(50)/X samples. a) The top panel displays muon stopping profiles for a few select energies. The average probing depths for each energy are indicated by the vertical lines. Plotted in the main panel are the extracted average fields as a function of the average probing depths for the X=Si and X=Co(2.4)Nb(3)Si sample structures. All normal (superconducting) data were measured at $T = 10\ K$ ($T = 2.5\ K$) and are plotted in open (closed) symbols. The lines are a guide to the eye and the grey dashed line is the best-fit profile for S(II) (the Nb(50) control). b) The temperature dependence of the average field for the X=Co(2.4)Nb(3)Si sample measured at both $E_\mu = 6\ keV$ and $E_\mu = 23\ keV$. The dashed line indicates the T_c value found from transport measurements.

Within the top panel of figure 6.1a) are shown some example muon stopping profiles where the corresponding vertical lines indicate the average probing depth for each incoming muon energy. As in the case of all previously measured copper capped samples, for $E_\mu = 4\ keV$ all muons stop within the copper layer but as the muon energy is increased the stopping distribution begins to spread out with its average shifting to higher depths. Crucially, at no point does a stopping profile sample only from the platinum spacer layer so it is not possible to gain information specifically about this spatially localised region. In the main panel of figure 6.1a) the results of analysing the LEμSR measurements using the averages approach are plotted. The data points represent the extracted flux averages as a function of the average implantation depth. The open and closed symbols correspond to measurements conducted in the normal and superconducting states respectively. All normal state points were measured at a temperature of 10 K whilst the superconducting state was recorded at 2.5 K which was close to the system base temperature. The normal state measurements, in all cases, simply recover the applied measurement field (B_0) which was set to around 303 Oe. In the superconducting state, for both sample structures, a flux lowering is measured across all sampled energies. In the case of both the NnS and NnSF sample structure the inclusion of the platinum spacer layer appears to prevent the expected enhancement to the screening profile associated with the Cu(40) layer with only a small signal amplitude of $\approx 1\ G$ present within the copper layer. As can be seen from the measurements on the NnS structure, the observed screening amplitude of $\approx 3\ G$ is significantly lower than the value determined for the Nb(50) film from Set II which, as indicated by the dashed profile in figure 6.1a), was found to be $\approx 3.8\ G$. This suggests the platinum layer results in an effective screening thickness which is highly comparable to the Nb(50) film. When one considers the visible enhancement associated with the addition of the ferromagnet (X=CoNbSi) it is well described by the standard form of the EM proximity effect used within chapter 4 and 5. There appears to be an additional amplitude of $\approx 4\ G$, when compared with the X = Si sample, at the S/F interface. Interestingly, the EM effect appears to be weaker when compared with previous chapters despite the use of a consistent ferromagnetic layer. This suggests that whilst the normal metal proximity can enhance the standard Meissner screening it is not necessary to generate the effect. For the NSIF systems $A_{EM} = -13 \pm 1\ G$ whereas here, even accounting for the effects of pair breaking[39], the amplitude is at most half of that value. This is a curious result and given comparable sample layers and interface quality, as would be expected for samples grown in the same vacuum cycle such as these, provides additional evidence that the electromagnetic proximity within these systems appears to scale with the existing Meissner screening current.

In addition to the energy scan results presented within figure 6.1a), muon measurements at fixed probing energy but variable temperature were also carried out for the NnSF system. The results of these temperature scans, conducted at two fixed probing energies, are presented within figure 6.1b). The plotted points represent the extracted average flux values as a function of the measurement temperature where the sample T_c, measured using the low temperature transport system discussed within section 2.2 of the experimental techniques chapter, is indicated by the dashed vertical line for reference. At a probing energy of 23 keV the muons predominantly sample the superconducting niobium layer. For this higher sampling energy the measured signal is onset at T_c and develops as a function of temperature down to the lowest plotted value at T= 4.5 K. Whilst the amplitude of the data is reduced when compared with the standard NSF response the linear temperature dependence is consistent with that shown in appendix D for the trilayer sample. The second temperature scan was conducted at a muon energy of 6 keV. The corresponding stopping profile for this energy sampled only from the copper side of the platinum layer and the measured response appears to be very different. In this case, the diamagnetic screening is suppressed to occur only at lower temperatures, below about T= 6 K, rather than having an onset at the sample T_c. As the temperature is reduced a small flux lowering slowly develops within the copper layer. This is in stark contrast to the behaviour of the proximitised copper in any measured system without a platinum layer, as presented in appendix D, where a screening response appears at T_c and develops steadily with decreasing temperature.

The results of the LEμSR measurements on the NnS and NnSF systems show that the presence of the platinum layer has a significant effect on the behaviour of the sample. Given the severely diminished screening amplitude within the copper layer, which interestingly only appears at temperatures significantly below T_c, it seems reasonable to wonder whether the platinum

---

[39] The pair breaking, as found within chapter 5 for the standard Co(2.4) ferromagnetic layer, results in a reduction of $A_{SF} \approx 2.5\ G$ in the normal Meissner screening amplitude.

layer is largely isolating the Cu(40) layer from the niobium. Such an effect could explain the lack of a normal metal enhancement but - importantly - not the altered temperature dependence of the signal within the copper. Failure of the pairs to propagate through the Pt(10) layer could be due to pair breaking effects occurring within the platinum, the interfaces having a very low transparency or the material itself having an exceedingly short mean free path. Indeed the expected inelastic mean free path of platinum is around 10 nm [164] which is the thickness of the material layer within these samples. Given the critical effect mean free path has on the normal metal - superconductor proximity, as demonstrated through the quasiclassical calculations presented in figure 3.8, this may play a role in explaining the suppressed screening response. If the amplitude of pairs that manage to traverse the platinum is sufficiently small then despite finding themselves in the copper, which under the right conditions can be as effective a screening medium as the niobium, their response may be negligible due to low pair density. In order to investigate the presence, or indeed absence, of proximity induced superconductivity within the normal metal scanning tunnelling microscopy (STM) measurements were carried out. These measurements were conducted as part of a collaboration with the STM group in St Andrews and were performed in their entirety by Dr Chi Ming Yim [165]. The results are included here for reference with his permission.

A set of two sample structures were grown using the same growth system and under the same conditions as the NnS and NnSF samples. The structures were of the form Au(5)/Pt(x)/Nb(50)/Si, as shown within figure 6.2a), with a variable platinum thickness of x= $2, 10$ nm. The thin normal metal cap, which in this case was comprised of gold[40] in the interest of preventing surface oxidation before the STM measurements, protected the underlying sample but more importantly provided a medium in which to measure the presence, or absence, of a superconducting gap at the sample surface separated from the niobium by the platinum layer. The results of the measurements are presented within figure 6.2 with the experimental details, as provided by Dr Chi Ming Yim, given in the associated caption. Panel b) presents a topographic image of the surface from which the differential conductance (dI/dV) maps for the Au(5)/Pt(2)/Nb(50)/Si sample were recorded. The surface, as expected, is polycrystalline and dirty.

---

[40] The results of LEμSR measurements on samples with Au and Cu normal metal layers are highly comparable and so the use of a gold capping layer should have no effect on the details of the sample behaviour.

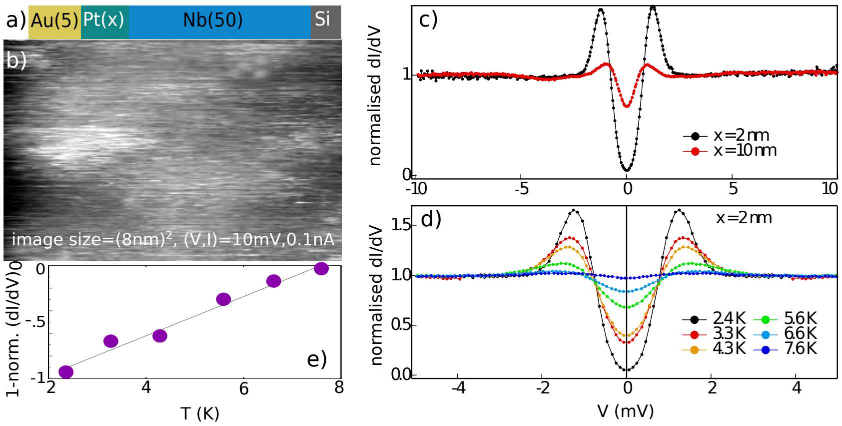

Figure 6.2: STM results on Au(5)/Pt(x)/Nb(50)/Si systems. All measurements were carried out by Dr Chi Ming Yim [165]. a) The sample structure. b) Topographic STM image for Au(5)/Pt(2)/Nb(50)/Si. c) Differential conductance spectra recorded at $T = 2.4\ K$ from the surface of the Au(5)/Pt(x)/Nb(50)/Si samples with x=: (black) 2 nm, and (red) 10 nm. d) dI/dV spectra taken from the sample with $x = 2\ nm$, at different temperatures. e) 1 - normalised dI/dV, at V= 0, as a function of temperature. In c)-d), dI/dV spectra were recorded using the standard lock-in technique, with frequency and amplitude of modulation set at 413 Hz, and 0.2 mV respectively, all superconducting spectra were normalised to the normal state.

The dI/dV spectra recorded at the surface of both the $x = 2\ nm$ and $x = 10\ nm$ samples are presented within figure 6.2c). For both sample structures there is a clear feature at the surface, approximately 3 mV in width, which is typical of a proximity induced conventional superconducting gap (see for example [166]). The amplitude of this gap feature is greatly reduced for the $x = 10\ nm$ sample when compared with the $x = 2\ nm$, almost fully gapped, result as might be expected if the platinum layer is partially isolating the copper from the niobium or indeed if the pairs, for some reason, cannot survive inside the platinum effectively or are destroyed. This latter explanation may also provide a natural interpretation of the delayed onset of an observed net diamagnetic screening response with temperature since it opens up the possibility of generating unconventional pairs, *via* either spin-orbit or weak ferromagnetism, that will in turn generate an opposing paramagnetic response. This opposing response could, over some temperature window in a way dependent on the relative densities of conventional and unconventional pairs, cancel out or even dominate over the diamagnetic screening of the conventional singlets. To investigate the superconducting gap feature further, and to look for any signs of unconventional pairs which may manifest as states within the gap as suggested by the experimental results in references [114, 167, 168], differential conductance spectra were recorded as a function of temperature for the $x = 2$ nm sample. The results of these measurements are shown in figure 6.2d). The height of the coherence peaks and the depth of the trough get progressively smaller with increasing temperature as T_c is approached. This is reflected in the linear dependence of $(1 - dI/dV)$ at zero bias on temperature as plotted in panel e). This confirms the origin of the gap feature on the gold surface. There appears to be no evidence of states appearing within the gap at any of the measured temperatures suggesting that any unconventional pairs present within the system do not survive over a lengthscale long enough to reach the surface. As a final note, whilst for a "conventional" triplet superconductor the expected tunnelling spectra appears as the BCS gap but with a additional states appearing at zero bias, there is no reason to believe that proximity induced states will behave in the same way. Only a single detailed experimental study has been performed on these systems where the gap structure appeared to vary spatially across the sample surface [168]. Further work is required to disentangle the possible contributions to the spectra at the surface in these systems. Not least the effect of impurities, disorder and roughness which are clearly evident features in the topographic map shown in figure 6.2a) and have been shown in the aforementioned study to correlate with the different types of measured gap structure.

The combined results of the LEμSR and STM measurements on the NnS and NnSF sample structures show that the inclusion of the platinum layer at the N/S interface has a significant effect on the behaviour of the sample. It appears that the superconductivity is suppressed by the platinum, which prevents any appreciable enhancement to the screening response associated with the presence of the normal metal layer but still allows the copper to proximitise through a spacer layer up to at least 10 nm thick. The delayed onset of the response on the copper side when compared with T_c, and indeed the onset observed within the bulk of the niobium layer, suggests this is not simply a mean free path or partial isolation effect. The STM results do show the presence of a gap at the surface of the sample, even in the sample with a 10 nm thick layer of platinum at the N/S interface, but no clear signature of any unconventional states could be extracted from the spectra measured at the surface. The results presented within this section are specific to the inclusion of platinum and warrant further exploration of its use as a "normal" metal layer within these thin film heterostructure systems.

6.2.2 The effect of a platinum spacer layer on the S/F proximity

As discussed within chapters 4 and 5 the new electromagnetic proximity theory has provided a means to interpret a number of previously anomalous observations within this field [39, 60, 82, 85]. The results presented within chapter 5 explored the dependence of the electromagnetic proximity on the coupling between the superconductor and the ferromagnet. Whilst a clear connection between A_{EM} and the coupling strength was established, meaning the source is somehow the interaction between S and F, the mechanism through which the EM proximity effect is generated within these systems could not be unambiguously identified. Within this section the focus is on manipulating the S/F interface, and the associated proximity effects, using instead a thin platinum spacer layer. As presented within section 6.2.1 platinum clearly has an effect on the proximity across the N/S interface so it may be expected to alter both the direct and EM proximity occurring at the S/F interface.

In order to investigate the effect of a platinum spacer layer on the S/F proximity an NSnF sample of the form Cu(40)/Nb(50)/Pt(2)/Co(2.4)/Nb(3)/Si was grown under the same conditions, and using the same niobium target purity, as sample Set I defined in chapter 3. In light of this the relevant control samples for comparison are S(I), NS(I) and NSF(I) as previously measured and modelled in detail within chapters 3 and 4. The standard set of LEμSR measurements were carried out on this NSnF sample structure and the results of both the energy and temperature scans are presented within figure 6.3. The top panel of figure 6.3a) displays some example muon stopping profiles for the platinum spacer sample. For $E_\mu \geq 20\ keV$ the muons begin to sample the region around the Pt(2)/Co(2.4) interface. The corresponding vertical lines indicate the average probing depth in each case. The main panel of figure 6.3a) presents the results of the averages analysis of the muon data. The plotted points represent the extracted flux averages as a function of the average probing depth where the plotting convention is consistent with that used in figure 6.1. Error bars are also plotted for each measurement point and typically fall within the range of $(0.1 - 0.3)\ G$ which in some cases is smaller than the symbol size. For all normal state data points the applied field, which was set to around 302 Oe, is recovered. In the corresponding superconducting state measurements there is a flux lowering observed across all probing energies. The average field values show a total screening amplitude of roughly 5 G which when compared with the control NS(I) response of 4.5 G appears to suggest the NSnF sample is behaving simply like the corresponding bilayer. This implies that the EM effect is largely destroyed simply due to the presence of a 2 nm thick platinum spacer layer. This is curious since in the previous chapter it took 8 nm of oxide at the S/F interface to completely kill-off A_{EM}. Focusing instead on panel b) of figure 6.3, however, it is possible that the previous statement was a bit premature.

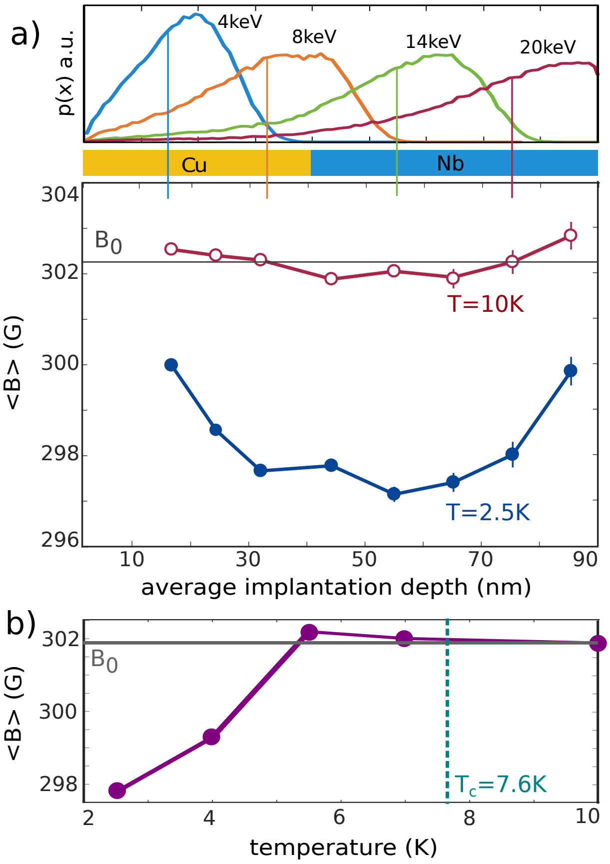

Figure 6.3: LEμSR results for the trilayer with a platinum spacer layer at the S/F interface. a) The top panel shows the stopping profiles for a range of different incoming muon energies with the average probing depths indicated by the corresponding vertical lines. For $E_\mu \geq 20$ keV the muons begin to sample the Pt/Co/Nb layers (not shown). The main panel presents the results of the averages approach to analysing the LEμSR data. All normal (superconducting) state data were measured at $T = 10(2.5)$ K and are plotted using open (closed) symbols. The lines are just a guide to the eye. b) The average field as a function of the sample temperature where the line is just a guide to the eye. The data were measured at a fixed muon energy of 11 keV which sampled symmetrically about the CuNb interface. The horizontal line marks the applied field B_0 and the vertical dashed line indicates the sample T_c found from transport measurements.

Plotted are the average flux values, measured for a muon probing energy of 11 *keV* which focuses around the NS interface for maximal signal, as a function of the sample measurement temperature. The vertical dashed line indicates the sample T_c which was determined *via* transport measurements to be 7.6 K. It is immediately obvious that the delayed onset of the screening with temperature previously observed within the copper layer of the NnSF structure is replicated. In both systems the size of the shift is approximately 2 K. Interestingly, the temperature scan in this case was conducted at a probing energy which measured predominantly across the N/S interface far away from the platinum layer. This implies that a platinum layer at either side of the niobium can suppress the apparent onset of screening with respect to T_c. The extracted averages appear to show a slight up-tick in the measured flux over the region where no diamagnetic response is observed. The reason for this is not clear but it may be related to two conflicting contributions to the total flux profile within that temperature window.

Given that the energy scan measurements were conducted at only 3 K below the onset temperature ($(T_c - 2)$ K) of a net diamagnetic screening, it no longer seems appropriate to directly compare the extracted NSnF amplitude to the NS(I) result which was measured almost 6 K below its respective onset temperature (T_c). Additionally, it is not clear whether the observed delay in the screening response corresponds to two opposing contributions cancelling out over a small temperature window or whether no screening is taking place at all until some lower threshold temperature is reached. What is clear, however, is that the thin platinum layer at the S/F interface is able to influence the measured behaviour across the full spatial extent of the sample. In light of this, it is possible that the platinum layer modifies the EM response at the S/F interface generating a sharp paramagnetic amplitude, which is cancelled by the diamagnetic Meissner screening, the latter only beginning to dominate at temperatures lower than 5.5 K. Further evidence for this can be seen from the data presented within appendix D where a comparable structure, this time with a Cu(2) spacer layer and a niobium quality consistent with Set II, was measured in the same way. The results on the copper spacer sample suggest the conclusions of chapter 5, that the gap strength in addition to the coupling strength between S and F, may be important also within these systems involving normal metal spacers. In the case of the copper, whilst the magnitude of the

EM proximity response is reduced when compared with NSF(II), possibly due to the proximity induced gap being weaker than the gap of the niobium, the sign is preserved. In the case of the platinum spacer, on the other hand, owing to its unusual material parameters the results seem to suggest the magnitude of A_{EM} is reduced, possibly also due to a weaker gap, and the sign appears to have flipped. The EM proximity theory predicts a change in sign concurrent with a change in $R = d_F/\xi_f$ and suggests that for a dirty system, such as the ones studied here, the generated amplitude decays with increasing R [40]. In the case of the Pt(2) spacer layer, in the presence of the applied field, the value of R could very well be altered whereby the full Pt(2)/Co(2.4) segment becomes a sort of composite ferromagnetic layer. This could drive the system into a regime where a smaller but paramagnetic EM response is instead generated. In order to test this hypothesis in detail, further study of the field dependence of the measured signal is required since the ability of the platinum to generate unconventional superconducting states will scale with the applied field. It is important to note, however, that in the case of the NnSF sample a similar, albeit smaller in amplitude, effect is present around the CuPtNb interface region remote to the cobalt. This seems to suggest that the cobalt layer is not required to produce the observed delayed onset in the net screening.

6.3 Platinum as the normal metal layer

Within the present section platinum is used as a replacement for copper in both the bilayer and trilayer sample structures. Given the results of the experiments carried out on the samples with spacer layers in section 6.2, platinum appears to both be a useful tool for investigating the various contributions to the muon signal and is interesting in its own right as a material layer within these sample structures. The experimental observations suggested the possibility of the platinum hosting unconventional superconducting states and a resultant flipping in sign of the electromagnetic contribution to the muon signal. Further measurements and modelling are required to draw any strong conclusions however. In order to further investigate this possibility, and in order to probe the response of platinum in a more focused way, a set of detailed LEμSR measurements were performed on samples with thick Pt layers. It was hoped that these measurements could shed some light on the behaviour of the platinum spacer layers presented within section 6.2.

6.3.1 LEμSR results on platinum bilayer samples

In this work the focus is on the behaviour of platinum bilayer systems. LEμSR measurements as a function of probing energy, temperature and applied field are performed on these sample structures and some startling experimental results obtained. In many cases the results provide further insight into the observations of section 6.2. The samples studied here are simple NS bilayers of platinum and niobium. It has already been demonstrated that the addition of a ferromagnetic layer greatly boosts the observed measurement signal *via* the action of an EM proximity effect. This maximises the chances of observing any novel effects occurring within the sample platinum layers, however, the addition of the ferromagnetic layer also increases the muon depolarisation rate and complicates the physics of the sample. Rather than include a further layer of complication the decision was made in this study to simply increase the thickness of the niobium layer such that the Meissner screening signal would be increased.[41] With the aim of being able to both study the platinum layer in detail and to reach the niobium layer, in order to probe the associated physics occurring therein, two bilayer sample structures of differing platinum layer thickness were grown in the same way as described within section 3.2:

i) A Pt(60)/Nb(100)/Si system, the purpose of which was to probe around the Pt/Nb interface and into the niobium layer. The hope was to both study the effect of the platinum on the screening response of the niobium and investigate the possibility of an EM response associated with the platinum layer.

ii) In order to probe the platinum side of the interface in more detail a second bilayer of the form Pt(100)/Nb(100)/Si was also grown and measured.

Within this section the conventional averages approach to the muon data analysis, discussed in detail within section 2.1, is taken as opposed to a full spatial profile analysis. This is in part due to a lack of control samples specific to this sample series and in part because this work provides a first look at what is happening within these wholly platinum-niobium based systems.

---

[41] The only associated downside is that the samples previously measured, and grown under the same conditions, can no longer be used as quantitative control samples since the behaviour will now be very different.

To get a handle on the behaviour of the full Pt/Nb interface region an energy scan on the Pt(60)/Nb(100)/Si bilayer system was first performed. The results of this measurement are displayed within figure 6.4 which presents plots of the extracted average flux and the muon depolarisation rate as a function of the average probing depth. The top panel of figure 6.4a) presents some sample muon stopping profiles for the Pt(60) bilayer where the corresponding vertical lines indicate the average stopping depth in each case.

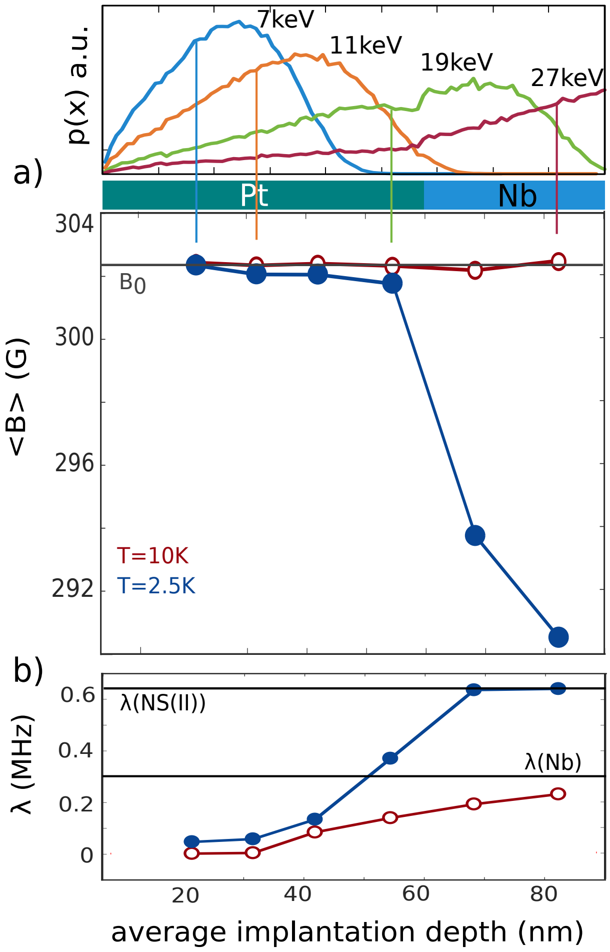

Figure 6.4: LEμSR results for the Pt(60)/Nb(100) bilayer sample. a) The top panel displays the muon stopping profiles plotted for a few select energies. The corresponding vertical lines indicate the average probing depths in each case. The main panel shows the extracted averages plotted as a function of the average probing depth. b) The plotted points indicate the muon depolarisation rate as a function of the average probing depth. Included for reference are the λ values, indicated by the horizontal lines as labelled, for Nb and the comparable purity NS bilayer. In a)-b) the open (closed) symbols correspond to the normal (superconducting) state measurements conducted at $T = 10\ K$ ($T = 2.5\ K$). The lines are a guide to the eye.

The layer thicknesses were designed such that the full range of measurement energies, which spanned a range $(7-27)\ keV$ in this case, allowed:

i) the platinum to be uniquely probed for $E_\mu < 19\ keV$,

ii) the interface region to be probed approximately equally from both sides for $E_\mu = 19\ keV$ and

iii) the niobium layer to be predominantly sampled for $E_\mu > 19\ keV$.

Perhaps the most key of these measurement energies, as it turns out, is $E_\mu = 19\ keV$ as will be discussed in detail in what follows. The main panel of figure 6.4a) displays the results of the conventional averages approach to the muon data analysis plotted with reference to a simple schematic of the sample structure which indicates the position of the interface for reference. All normal state measurements were performed at a temperature of $T = 10\ K$ and are plotted using open symbols. The corresponding superconducting state measurements were carried out at a temperature of $T = 2.5\ K$ and are plotted using closed symbols. Within the normal state the applied measurement field, which was set to around 302 Oe, was recovered across all of the measurement energies. The superconducting state results are, however, a different story entirely. The measurement energies which probe primarily the platinum, $E_\mu < 19\ keV$, appear to return a net signal within error of the applied measurement field. Turning to the energies focused on the bulk of the niobium, $E_\mu > 19\ keV$, it is clear that there is a large diamagnetic screening developing towards the centre of the superconducting layer as expected. At first glance the results look like an N/S proximity but where the N layer has a low mean free path and does not readily proximitise but the key measurement at $E_\mu = 19\ keV$ indicates something far more interesting is going on. For a muon probing energy of exactly $E_\mu = 19\ keV$ the corresponding stopping profile clearly shows an average stopping distance very close to the interface between the platinum and the niobium.[42] If the sample was generating no signal within the platinum and a Meissner screening within the niobium then the expected result would be a significant flux lowering associated with the muons sampling the first 30 nm of the superconductor. Instead the measurements show only a slight flux lowering, roughly equivalent to the error bar on the data, when compared with the corresponding normal state data point. This strongly

---

[42] In the standard CuNb bilayers samples previously measured this probing energy would correspond to the maximum signal amplitude as presented within chapter 3

suggests that the weighted sampling across the Pt/Nb interface is averaging two separate contributions to the total signal: a diamagnetic component and an equally weighted paramagnetic response, over the spatial width of the stopping profile. Given the results for $E_\mu < 19\ keV$, which sample largely on the platinum side of the interface and measure no net response, this second component seems to be appearing within the niobium layer. Further evidence for this can be seen from the results of extracting the muon depolarisation rate as a function of the average probing depth. The results of this analysis are presented within figure 6.4b) using the same plotting convention as for the average field data within panel a). The normal state data show the muon depolarisation rate (λ) within the platinum layer is extremely small. This is advantageous in the quest to resolve small differences since the damping on the signal is exceedingly small within this region.[43] As the probing energy increases and samples progressively more of the niobium the depolarisation rate begins to increase towards the usual normal state value of $\approx 0.3\ MHz$ for niobium which is associated with its nuclear depolarisation. Within the normal state spatial dependence of λ it is clear that for $E_\mu > 11\ keV$ the muons begin to sample the niobium since it is at this point the average value begins to climb. In addition, for $E_\mu = 19\ keV$ the average λ value reflects the approximately 50/50 sampling of the platinum and niobium layers. In the superconducting state the results show an increase in λ across all measurement energies. This is interesting since it implies the superconductivity, whilst not generating a measurable screening current, is influencing the full spatial extent of the platinum layer. Interestingly, at $E_\mu = 19\ keV$ there is a clear signature the sample is superconducting and flux gradients are present since there is a rapid increase in λ towards values typical of the superconducting bilayer response. At the highest energies, for which a clear diamagnetic Meissner response is seen in the average field, the system settles on $\lambda \approx 0.6\ MHz$ which is directly comparable to the response of the niobium layer within NS(II) shown in figure 3.6. This implies that deep within the niobium the flux gradients are similar to those associated with the standard cosh profile across the CuNb bilayer sample.

In order to investigate the platinum layer in more detail a corresponding energy scan was performed on the Pt(100)/Nb(100)/Si bilayer system. The

---

[43] A feature of platinum which will be important for the measurements performed on the Pt(100) sample presented within figure 6.5.

results of these LEμSR measurements are presented within figure 6.5. The top panel of figure 6.5a) presents the corresponding muon stopping profiles for a set of energies spanning the full measurement range. The corresponding vertical lines in each case indicate the average probing depths which all lie within the platinum layer. For $E_\mu < 27\ keV$ all muons stop only within the platinum layer, which extends beyond the x-axis of the figure, whilst at $E_\mu = 27\ keV$ a small fraction of muons sample the niobium layer.

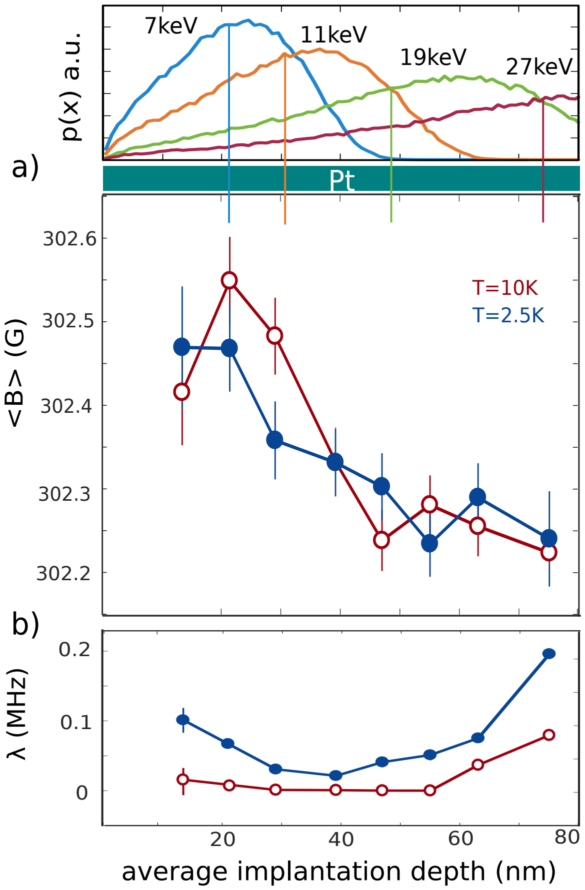

Figure 6.5: LEμSR results for the Pt(100)/Nb(100) bilayer sample. a) Top panel: muon stopping profiles for a range of different probing energies. The corresponding vertical lines indicate the average probing depth for each incoming muon energy. Even at the highest measurement energy ($E_\mu = 27\ keV$) all muons stop within the Pt(100) layer. Main panel: the results of the conventional approach to the data analysis are shown. The plotted points represent the average field as a function of the average probing depth. b) The plotted points indicate the muon depolarisation rate as a function of the average probing depth. In a)-b) the open (closed) symbols correspond to the normal (superconducting) state measurements conducted at $T = 10\ K$ ($T = 2.5\ K$). In each case the lines are simply a guide to the eye.

The results of the averages analysis to the muon data are presented within the main panel of figure 6.5a) where all the measurement and plotting conventions are consistent with figure 6.4. Within the normal state the applied field, in this case set to around 302.3 Oe, was simply recovered. The corresponding superconducting state measurements show no discernible difference in average field values when compared with the normal state. Even given the small error bars, thanks in part to the exceedingly low muon depolarisation rate within the platinum, no systematic difference in average field is resolved above and below T_c which suggests a lack of a measurable screening response across the full material layer of platinum. This null result also indicates that within the temperature range $(2.5 - 10)$ K the properties of the platinum layer are not changing appreciably enough to alter the measured field. The story is different, however, when one considers the behaviour of the second moment with average probing depth. The results of extracting λ as a function of the average probing depth, measured above and below T_c, are shown within figure 6.5b). There is a clear shift in the depolarisation rate within the superconducting state to higher values across all measurement energies. This is indicative of some measure of the superconductivity extending across the full spatial extent of the platinum layer. Given the shift is largely constant across all energies the origin may be stray field related. The shift in λ does therefore provide a proxy to indicate the niobium layer, which cannot be probed directly, is superconducting.

In addition to the energy scans performed on both the platinum bilayers, temperature scans at a fixed muon probing energy were also carried out. The results of the temperature scans on both are presented within figure 6.6. In the case of the Pt(60) bilayer for high muon probing energies the average field and the muon depolarisation rate show a systematic behaviour with decreasing temperature, however, in the Pt(100) sample the average field values show no discernible difference in signal above and below T_c though it is still possible to monitor the superconductivity *via* the behaviour of λ. Figure 6.6a) presents the extracted average field values as a function of temperature for the Pt(60) sample measured at a fixed muon probing energy of 27 keV. The applied field B_0, which was set to approximately 302 Oe for the duration of the measurement, is indicated by the solid horizontal line for reference. In addition, the sample T_c was determined *via* transport measurements to be 8.3 K and is indicated by the dashed vertical line.

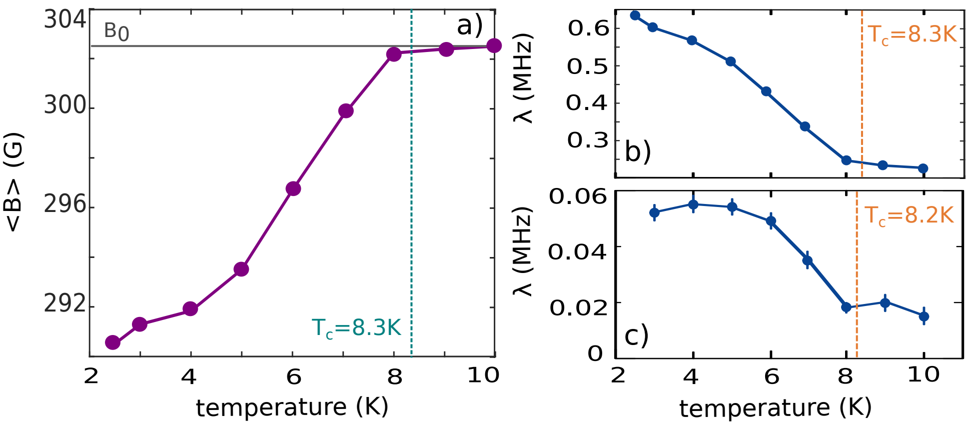

Figure 6.6: The temperature scan results for the platinum bilayers. a) The average field plotted as a function of the temperature for the Pt(60)/Nb(100) bilayer measured using a muon probing energy of $E_\mu = 27\ keV$. B_0 indicates the applied measurement field. b) The muon depolarisation rate as a function of the measurement temperature for the Pt(60)/Nb(100) with a fixed energy $E_\mu = 27\ keV$. c) The muon depolarisation rate as a function of the measurement temperature for the Pt(100)/Nb(100) sample measured at $E_\mu = 11\ keV$ In a)-c) the vertical dashed lines indicate the corresponding sample T_c values extracted from transport measurements and the connecting lines are just a guide to the eye.

The average flux values show the signal is onset at T_c and develops linearly with decreasing temperature until it begins to level-off for the lowest measurement temperatures. Contrary to the samples with platinum spacer layers there is no evidence of a temperature shift of the net response with respect to T_c at the muon probing energy. Given the possible net paramagnetic response would be spatially localised at smaller probing depths near the Pt/Nb interface, only a small weight of muons stop within the region of the sample where it may dominate over the diamagnetic screening. The measurement response at $E_\mu = 27\ keV$ shows the development of the diamagnetic screening with decreasing temperature, which as seen in panel a), takes a conventional form. The corresponding temperature dependence of the depolarisation rate, displayed in panel b) of figure 6.6, is highly consistent with this interpretation. For the Pt(100) bilayer sample the muon depolarisation rate as a function of the average probing depth was measured for a fixed muon probing energy of $E_\mu = 11\ keV$. The results are presented within figure 6.6c). The data points represent the extracted values and the dashed vertical line indicates the sample T_c value of $8.2\ K$ found from simple transport measurements. Once again the increase in λ

is clearly onset at the superconducting transition temperature and develops with decreasing temperature until it levels off towards the base temperature of the measurement system.

The final measurement performed on the platinum bilayer structure was the field scan presented within figure 6.7. This was measured at a probing energy of $E_\mu = 27\ keV$ for the Pt(60)/Nb(100)/Si system. The figure plots $\delta B = \langle B_{10\ K} \rangle - \langle B_{2.5\ K} \rangle$ against the applied measurement field. The data points are the extracted values whilst the connecting line is the best-fit power law description optimised using the Levenberg-Marquardt method as discussed in appendix A. Interestingly, the data show a non linear reduction in the system response with decreasing applied field. The power law, $\delta B = \alpha B_0^{3/2}$, is an excellent description of the data, at least over the small range of experimentally accessible applied field values, showing the measured effect dies off more rapidly than a standard Meissner response. The origins of this apparent power law dependence are, however, unclear.

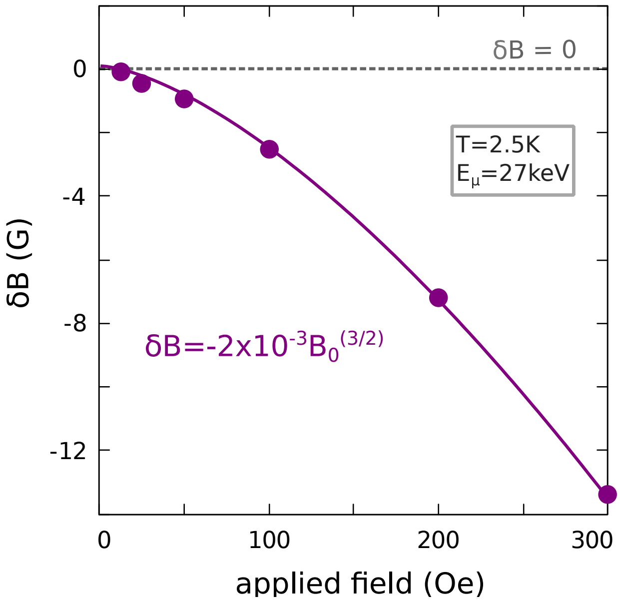

Figure 6.7: The field dependence of the muon signal for the Pt(60)/Nb(100) bilayer sample. The plotted points indicate the difference between the extracted average field values measured at $T = 10\ K$ and $T = 2.5\ K$, using a probing energy of $E_\mu = 27\ keV$, plotted as a function of the applied measurement field. The solid line is the (3/2) power law fit to the data with the corresponding equation displayed where the fit was optimised as discussed within appendix A. The horizontal dashed line represents a zero screening amplitude.

The field dependence measured on the NSF(I) system in chapter 3, on the other hand, is almost perfectly linear down to low applied field. As noted within section 3.4.4 and appendix E the extraction of average field values becomes more difficult for low applied measurement fields. Whether or not the data indeed tend toward $\delta B(0) = 0$, as is suggested by the low field values in figure 6.7, or instead extrapolate to a positive y-intercept is therefore not easy to determine for certain simply from these transverse field measurements. In order to better investigate the physics at low and zero applied field, muon measurements in alternative longitudinal measurement geometries could be vital.

Taken all together the results of the energy, temperature and field scans on these platinum based bilayer structures suggest that either the presence of the platinum is having a severely damaging effect on the superconductivity within the niobium layer or is producing a compensatory paramagnetic feature that dies off over a lengthscale on the order of a few tens of nanometers into the niobium. The former mechanism seems highly unlikely and it is difficult to think of a physically justifiable reason for the platinum to be so damaging to states deep within the niobium. The latter explanation, on the other hand, provides a natural framework in which to interpret the results and is in agreement with some of the results on the platinum spacer samples which implied the presence of a sign reversed A_{EM}. The non-linear field dependence of the total signal amplitude points to something other than a simple orbital effect, perhaps related to the magnetic susceptibility of the platinum though further measurements, possibly using the SQUID to probe the magnetic characteristics of the platinum, are required before any firm conclusions can be drawn.

Given the evidence available at the time of writing it was not possible to model this data using the full spatial analysis method. The results of the energy scans on the Pt(60)/Nb(100) and Pt(100)/Nb(100) bilayer samples, however, suggest a small pool of possible profiles which could sensibly generate the observed average data. A schematic diagram of one such profile is presented within figure 6.8. This proposes the full superconducting state profile ($B_s(x)$) to be the sum of a standard Meissner screening ($B_{ms}(x)$) profile with a paramagnetic EM response, of amplitude A_{EM}, originating at the Pt/Nb interface. This choice would also be broadly consistent with the measurements on platinum spacer samples presented within section 6.2.

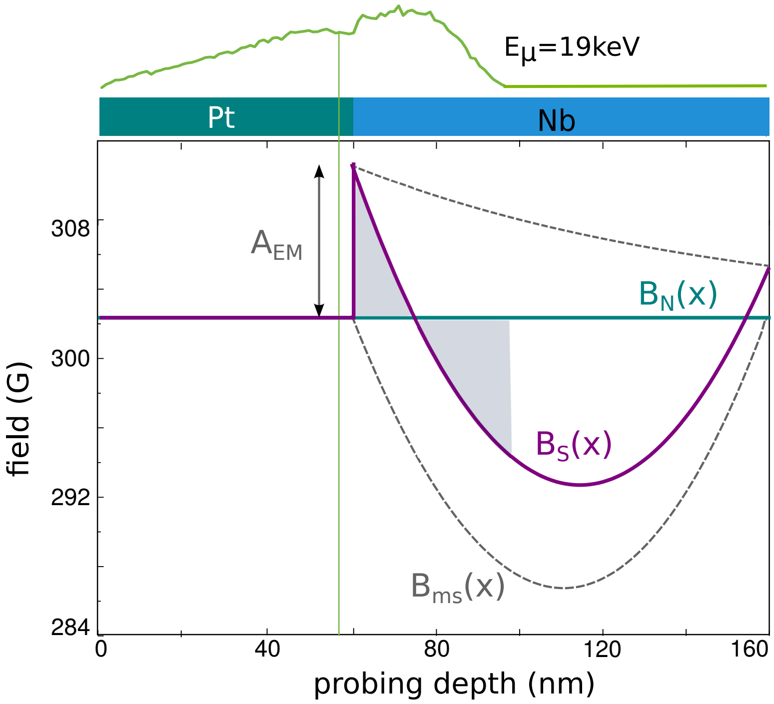

Figure 6.8: A schematic diagram showing one possible spatial profile for the screening response across the Pt(60)/Nb(100) bilayer sample. In the normal state, a constant applied field profile is represented by $B_N(x)$ The full superconducting state profile ($B_S(x)$) is composed of two contributions: a standard Meissner screening ($B_{ms}(x)$) and a paramagnetic EM response, of amplitude A_{EM}, generated at the Pt/Nb interface. The $E_\mu = 19\ keV$ stopping profile is shown alongside to illustrate the possibility for two such contributions to cancel across the width of a stopping profile as indicated by the shaded regions.

The Meissner screening component $B_{ms}(x)$ was chosen to be consistent with the response of NS(II) which, as the quasiclassical calculations presented within figure 3.8 suggest, should not be too dissimilar to a Nb(100) thin film response. In addition, the value of A_{EM} was set to be 8 G such that over the width of the 19 keV stopping profile the two contributions largely cancel out as indicated by the sampled shaded regions. An EM component, of either sign, can only be generated where the niobium comes into contact with an additional source of vector potential. In the case of platinum this could potentially be provided by spin-orbit interaction or Stoner enhanced paramagnetism. Whilst no firm conclusions can be drawn from figure 6.8 without a full implementation of the model on the data it is suggestive of what may be going on within these samples.

6.3.2 LEμSR results on a platinum trilayer

As a final test of the properties of platinum within S/F hybrid heterostructures a simple platinum based trilayer was grown, using the same growth system and purity niobium target as sample Set I discussed within chapter 3, and measured using LEμSR. The original aim of these measurements was to investigate whether the platinum layer is capable of generating a paramagnetic Meissner response, such as the one observed for a AuHoNb system [32], due to the presence of unconventional superconducting states generated by the platinum. This would rely on the Stoner enhanced properties of platinum whereby, due to a large density of states at the Fermi level resulting in a large magnetic susceptibility, in an applied magnetic field the conventional Cooper pairs can be phase shifted in such a way as to generate triplet correlations. No net screening amplitude was observed within the platinum layers of the bilayer sample structures, however, a clear signature of superconductivity deep in the platinum layer was reflected within the behaviour of λ as a function of temperature. Whether or not this was simply due to stray fields associated with steep flux gradients within the niobium is difficult to determine, though the STM measurements on the platinum spacer samples show the superconductivity can traverse at least 10 nm of platinum.[44] One possible explanation of zero net screening in the platinum could be the generation of equal paramagnetic and diamagnetic screening densities which cancel out though this is largely conjecture. Extension to the trilayer case is expected to have two consequences on the flux profile. The EM proximity at the S/F interface should boost the overall signal amplitude whilst pair breaking effects will reduce the standard Meissner screening response. It was initially unclear whether or not this would turn out to be advantageous for the aims of this measurement or whether the inclusion of the strongly ferromagnetic layer would have any effects on how the screening current interacts with the thick platinum cap.

The trilayer structure measured was of the form Pt(60)/Nb(50)/Co(2.4)/Nb(3)/Si. It was hoped that the Co layer would give the overall signal a boost and that the thicker Pt layer, when compared with the usual thickness of copper, would allow both the Pt layer and the Pt/Nb interface to be probed in a more spatially localised way whilst avoiding pollution of the signal due to the expected diamagnetic response of the Nb. The results of the performed LEμSR measurements are presented within figure 6.9.

---

[44] This suggests $\xi_S \approx 7\ nm$ within the platinum layer.

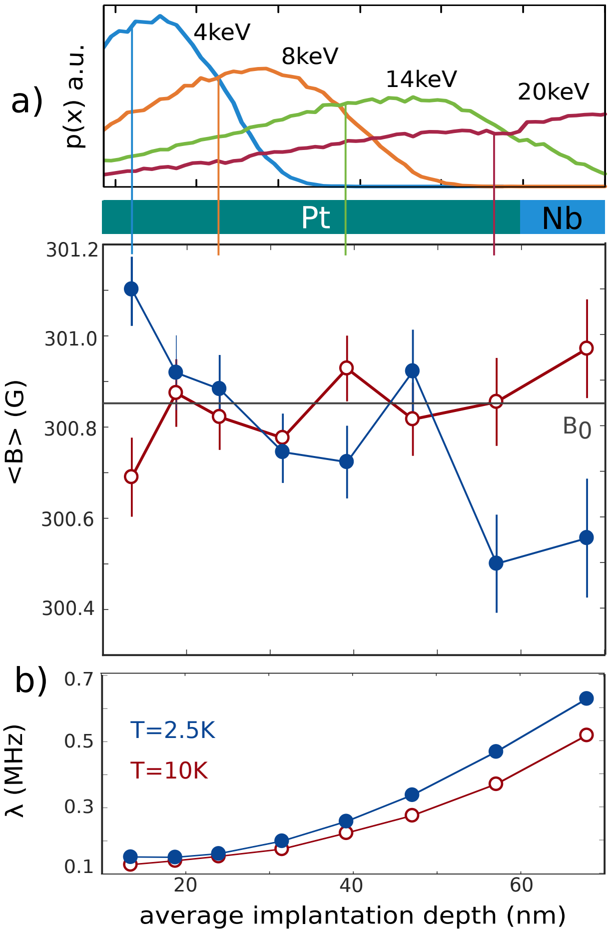

Figure 6.9: LEμSR results on a Pt(60)/Nb(50)/Co(2.4)/Nb(3)/Si trilayer sample. a) The top panel presents some sample muon stopping profiles for the platinum trilayer where the corresponding vertical lines represent the average probing depth in each case. Main panel: The average field as a function of the average probing depth is plotted. The applied measurement field B_0 is indicated for reference. b) The muon depolarisation rate as a function of the average probing depth. In a)-b) the open (closed) data points represent measurements taken in the normal (superconducting) state at $T = 10\ K$ ($T = 2.5\ K$). The lines are just a guide to the eye.

Within the top panel of figure 6.9a) are presented the muon stopping profiles, plotted over a range $(10-70)\ nm$, where the corresponding vertical lines indicate the average probing depths. Importantly for $E_\mu \leq 8\ keV$ the muon stopping profiles are localised to the platinum layer. For any subsequent increase in E_μ, the stopping profiles begin to sample the niobium layer with increasing weight. For $E_\mu = 20\ keV$ the average probing depth is close to the Pt/Nb interface. Within the main panel of figure 6.9a) are plotted the results of the averages approach to analysing the LEμSR data. All normal state measurements were conducted at a temperature of $T = 10\ K$ and are plotted using open symbols. The corresponding superconducting state measurements were performed at $T = 2.5\ K$ and are indicated by the closed symbols. In the normal state, as with all measurement series, the applied measurement field was recovered. In this case $B_0 \approx 300.8\ Oe$ as indicated by the solid horizontal line. Within the superconducting state, for the majority of energies, there is no clear difference in the data above and below T_c. Within the platinum layer at the lowest sampled energy, which captures the surface 50% of the platinum, there appears to be a net paramagnetic response, however, for $E_\mu = (6 - 17)\ keV$ there is no real net difference. At the highest measured energies, $E_\mu = (20, 23)\ keV$, only a very small net diamagnetic amplitude of approximately 0.4 G is observed despite a stopping profile which significantly samples the niobium layer and the addition of the cobalt layer to boost the signal amplitude.

The average flux data presented within figure 6.9 are somewhat similar to the results for the thin gold capped sample in appendix F. This suggests that within the trilayer structure, in contrast to what was observed within the platinum bilayer and spacer samples, the platinum does not seem at first glance to be contributing to the measured screening. It is possible, however, to explain the data in a way consistent with the previous observations as follows. Within the platinum layer there is no net signal, this would be consistent with the observations made on platinum bilayers within section 6.3.1, and that the total amplitude within the niobium layer comprises three separate contributions: the normal Meissner screening which is known to be at most 1 G for samples grown using lower purity Nb; the diamagnetic A_{EM}, that appears to scale somehow with the screening current, associated with the Co(2.4) layer and a paramagnetic A_{EM} associated with the platinum interface. Given the overall amplitude of approximately 0.4 G it seems likely that within this picture the two opposing EM contributions are similar in magnitude such that the net result is close to, but slightly smaller than, the expected Meissner amplitude for a corresponding probing depth of up to 30 nm into the niobium. If it were possible to probe nearer the region close to the S/F interface the opposite effect, that the amplitude is slightly larger than the expected Meissner response, ought to be observed. If this interpretation is along the right lines, one might expect the behaviour of the depolarisation rate as a function of the average probing depth to also be consistent with the behaviour observed for the platinum bilayer samples. Figure 6.9b) presents the extracted λ values as a function of the average probing depth above and below T_c. The corresponding plotting and measurement conventions are the same as those used within panel a). Across all energies there is an increase in λ below the superconducting T_c when compared with the values in the normal state. It is more difficult to see precisely the point at which the weighted niobium sampling begins to dominate over the platinum since the whole behaviour is moderated by the exponential increase in rate as the average depth approaches the ferromagnetic layer. The shift in λ above and below T_c is, however, smaller than in the bilayer samples which had both thicker and higher quality niobium and no possibility of an opposing A_{EM} due to the lack of a cobalt layer. This suggests that any change in flux gradients associated with T_c within the trilayer are smaller. This could reflect both a lower signal amplitude or the superposition of three partially cancelling signals since both would result in a flatter flux landscape than observed within the bilayer systems hence the smaller shift in rate.

6.4 Discussion and conclusions regarding the results on platinum within NSF heterostructures

In the first part of the chapter, an investigation into the effects of inserting thin platinum spacer layers at both the N/S and S/F interfaces was presented. Here it was concluded, from the results of STM measurements performed at the sample surface, that the platinum layers were transparent to superconducting pairs for thicknesses of up to at least 10 nm. Within the copper layer of the NnS and NnSF samples, however, only a very small screening amplitude of ≈ 1 G was observed. This lack of a substantial response within the copper layer could be related to many different factors: a lower mean free path of platinum when compared with copper, which as seen from the quasiclassical calculations presented within figure 3.8, could result in the screening remaining entirely contained within the niobium; a high interface resistance at the Pt/Nb interface; a short spin diffusion length, which would prevent the transmission of spin correlations, within the platinum; or two compensating effects occurring over the same region being averaged by a muon stopping profile. The first of these explanations appears to be the most likely but cannot be the only mechanism at play since the net signal for all platinum containing samples is always significantly reduced, rather than being identical, when compared with the relevant control sample. Moreover, the curious temperature dependence observed, so far only in systems involving both thin platinum spacers and cobalt layers, could potentially be explained *via* a gap dependence of some additional paramagnetic component of the signal. The temperature dependence of the signal within S(II), please see appendix D, suggests the gap builds up down to temperatures of $\approx 5\ K$ with any further decrease in temperature not resulting in an appreciable further increase in the screening response. Curiously, the delayed diamagnetic response for the platinum spacer samples begins to kick in at around $T = 5.5\ K$. It seems plausible that the possible paramagnetic component could scale with the niobium gap strength in such a way that it exactly cancels the diamagnetic component of the full NS section over some temperature window. For the samples measured here, this appears to be the case until a threshold is reached at $T = 5.5\ K$ where the temperature dependence of the NS section begins to dominate over the gap and a net diamagnetic response is observed.

The latter half of the work focused on the properties of thick material layers of platinum. The observations made within the section on platinum based bilayers strongly suggest that in addition to the standard diamagnetic screening response there is a paramagnetic amplitude at or near the Pt/Nb interface. This was hinted at through both the absence of a net screening response deep within the niobium and the increase of λ below the superconducting transition which implied the occurrence of flux gradients around the interface region. These observations were so clear, in part, thanks to the exceedingly low base muon depolarisation rate within the platinum in this simple structure. Interestingly, the field dependence of the signal dropped off in a non-linear and more rapid fashion than expected for a standard Meissner screening effect which, suggests the possibility of an additional component to the field dependence. This could be related to the material properties of platinum though the precise nature of the effect is difficult to ascertain from the present evidence. SQUID measurements, to fully characterise the behaviour of the platinum layer, and muon measurements in zero field or which utilise alternative measurement geometries could be key to understanding its origins.

In light of the measurement results on the platinum bilayer systems, a spatial profile involving the sum of a standard Meissner component with a paramagnetic EM amplitude originating at the Pt/Nb interface was proposed as a possible explanation for the data. A full implementation of the model is required before any firm conclusions can be drawn but the proposed profile does have the potential to explain the experimental observations. More generally, if the ideas from this proposed bilayer analysis are extended across the other sample structures then a broadly self-consistent picture starts to emerge. The possible presence of a substantial paramagnetic EM component at the Pt/Nb interfaces requires there to be some additional source of vector potential at the interface in question which acts against the usual diamagnetic screening response. Possible sources include the Stoner enhanced paramagnetism and strong spin-orbit coupling of platinum. This further suggests the importance of detailed measurements on the properties of these systems where it may also be useful to compare the behaviour of platinum to that of other heavy metals.

The combined set of measurements performed on these NSF heterostructures containing platinum has demonstrated the importance of material parameters to all aspects of proximity effects within SF hybrid systems. Clearly the platinum has a substantial effect on the overall muon signal which appears to involve the generation of unconventional states and the possibility of an associated paramagnetic EM amplitude. A detailed spatial analysis of the data and a solid determination of the origin of the observations through systematic characterisation measurements is required. In order to achieve these aims further SQUID and muon experiments are likely to provide added insight on the precise role of the platinum within these structures such that more firm conclusions may be drawn.

7 | Concluding remarks and future outlook

The body of work discussed within this thesis has addressed a number of interesting, and in some cases previously unknown, phenomena within S/F hybrid heterostructures. The initial LEμSR experiments, conducted on simple thin film systems comprising normal metal, superconductor and ferromagnet layers, presented within chapter 3 were originally motivated by a number of anomalous results in the field, not least the work reported in [39] which uncovered, through the use of LEμSR, what appeared to be a tunable and remotely induced magnetism within a normal metal. From this earlier work, it was clear ferromagnetism was important in generating the effect but its origins were unclear and it could not be interpreted within any existing theory picture. The work discussed in chapter 3 sought to pin down at what stage the existing theory failed to explain the experimental data. It was clear from these control measurements that both the thin film superconductors and the NS bilayer systems could be successfully modelled using the London and quasiclassical theories respectively. The point of breakdown came when, through the addition of a thin ferromagnetic layer to the underside of the superconductor, a large diamagnetic enhancement to the screening was observed [60]. This work, along with references [39, 82], prompted the development of a new theory to describe a substantial and hitherto unknown effect: the electromagnetic proximity effect.

In light of the newly developed EM proximity picture, the focus of chapter 4 was to both test the main predictions of the theory and examine whether the data on simple S, NS and NSF structures could now be successfully interpreted. Through application of a theoretical flux profile, consistent with that predicted by theory, to the LEμSR data an excellent correspondence between theory and experiment was found. At the very least this suggested the core idea of the EM theory, that an additional source of vector potential at the S/F interface induces a screening response inside the superconductor over λ_L, was an appropriate description of the physics observed at the S/F interface [84]. The measurements, however, could not identify for certain the mechanism through which the additional vector potential influenced the superconductor.

To further investigate the new theory a systematic experiment involving the manipulation of the S/F interface using insulating oxide barriers was conducted as discussed within chapter 5. The results of this study unambiguously determined that the direct sampling of the exchange field by the superconducting wavefunction is the source of the EM proximity effect. It was also demonstrated, through a full spatial analysis of the LEμSR data, that the EM proximity within the measured systems was both substantially larger than the effects of pair breaking and approximately constant for oxide barrier thicknesses of up to 4 nm [83]. The former suggests the importance of accounting for effects of electromagnetic origin when both interpreting experimental data and within S/F device design. The latter motivates the further development of theory to investigate how other factors, for example the superconducting gap strength at the interface, may effect the generation of the EM amplitude.

Within the final chapter the properties of platinum, both to generate proximity effects in its own right and as a means to manipulate the N/S and S/F interfaces, were investigated. A number of interesting observations were made. The presence of platinum within the sample structures was determined in all cases to have a profound effect on the sample behaviour. The most likely explanation for the set of measurements as a whole was that the platinum promotes the generation of a paramagnetic, as opposed to a diamagnetic, electromagnetic amplitude whenever it forms an interface with niobium. This is perhaps a surprising result since platinum is simply a normal metal, albeit one with interesting material properties, however the average muon data suggest this is the case. Moreover, the results of temperature and field scans reflect an additional component to the signal not observed within any system in which platinum is absent. In light of the insight brought by the averages approach to the LEμSR data analysis a full spatial analysis of the data may now be possible. This could involve the application of analytical, or even numerical, flux profiles to the existing data. A more systematic knowledge of the platinum material properties and how the systems behave at low, or even zero, applied fields is required, however, before any detailed conclusions can be drawn. Future application of SQUID magnetometry and LEμSR experiments conducted in alternative measurement geometries could be key in uncovering the details of the mechanisms at play within the platinum systems and how these mesh with the current understanding of proximity effects within these heterostructures.

The sum of the work presented across all four experimental chapters represents a step-change in understanding of proximity effects within S/F hybrid systems. An entirely new contribution to the flux profile was uncovered and the associated theory of an underlying mechanism for its generation developed as a result. The remaining open questions largely fall within three separate categories:

i) The precise origin, beyond simply the vector potential of the ferromagnetic layer, of the EM amplitude. More specifically, the role of spin-orbit and Rashba effects within these systems and whether or not they form an important basis for the generation of the EM amplitude.

ii) Expansion of the theory to account for other factors explicitly, such as the superconducting gap strength at the interface, on which the EM proximity may depend.

iii) How to optimise the S/F interfaces with the goal of specific applications in mind. For example, does this newly described proximity theory have an adverse effect on device physics and if so how can this be minimised?

With continued effort to address these questions the role of the EM proximity effect within S/F hybrid systems can continue to be developed and potentially utilised within devices.

A | Details of the Levenberg - Marquardt fit method

The Levenberg-Marquardt algorithm is a numerical recipe which solves least squares problems that typically arise when fitting a parameterised function to a set of fixed data points [95]. It does so by minimising the sum of the squares of the errors between the data points and the fit function. This is achieved through iterative updates to the parameter values. A schematic of the minimisation protocol adopted by the Levenburg-Marquardt method is shown in figure A.1. Here the function to be minimised is the least squares function $f(x)$. In regions where the solution is far away from a minimum the algorithm uses the gradient descent method (GD) which updates parameters in the direction of steepest descent and near a minimum the Gauss-Newton (GN) method is adopted which assumes a quadratic local form to $f(x)$ and alters the parameters towards its minimum.

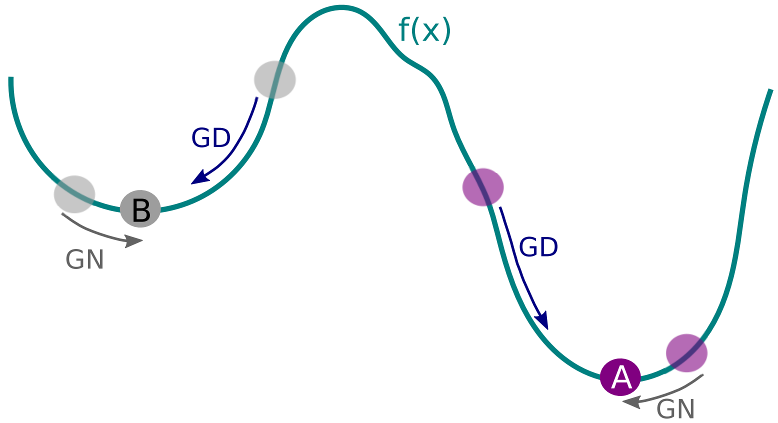

Figure A.1: A schematic of the minimisation protocol adopted by the Levenburg-Marquardt algorithm. In regions far away from the minimum of the least squares function, $f(x)$, it uses gradient descent (GD) and close to a minimum it uses Gauss-Newton (GN). Where the initial parameter guess is far away from the global minimum, A, it is possible to become trapped in a local minimum, B.

Given a "good" initial guess of fit parameters the Levenberg-Marquardt algorithm is a reliable and efficient method to find a best fit, however, it is important to note that if the initial input parameters are very far away from the global minimum (A) then it is also possible to become trapped in a local minimum (B) giving a misleading result.

If $y(x_i)$ represents the data measured at discrete points x_i, with some associated Gaussian experimental error of standard deviation σ_i, and $y_{fit}(x_i)$ the fit to be made to the data then the statistical error to be minimised is given by equation A.1.

$$Err = \frac{1}{N}\sum_{i=1}^{N}\frac{(y_{fit}(x_i) - y(x_i))^2}{\sigma_i} = \frac{\chi^2}{N} \tag{A.1}$$

where N is the total number of discrete points and $\chi^2 = \frac{(y_{fit}(x_i)-y(x_i))^2}{\sigma_i}$ the goodness of fit parameter. Where $\chi^2 \approx 1$ there is a close correspondence between the measured data and the fit. Typically, when fitting a data set one looks for a set of parameter values which can offer a physically sensible description of the data and a corresponding χ^2 value close to unity.

B | Transport data: definition of the T_c and H_{c2} criteria

This appendix gives further details about the analysis methods used for all transport data. In particular, the criteria for T_c and H_{c2} extraction are given and justified. Figure B.1 shows an example set of transport data measured on the Nb(50 nm) film from sample Set II [45] which we will use as an illustration of the procedures followed.

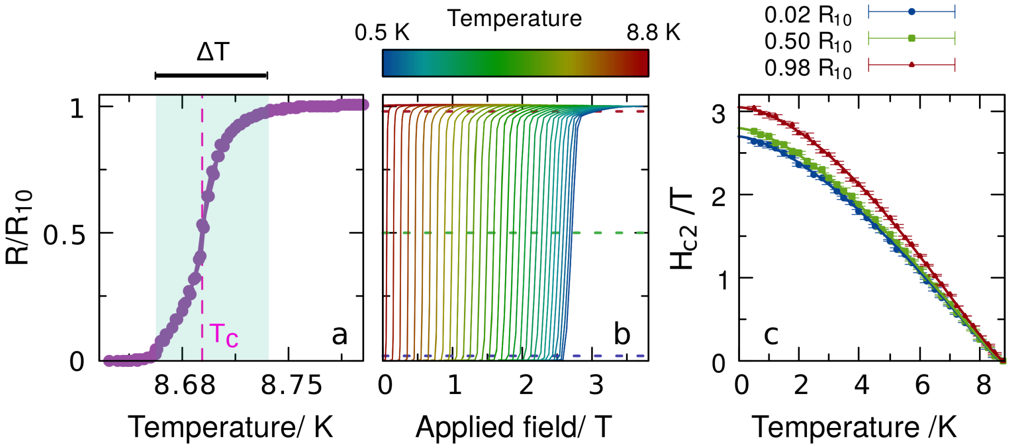

Figure B.1: Transport data for a Nb(50 nm) film: definition of T_c and H_{c2}. a) Normalised resistance against temperature plot. The shaded region represents the transition width, ΔT, defined as the temperature range over which the resistance falls from 98% to 2% of the normal state value. The value of T_c is extracted at 50% of the normal state resistance as indicated by the vertical dashed line. b) Normalised resistance as a function of applied field for a range of temperatures $(0.5 - 8.8)$ K. The horizontal dashed lines correspond to the 2%, 50% and 98% normal state resistance criteria for extracting H_{c2}. c) Upper critical field as a function of temperature for the 2% (blue), 50% (green) and 98% (red) criteria. The points are the extracted values and the solid lines show a fit to the data using GL theory.

---

[45] See chapter 3 for further details,

B.1 Resistance-temperature data

For dirty thin film superconductors and proximity systems it is possible for the superconducting transition to become broadened or even to exhibit plateaus and step-like features. The extent to which this happens in our systems depends on the quality of the sample growth and can be related to impurities, roughness and interface resistances. In such cases it becomes important to define a consistent criteria with which to extract the critical temperature (T_c). This is especially important when seeking to make comparisons between data sets where we may expect to see small differences in T_c due to, for example, the presence of a normal metal or ferromagnetic material in direct contact with a superconductor.

Figure B.1(a) shows the resistance-temperature data for the Nb(50 nm) film from sample set II ($\lambda_L = 140$ nm). There are two useful quantities to extract from this plot in order to characterise the behaviour: the value of T_c, defined as the temperature at which the resistance reaches half the normal state value (R_{10}); and the transition width ΔT, defined as the temperature range over which the resistance falls from 98% to 2% of R_{10}. The vertical dashed line in figure B.1 indicates the value of T_c, in this case 8.69 K, and the width of the shaded region corresponds to ΔT which for this sample is 72 mK. For all samples we follow this same convention when extracting T_c and ΔT.

B.2 Upper critical field-temperature data

When modelling the behaviour of our superconducting thin film samples using the quasiclassical framework there are a number of physical tuning parameters. In many cases it is possible to fix these parameters to their experimentally determined values for a given system. One measurement that is important in this regard is to determine H_{c2} as a function of temperature since through fits to this data the coherence length, and hence diffusion constant, for the superconductor can be extracted [46]. As may be expected, we have found the extracted values to differ quite markedly from those for a bulk system. For example, typical superconducting coherence lengths for our mesoscopic samples fall within the $(7-12)$ nm range as opposed to the 30 nm expected for a bulk sample of Nb. This section gives further details about the conventions we use when determining these values.

---

[46] Please see chapter 2 for more details

Figure B.1(b) shows a series of resistance against applied field curves, plotted for a range of temperatures $(0.5 - 8.8)$ K, from which we extract the upper critical field as a function of temperature. The dashed horizontal lines show the three test criteria used: 2%, 50% and 98% of R_{10}. When one considers the shape of the transition with applied field there is some broadening evident at the high field side which reduces as the measurement temperature gets closer to T_c. This becomes more clearly visible in the plots of upper critical field as a function of temperature for the 2% (blue), 50% (green) and 98% (red) criteria plotted in figure B.1(c). The curves extracted at 2% and 50% of R_{10} show good agreement with one another across the full temperature range whereas the 98% curve deviates due to the broadening effect. The origin of the resistance-field curve broadening is unknown but does not appear to be a fixed feature of the sample behaviour. We have measured multiple pieces of the same sample, for example, and the broadening effect is only visible in those pieces taken from an edge region of the film. This leads us to believe it may be related to inhomogeneities in the film thickness towards the edge of the as grown film. To avoid any anomalies associated with this behaviour we choose to extract all $H_{c2}(T)$ curves at $2\%R_{10}$.

C | Depolarisation rate as a function of probing depth: the effect of a ferromagnetic layer

As discussed in chapters 2 and 3, wherever a sample is composed in part of a ferromagnetic layer then there will be a marked effect on the muon depolarisation rate due to the associated stray fields. In the case of the normal metal - superconductor - ferromagnet structures measured here this can be modelled using an exponential profile as previously shown by equation 2.8 within section 2.1.6. This is the approach taken here in the analysis of all NSF samples and is essential in disentangling the effects of stray fields from, say, changes to flux profiles associated with unconventional states. This is particularly important within chapter 5 where the effects of insulating barriers on proximity effects between Nb and Co are explored.

Whilst examples of the model profiles and extracted parameters have been given within the main content of this thesis, and subsequently compared with the results of the conventional averages approach, here the effect of the stray fields on the raw data is shown directly. Figure C.1 shows a comparison of raw LEμSR spectra measured at different average depths. At a muon energy of $E_{\mu} = 4\ keV$ (top) all of the muons stop within the copper and there is very little evidence of damping in the signal amplitude as a function of time. As the probing energy increases to $E_{\mu} = 14\ keV$ (centre), and subsequently to $E_{\mu} = 23\ keV$ (bottom), the fraction of muons stopping within the region close to the ferromagnet and consequently the depolarisation rate increases. This is clearly visible as an increase in the damping, from top to bottom in figure C.1, which goes from 0.6 MHz to 2.1 MHz as a function of probing depth.

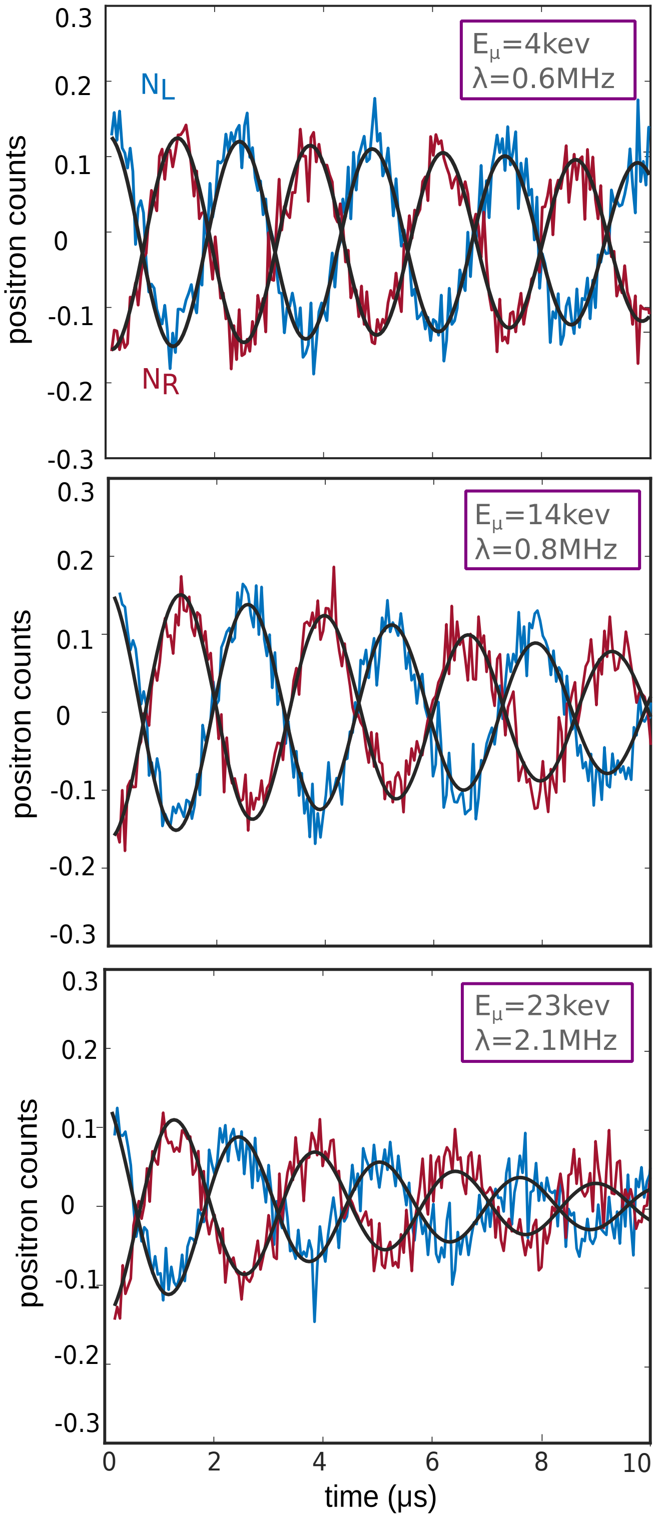

Figure C.1: Comparison of raw muon detector spectra for different average probing depths within an NSF thin film sample. From top to bottom the average probing depth increases. This results in more muons stopping within the region close to the Cobalt layer and thus the damping rate increases.

The spectra within figure C.1 are representative of all the NSF and NSIF samples containing cobalt layers that were measured as part of the investigations presented within this thesis. It is important to note that whilst the damping rate does increase for higher muon energies the detector signals are still easily fit with the usual damped cosine form only now the associated error in the extracted $\langle B \rangle$ will be slightly larger[47]. In systems with rough or textured ferromagnets however, which are not considered in detail here, the depolarisation rate can increase to within the range $(10 - 20)\ MHz$. In this case the spectra are so strongly damped that fitting, and thus extraction of $\langle B \rangle$, becomes extremely challenging. To combat this the number of muon events (N_μ) must be increased to the order of 10 million counts where the error decreases as $1/\sqrt{N_\mu}$. Of course, this only helps if the depolarisation is not so strong as to completely damp away any evidence of oscillations.

---

[47] In general increasing to $\pm 0.3\ G$ when compared with the $\pm 0.1\ G$ for lower probing energies.

D | Comparison of transport and muon T_c in more detail

This appendix relates directly to the measurements discussed in Chapter 3. It provides the opportunity to look at a comparison between the measured transport T_c and the value observed in LEμSR experiments for each sample structure. Figure D.1 presents the measured temperature dependence of $\langle B \rangle$ for a) N(II), b) NS(II) and c) NSF(II) which are shown separately for clarity. The plotted points are the flux averages extracted from the fits to the muon data and the vertical lines represent the T_c values determined from transport. In each case the temperature at which the flux lowering becomes observable coincides well with the respective transport T_c. Interestingly, the difference in temperature dependence between the bilayer and trilayer samples is linear. This suggests the EM component develops linearly with decreasing temperature.

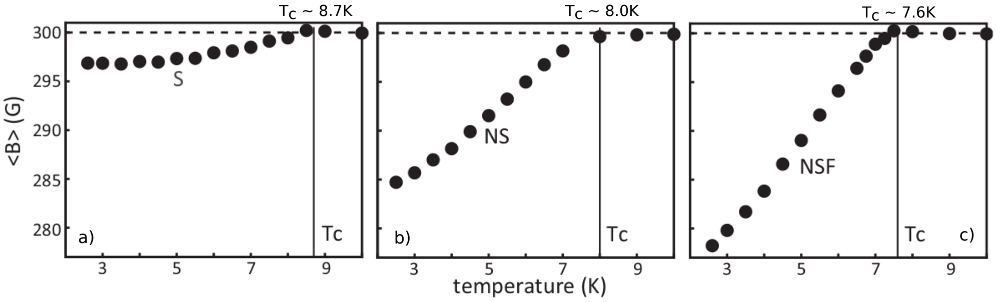

Figure D.1: Comparison of muon and transport T_c for a) S(II) measured at 8 keV, b) NS(II) and c) NSF(II) both measured at 11 keV. In each case the data points show $\langle B \rangle$ as a function of temperature measured using LEμSR and the vertical lines indicate the transport T_c for each sample.

E | Limitations of TF LEμSR at low applied field

The muons which are implanted into a sample thermalise, whilst preserving their initial spin direction, before beginning to Larmor precess around the local field. After collecting a statistically significant number of events the resultant positron spectrum shows a, possibly damped, oscillation at a frequency determined by the the local field experienced by the muon ensemble. If this field should be low, and consequently the frequency of the signal low, then it becomes difficult to fit the spectra since there are few or partial oscillations within the time window of the measurement. This can in part be combated by collecting more counts but low field is perhaps best investigated in another geometry or through zero field measurements.

Figure E.1 shows some example LEμSR data for lower applied fields. In the left panel the result of measuring at an applied field of $B_0 = 25\ G$ is displayed and on the right the applied field was set to 100 G.

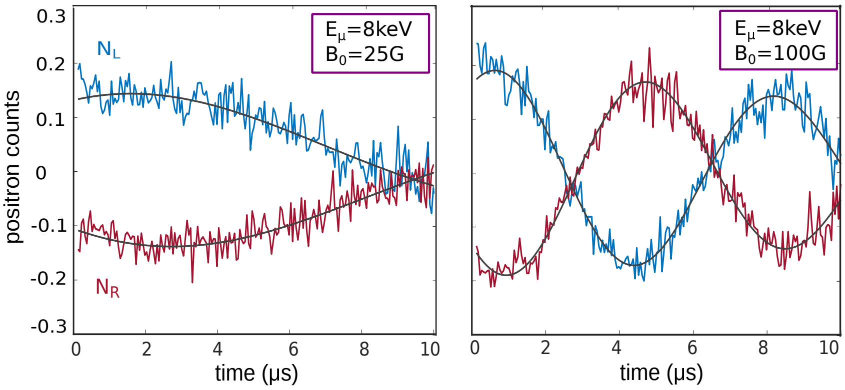

Figure E.1: A comparison of LEμSR spectra, with their associated fits, for different applied field. Left panel: For $B_0 = 25\ G$ only a half oscillation is visible within the time window. Right panel: For $B_0 = 100\ G$ the spectra can be more accurately and precisely fit.

In each case the spectra still contain enough information to obtain a reasonable fit to the data. Any further reduction in the applied field, however, would present a problem since only a partial half oscillation will remain. This is why in this spin rotation type of measurement we cannot gain access to lower values of applied field and still obtain an accurate picture of the average field.

In chapter 3, figure 3.11(c) presents the extracted signal amplitude as a function of the applied field for the NSF(I) trilayer sample. This was measured down to $B_0 = 25\ G$. The dependence of the total signal with applied field looks to be linear with extrapolation indicating $\delta B(0) = 0\ G$. However, it is important to take care when interpreting the low field data in this geometry, for the reasons cited above, so further experiments conducted at zero field could prove to be important in determining whether the signal does in fact persist in the absence of an external field or whether it is somehow linked to the Meissner response.

F | EM proximity in gold capped samples

Within this appendix are presented the results of LEμSR experiments on gold capped samples. These measurements were part of a follow up study to the work presented in [39]. Within this set of experiments the samples of interest were largely superconducting spin valves some of which had antiferromagnetically pinned cobalt layers. They are included here to provide further evidence for the EM proximity effect but since these samples do not have all of the required control measurements it is not possible to model them fully within this picture. They do, however, provide a useful addition to the discussion and indeed raise some interesting discussion points in their own right.

The data presented here were measured on three separate samples with the following corresponding layouts where the bracketed numbers represent the layer thicknesses in nanometers.

1. A standard superconducting spin valve stack with free cobalt layers: Au(120)/Nb(50)/Co(2.4)/Nb(3)/Co(1.2)/Ta(7.5)/Si
2. A superconducting spin valve stack with free and antiferromagnetically pinned cobalt layers. The IrMn is the pinning layer in this case: Au(120)/Nb(50)/Co(2.4)/Nb(3)/Co(1.2)/IrMn(4)/Co(3)/Ta(7.5)/Si
3. A simple thin capped trilayer: Au(5)/Nb(50)/Co(2.4)/Si

For brevity these sample layouts are labelled NSFF, NSFFAF and NSF respectively in what follows. Whilst the sample structures are themselves relatively complex the manner in which they are discussed here is, broadly speaking, in relation only to the NSF segment. This is because we are primarily interested in the physics at the S/F interface and how this relates to the presence, or absence, of the thick normal metal layer.

Figure F.1 presents the LEμSR results on the gold capped sample structures. The left panel shows the results on the spin valve structures, NSFF and NSFFAF, which have been scaled to the same measurement temperature for ease of comparison. This was achieved simply by using the temperature dependence of the signal amplitude, measured at $E_\mu = 23\ keV$ for the NSFFAF structure, as shown in the inset of figure F.1. By finding the gradient of the $\langle B \rangle - T$ plot below T_c and assuming a linear dependence within the region of interest it was possible to scale the NSFFAF data, actually measured at $T = 2.5\ K$, to match the NSFF data measured at $T = 2.9\ K$. The left panel of figure F.1 displays the results of this analysis. When one considers the resultant data it is clear that across all measured energies the two samples are the same within the error. This provides evidence that it is really just the NSF component which generates the additional contribution which can be attributed to the EM proximity at the S/F interface.

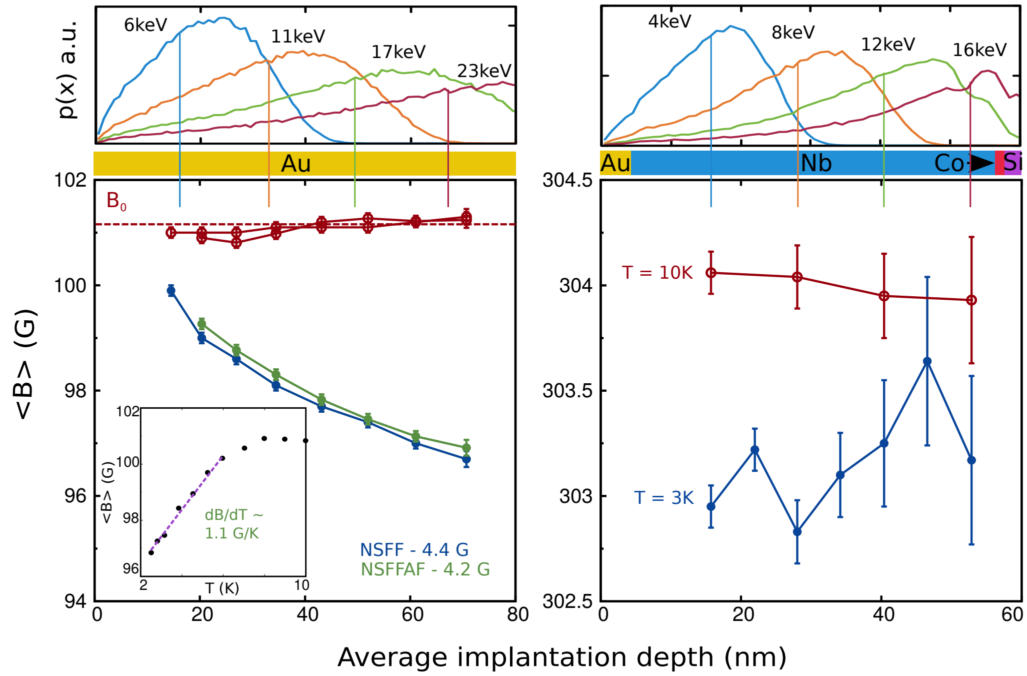

Figure F.1: LEμSR results on gold capped samples. For all data the normal (superconducting) state values are plotted in open (closed) symbols and the lines are a guide to the eye. In each case the top panel shows some sample muon stopping profiles with the respective average probing depths indicated by the vertical lines. Left panel: results for the NSFF and NSFFAF samples which have been scaled to the same measurement temperature, using the gradient of the $\langle B \rangle - T$ data, for ease of comparison. The inset displays the average flux as a function of temperature measured at $E_\mu = 23\ keV$ for the NSFFAF sample. Right panel: results for the AuNbCo sample which show no evidence of an EM proximity effect.

Additionally, in these spin valve samples the much thicker normal metal layer, 120 nm of gold when compared with only 40 nm of copper, offers the opportunity to see how the normal metal proximity and, to a degree, the EM proximity develops over a longer lengthscale. It is clear that the screening in this case has still developed across the full spatial extent of the NS section since even at the lowest measured energy there is a substantial flux expulsion observed. Unfortunately, due to the lack of appropriate control samples within the set it is not possible to model the different contributions explicitly. It is possible, however, to do a quick comparison between this data and the NSF(I) trilayer results simply by scaling the measured amplitudes to the same applied field. In the case of these measurements on NSFF and NSFFAF structures an amplitude of around $B \approx 4.4\ G$ was measured for an applied field of $B_0 \approx 100\ Oe$. This would correspond, using the field dependence measured on NSF(I) shown in figure 3.11 to scale the data, to a projected amplitude of $B \approx 13\ G$ for an applied field of $B_0 \approx 300\ Oe$. This is comparable to the NSF trilayer sample from growth Set I and suggests the two components, Meissner and EM, may be of similar order and behaviour in these more complex samples. This provides further evidence that the key ingredients in determining the physics are the NSF sections and that the ferromagnet needs to be in direct contact with the condensate.

The right panel of figure F.1 presents the results of LEμSR measurements on a simple NSF trilayer sample but this time with a normal metal layer only 5 nm thick. By comparing the data measured above and below T_c it is clear there is very little to see in terms of flux expulsion. For the higher probing energies there appears to be a small measured effect of approximately 1 G in amplitude which corresponds to a percentage expulsion of $\approx 0.3\%$. When one compares this result to the single Nb(50) sample from Set I, the results on which can be found in figure 3.5, it is clear the two signals differ approximately by a factor of two in amplitude. Interestingly, within this thin capped sample there is no evidence of a large EM proximity amplitude at the S/F interface. This appears to suggest that rather than being just a fixed feature of an S/F interface the EM proximity, or at least the sense in which it manifests within these measurements, may be a modification to the orbital screening current rather than the result of a static effect. This is consistent with the field dependence measurements on NSF(I) presented in figure 3.11 which tentatively suggest $\delta B(0) \to 0$.

When taken together these results on the gold capped samples show several things. Firstly, as expected, the normal metal proximity effect is not limited to copper and works comparatively well with gold which has a somewhat similar mean free path and coherence length to the sputtered copper. The much thicker N layers allow the relevant lengthscales to be explored in more detail. It is clear the normal metal proximity continues to develop over the full extent of the Au/Nb bilayer section. The pairs, despite being generated by a single Nb(50) layer, are able to propagate and screen throughout the 120 nm thickness of gold. The fact the total signal amplitudes measured for the NSFF and NSFFAF samples can be directly compared with the NSF(I) results suggest the important ingredients are the N, S and F layers and that only the direct S/F interface plays a role in setting up the EM effect. The results on the NSF with the thin gold cap are additionally very interesting. Here the absence of a thick normal metal means the standard Meissner effect does not experience the usual "boost" associated with the normal proximity effect and only a small Meissner amplitude of $0.3\% B_0$ is observed. In this system there is no evidence of a large EM amplitude at the Nb/Co interface. The observed signal suggests any EM amplitude would be in fact only ≈ 0.5 G. This, combined with the field dependence measurement in figure 3.11, suggests the EM effect may have an alternative origin, at least in these systems, to that currently discussed in the theory though further systematic measurements are required to explore this in more detail.

G | The effect of a copper spacer layer at the S/F interface

The results presented within section 6.2.2 on the Cu(40)/Nb(50)/Pt(2)/Co(2.4)/Nb(3)/Si sample structure suggest that the presence of even a thin platinum spacer layer at the S/F interface can have a substantial effect on the measured signal. Whilst the spatial profile across the sample was consistent in shape to the results for NSF(I), the total amplitude was much lower than even the bilayer response of comparable niobium quality and the onset of a net diamagnetic screening amplitude occurred 2 K below T_c. When taken together these results suggest the platinum layer at the interface significantly altered the interaction between the superconductor and ferromagnet. Though the precise nature of the effect was unclear it seemed most likely that the Pt(2) layer modified either the S/F interface or the way in which the superconductivity sampled the ferromagnet in such a way as to produce a positive value of A_{EM}. Within this appendix, the results of an LEμSR energy scan on a similar NSnF structure, but one where the spacer layer is composed of copper instead of platinum, are presented for comparison. The sample structure was grown in the same vacuum cycle, using the same niobium target purity, as sample Set II which is discussed within chapter 3.

The results of the LEμSR measurements performed on a range of samples of the form Cu(40)/Nb(50)/X, with X=Si, Co(2.4)/Nb(3)/Si and Cu(2)/Co(2.4)/Nb(3)/Si, are presented within figure G.1. The top panel displays the usual muon stopping profiles for a subset of the measurement energies where the vertical lines correspond to the average probing depths in each case. Within the main panel are shown the results of the conventional averages approach to the data analysis. The extracted average flux values are plotted as a function of their corresponding average probing depths.

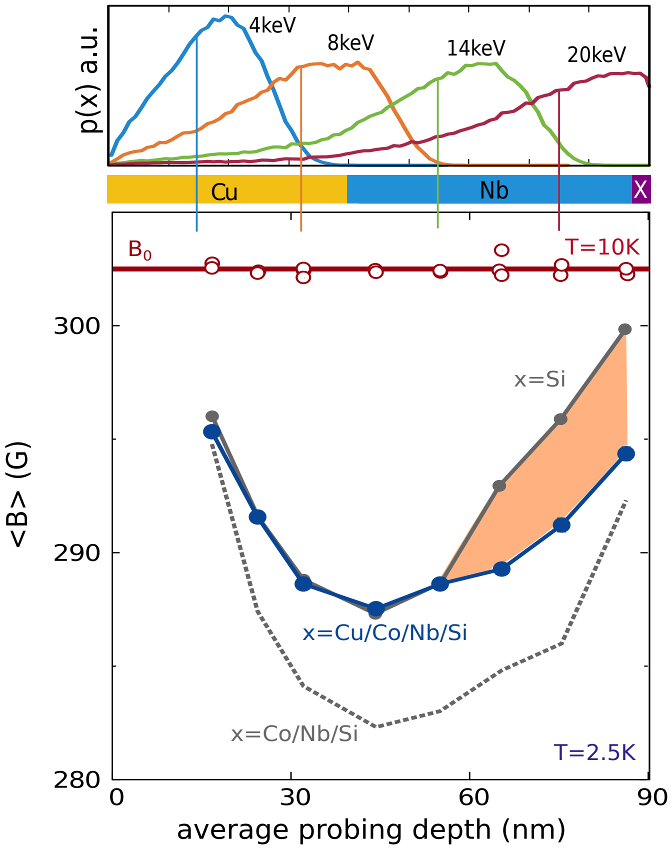

Figure G.1: LEμSR results for the Cu(40)/Nb(50)/Cu(2)/Co(2.4) sample structure plotted along side the results on the relevant NS and NSF control samples. Top panel: presented are some sample muon stopping profiles for a range of selected implantation energies. The corresponding vertical lines indicate the average stopping depth in each case. Bottom panel: the extracted flux averages as a function of the average probing depth for a range of samples of the form Cu(40)/Nb(50)/X with X = Si, Cu(2)/Co(2.4)/Nb(3)/Si and Co(2.4)/Nb(3)/Si corresponding to the NS, NSnF and NSF samples respectively. All normal (superconducting) state data were measured at $T = 10\ K$ ($T = 2.5\ K$) and are plotted in open (closed) symbols. The grey dashed line outlines the response for the NSF control sample and the shaded region indicates the modified EM response at the SnF interface.

All normal and superconducting state measurements were conducted at temperatures of 10 K and 2.5 K and are plotted in open and closed symbols respectively. All of the normal state measurements recovered the applied field which was set to around 302 Oe. In the superconducting state, for the X=Cu(2)/Co(2.4)/Nb(3)/Si sample, there is once again a flux lowering observed across all energies. When the sample with the copper spacer is compared with the NS(II) (grey points) and NSF(II) (dotted lines) it appears the total amplitude lies somewhere between the two control samples. The difference between NS(II) and the copper spacer sample, indicated by the shaded region, suggests the additional component has its origin at the S/F interface and decays away towards the sample surface. In addition, it appears the Meissner response is slightly reduced, as expected in the presence of pair breaking effects, and the EM amplitude is also reduced when compared with the usual response at the Nb(50)/Co(2.4) interface.

The results of chapter 5 suggest that both the coupling strength between S and F and the gap strength at the interface may have an effect on the amplitude of the resultant EM proximity response. Given that in the copper spacer sample the superconductivity in direct contact with the ferromagnet is proximity induced then the gap may be weaker, less robust and the resultant EM amplitude smaller. The expected result is then a total screening amplitude lying somewhere between NS(II) and NSF(II) as observed in figure G.1. In the case of the Cu(2) spacer layer the material parameters are such that the copper becomes readily proximitised, as demonstrated extensively in previous samples, and behaves simply as a normal metal with proximity induced superconductivity. In the case of the Pt(2) spacer layer, however, due to its unusual material properties it seems the resultant EM amplitude may be flipped in sign.

References

[1] A. I. Buzdin. Proximity effects in superconductor-ferromagnet heterostructures. *Rev. Mod. Phys.*, 77:935–976, 2005.

[2] F. S. Bergeret, A. F. Volkov, and K. B. Efetov. Odd triplet superconductivity and related phenomena in superconductor-ferromagnet structures. *Rev. Mod. Phys.*, 77:1321, 2005.

[3] M. Eschrig. Spin-polarized supercurrents for spintronics: a review of current progress. *Rep. Prog. Phys.*, 78:104501, 2015.

[4] R. M. Lutchyn, E. P. A. M. Bakkers, L. P. Kouwenhoven, P. Krogstrup, C. M. Marcus, and Y. Oreg. Majorana zero modes in superconductor–semiconductor heterostructures. *Nat. Rev. Mater.*, 3:52–68, 2018.

[5] H. Kammerlingh Onnes. *Leiden Communications*, 119b,120b,124c, 1911.

[6] D. van Delft and P. Kes. The discovery of superconductivity. *Phys. Today*, 63(9):38–42, 2010.

[7] F. Y. Ogrin, S. L. Lee, A. D. Hillier, A. Mitchell, and T.-H. Shen. Interplay between magnetism and superconductivity in Nb/Co multilayers. *Phys. Rev. B*, 62:6021–6026, 2000.

[8] Y. Obi, M. Ikebe, T. Kubo, and Hi. Fujimori. Oscillation phenomena of transition temperatures in Nb/Co and V/Co superconductor-ferromagnet multilayers. *Phys. C*, 317-318:149–153, 1999.

[9] Ya. V. Fominov, N. M. Chtchelkatchev, and A. A. Golubov. Nonmonotonic critical temperature in superconductor/ferromagnet bilayers. *Phys. Rev. B*, 66:014507, 2002.

[10] J. S. Jiang, D. Davidović, Daniel H. Reich, and C. L. Chien. Oscillatory superconducting transition temperature in Nb/Gd multilayers. *Phys. Rev. Lett.*, 74:314–317, 1995.

[11] J. S. Jiang, D. Davidović, D. H. Reich, and C. L. Chien. Superconducting transition in Nb/Gd/Nb trilayers. *Phys. Rev. B*, 54:6119–6121, 1996.

[12] I. A. Garifullin, D. A. Tikhonov, N. N. Garif'yanov, L. Lazar, Yu. V. Goryunov, S. Ya. Khlebnikov, L. R. Tagirov, K. Westerholt, and H. Zabel. Re-entrant superconductivity in the superconductor/ferromagnet V/Fe layered system. *Phys. Rev. B*, 66:020505, 2002.

[13] Y. Blum, A. Tsukernik, M. Karpovski, and A. Palevski. Oscillations of the superconducting critical current in Nb-Cu-Ni-Cu-Nb junctions. *Phys. Rev. Lett.*, 89:187004, 2002.

[14] T. Kontos, M. Aprili, J. Lesueur, F. Genêt, B. Stephanidis, and R. Boursier. Josephson junction through a thin ferromagnetic layer: Negative coupling. *Phys. Rev. Lett.*, 89:137007, 2002.

[15] J. W. A. Robinson, S. Piano, G. Burnell, C. Bell, and M. G. Blamire. Critical current oscillations in strong ferromagnetic π junctions. *Phys. Rev. Lett.*, 97:177003, 2006.

[16] T. S. Khaire, W. P. Pratt, and Norman O. Birge. Critical current behavior in Josephson junctions with the weak ferromagnet PdNi. *Phys. Rev. B*, 79:094523, 2009.

[17] T. Kontos, M. Aprili, J. Lesueur, and X. Grison. Inhomogeneous superconductivity induced in a ferromagnet by proximity effect. *Phys. Rev. Lett.*, 86:304–307, 2001.

[18] V. V. Ryazanov, V. A. Oboznov, A. Yu. Rusanov, A. V. Veretennikov, A. A. Golubov, and J. Aarts. Coupling of two superconductors through a ferromagnet: Evidence for a π junction. *Phys. Rev. Lett.*, 86:2427–2430, 2001.

[19] Qifeng Liang, Yong Yu, Qianghua Wang, and Jinming Dong. Controllable $0-\pi$ transition in a superconducting graphene-nanoribbon junction. *Phys. Rev. Lett.*, 101:187002, 2008.

[20] C. Cirillo, C. Bell, G. Iannone, S. L. Prischepa, J. Aarts, and C. Attanasio. Nonmonotonic behavior of the anisotropy coefficient in

superconductor-ferromagnet-superconductor trilayers. *Phys. Rev. B*, 80:094510, 2009.

[21] A. Singh, S. Voltan, K. Lahabi, and J. Aarts. Colossal proximity effect in a superconducting triplet spin valve based on the half-metallic ferromagnet CrO_2. *Phys. Rev. X*, 5:021019, 2015.

[22] R. S. Keizer, S. T. B. Goennenwein, T. M. Klapwijk, G. Miao, G. Xiao, and A. Gupta. A spin triplet supercurrent through the half-metallic ferromagnet CrO_2. *Nature*, 439:825, 2006.

[23] T. S. Khaire, Mazin A. Khasawneh, W. P. Pratt, and Norman O. Birge. Observation of spin-triplet superconductivity in Co-based Josephson junctions. *Phys. Rev. Lett.*, 104:137002, 2010.

[24] J. W. A. Robinson, J. D. S. Witt, and M. G. Blamire. Controlled injection of spin-triplet supercurrents into a strong ferromagnet. *Science*, 329:59–61, 2010.

[25] J. W. A. Robinson, G. B. Halász, A. I. Buzdin, and M. G. Blamire. Enhanced supercurrents in Josephson junctions containing nonparallel ferromagnetic domains. *Phys. Rev. Lett.*, 104:207001, 2010.

[26] J. Wang, M. Singh, M. Tian, N. Kumar, B. Liu, C. Shi, J. K. Jain, N. Samarth, T. E. Mallouk, and M. H. W. Chan. Interplay between superconductivity and ferromagnetism in crystalline nanowires. *Nat. Phys.*, 6:389–394, 2010.

[27] M. S. Anwar, F. Czeschka, M. Hesselberth, M. Porcu, and J. Aarts. Long-range supercurrents through half-metallic ferromagnetic CrO_2. *Phys. Rev. B*, 82:100501, 2010.

[28] J. Y. Gu, J. Kusnadi, and C.-Y. You. Proximity effect in a superconductor/exchange-spring-magnet hybrid system. *Phys. Rev. B*, 81:214435, 2010.

[29] D. Sprungmann, K. Westerholt, H. Zabel, M. Weides, and H. Kohlstedt. Evidence for triplet superconductivity in Josephson junctions with barriers of the ferromagnetic Heusler alloy Cu_2MnAl. *Phys. Rev. B*, 82:060505, 2010.

[30] W. Meissner and R. Ochsenfeld (A. M. Forrest Trans.). Ein neuer effekt bei eintritt der supraleitfähigkeit (a new effect at the onset of superconductivity). *Die Naturwissenschaften*, 21:787, 1933.

[31] M. Alidoust, K. Halterman, and J. Linder. Meissner effect probing of odd-frequency triplet pairing in superconducting spin valves. *Phys. Rev. B*, 89:054508, 2014.

[32] A. Di Bernardo, Z. Salman, X. L. Wang, M. Amado, M. Egilmez, M. G. Flokstra, A. Suter, S. L. Lee, J. H. Zhao, T. Prokscha, E. Morenzoni, M. G. Blamire, J. Linder, and J. W. A. Robinson. Intrinsic paramagnetic Meissner effect due to s-wave odd-frequency superconductivity. *Phys. Rev. X*, 5:041021, 2015.

[33] V. N. Krivoruchko and E. A. Koshina. Inhomogeneous magnetism induced in a superconductor at a superconductor-ferromagnet interface. *Phys. Rev. B*, 66:014521, 2002.

[34] F. S. Bergeret, A. F. Volkov, and K. B. Efetov. Induced ferromagnetism due to superconductivity in superconductor-ferromagnet structures. *Phys. Rev. B*, 69:174504, 2004.

[35] F. S. Bergeret, A. Levy Yeyati, and A. Martín-Rodero. Inverse proximity effect in superconductor-ferromagnet structures: From the ballistic to the diffusive limit. *Phys. Rev. B*, 72:064524, 2005.

[36] R. I. Salikhov, I. A. Garifullin, N. N. Garif'yanov, L. R. Tagirov, K. Theis-Bröhl, K. Westerholt, and H. Zabel. Experimental observation of the spin screening effect in superconductor/ferromagnet thin film heterostructures. *Phys. Rev. Lett.*, 102:087003, 2009.

[37] J. Xia, V. Shelukhin, M. Karpovski, A. Kapitulnik, and A. Palevski. Inverse proximity effect in superconductor-ferromagnet bilayer structures. *Phys. Rev. Lett.*, 102:087004, 2009.

[38] M. G. Flokstra, S. J. Ray, S. J. Lister, J. Aarts, H. Luetkens, T. Prokscha, A. Suter, E. Morenzoni, and S. L. Lee. Measurement of the spatial extent of inverse proximity in a Py/Nb/Py superconducting trilayer using low-energy muon-spin rotation. *Phys. Rev. B*, 89:054510, 2014.

[39] M. G. Flokstra, N. Satchell, J. Kim, G. Burnell, P. J. Curran, S. J. Bending, J. F. K. Cooper, C. J. Kinane, S. Langridge, A. Isidori, N. Pugash, M. Eschrig, H. Luetkens, A. Suter, T. Prokscha, and S. L. Lee. Remotely induced magnetism in a normal metal using a superconducting spin-valve. *Nat. Phys.*, 12:57–61, 2016.

[40] S. Mironov, A. S. Mel'nikov, and A. Buzdin. Electromagnetic proximity effect in planar superconductor-ferromagnet structures. *Appl. Phys. Lett.*, 113(2):022601, 2018.

[41] Zh. Devizorova, S. V. Mironov, A. S. Mel'nikov, and A. Buzdin. Electromagnetic proximity effect controlled by spin-triplet correlations in superconducting spin-valve structures. *Phys. Rev. B*, 99:104519, 2019.

[42] A. F. Volkov, F. S. Bergeret, and K. B. Efetov. Spin polarization and orbital effects in superconductor-ferromagnet structures. *Phys. Rev. B*, 99:144506, 2019.

[43] L. N. Cooper. Bound electron pairs in a degenerate Fermi gas. *Phys. Rev.*, 104:1189–1190, 1957.

[44] J. Bardeen, L. N. Cooper, and J. R. Schrieffer. Microscopic theory of superconductivity. *Phys. Rev.*, 106:162–164, 1957.

[45] J. Bardeen, L. N. Cooper, and J. R. Schrieffer. Theory of superconductivity. *Phys. Rev.*, 108:1175–1204, 1957.

[46] M. Eschrig. Spin-polarized supercurrents for spintronics. *Rev. Mod. Phys.*, 64:43, 2011.

[47] A. C. Rose-Innes and E. H. Rhoderick. *Introduction to Superconductivity.* Pergamon Press, London, 1994.

[48] D. K. Finnemore, T. F. Stromberg, and C. A. Swenson. Superconducting properties of high purity niobium. *Phys. Rev.*, 149, 1966.

[49] G. P. Felcher, R. T. Kampwirth, K. E. Gray, and R. Felici. Polarized-neutron reflections: A new technique used to measure the magnetic field penetration depth in superconducting niobium. *Phys. Rev. Lett.*, 52:1539–1542, 1984.

[50] A. Suter, E. Morenzoni, N. Garifianov, R. Khasanov, E. Kirk, H. Luetkens, T. Prokscha, and M. Horisberger. Observation of non-exponential magnetic penetration profiles in the Meissner state: A manifestation of nonlocal effects in superconductors. *Phys. Rev. B*, 72:024506, 2005.

[51] A. Romanenko, A. Grassellino, F. Barkov, A. Suter, Z. Salman, and T. Prokscha. Strong Meissner screening change in superconducting radio frequency cavities due to mild baking. *Appl. Phys. Lett.*, 104:072601, 2014.

[52] H. Zhang, J. W. Lynn, C. F. Majkrzak, S. K. Satija, J. H. Kang, and X. D. Wu. Measurements of magnetic screening lengths in superconducting Nb thin films by polarized neutron reflectometry. *Phys. Rev. B*, 52:10395–10404, 1995.

[53] A. I. Gubin, K. S. Il'in, S. A. Vitusevich, M. Siegel, and N. Klein. Dependence of magnetic penetration depth on the thickness of superconducting Nb thin films. *Phys. Rev. B*, 72:064503, 2005.

[54] P. G. De Gennes and E. Guyon. Superconductivity in 'normal metals'. *Phys. Lett.*, 3:168–169, 1963.

[55] N. R. Werthamer. Theory of superconducting transition temperature and energy gap of superposed metal films. *Phys. Rev.*, 132:2440–2445, 1963.

[56] A. F. Andreev. Thermal conductivity of the intermediate state of superconductors. *Sov. Phys. JETP*, 19:1228–1230, 1964.

[57] M. J. M. de Jong and C. W. J. Beenakker. Andreev reflection in ferromagnet-superconductor junctions. *Phys. Rev. Lett.*, 74:1657–1660, 1995.

[58] W. Belzig, C. Bruder, and G. Schön. Local density of states in a dirty normal metal connected to a superconductor. *Phys. Rev. B*, 54:9443–9448, 1996.

[59] W. Belzig, C. Bruder, and G. Schön. Diamagnetic response of normal metal-superconductor double layers. *Phys. Rev. B*, 53:5727–5733, 1996.

[60] M. G. Flokstra, R. Stewart, N. Satchell, G. Burnell, H. Luetkens, T. Prokscha, A. Suter, E. Morenzoni, S. Langridge, and S. L. Lee. Observation of anomalous Meissner screening in Cu/Nb and Cu/Nb/Co thin films. *Phys. Rev. Lett.*, 120:247001, 2018.

[61] C. Espedal, T. Yokoyama, and J. Linder. Anisotropic paramagnetic Meissner effect by spin-orbit coupling. *Phys. Rev. Lett.*, 116:127002, 2016.

[62] I. V. Bobkova and A. M. Bobkov. Quasiclassical theory of magnetoelectric effects in superconducting heterostructures in the presence of spin-orbit coupling. *Phys. Rev. B*, 95:184518, 2017.

[63] R. Meservey, P. M. Tedrow, and P. Fulde. Magnetic field splitting of the quasiparticle states in superconducting aluminium films. *Phys. Rev. Lett.*, 18:1270–1272, 1970.

[64] P. M. Tedrow and R. Meservey. Spin-dependent tunneling into ferromagnetic nickel. *Phys. Rev. Lett.*, 26:192–195, 1971.

[65] P. M. Tedrow and R. Meservey. Spin polarisation of electrons tunneling from films of $\mathrm{Fe, Co, Ni}$ and Gd. *Phys. Rev. B*, 7:318–325, 1973.

[66] A. I. Larkin and Y. N. Ovchinnikov. Inhomogeneous state of superconductors. *Sov. Phys. JETP*, 20:262–269, 1965.

[67] P. Fulde and R. A. Ferrell. Superconductivity in a strong spin exchange field. *Phys. Rev.*, 135:550–563, 1964.

[68] F. S. Bergeret, A. F. Volkov, and K. B. Efetov. Long-range proximity effects in superconductor-ferromagnet structures. *Phys. Rev. Lett.*, 86:4096–4099, 2001.

[69] M. Eschrig and T. Löfwander. Triplet supercurrents in clean and disordered half-metallic ferromagnets. *Nat. Phys.*, 4:138–143, 2008.

[70] A. Balatsky and E. Abrahams. New class of singlet superconductors which break the time reversal and parity. *Phys. Rev. B*, 45:13125–13128, 1992.

[71] R. Matthias Geilhufe and Alexander V. Balatsky. Symmetry analysis of odd- and even-frequency superconducting gap symmetries for time-reversal symmetric interactions. *Phys. Rev. B*, 97:024507, 2018.

[72] J. Linder and J. W. A. Robinson. Superconducting spintronics. *Nat. Phys.*, 11:307–315, 2015.

[73] A. Singh, C. Jansen, K. Lahabi, and J. Aarts. High-quality CrO_2 nanowires for dissipation-less spintronics. *Phys. Rev. X*, 6:041012, 2016.

[74] M. G. Flokstra, T. C. Cunningham, J. Kim, N. Satchell, G. Burnell, P. J. Curran, S. J. Bending, C. J. Kinane, J. F. K. Cooper, S. Langridge, A. Isidori, N. Pugach, M. Eschrig, and S. L. Lee. Controlled suppression of superconductivity by the generation of polarized cooper pairs in spin-valve structures. *Phys. Rev. B*, 91:060501, 2015.

[75] L. R. Tagirov. Low-field superconducting spin switch based on a superconductor /ferromagnet multilayer. *Phys. Rev. Lett.*, 83:2058–2061, 1999.

[76] A. I. Buzdin, A. V.Vedyayev, and N. V. Ryzhanova. Spin-orientation-dependent superconductivity in F/S/F structures. *JETP Lett.*, 91(6):308–313, 2010.

[77] Ya. V. Fominov, A. A. Golubov, T. Yu. Karminskaya, M. Yu. Kupriyanov, R. G. Deminov, and L. R. Tagirov. Superconducting triplet spin valve. *JETP Lett.*, 91(6):308–313, 2010.

[78] I. C. Moraru, W. P. Pratt, and N. O. Birge. Magnetization-dependent T_c shift in ferromagnet/superconductor/ferromagnet trilayers with a strong ferromagnet. *Phys. Rev. Lett.*, 96:037004, 2006.

[79] A. Yu. Rusanov, S. Habraken, and J. Aarts. Inverse spin switch effects in ferromagnet-superconductor-ferromagnet trilayers with strong ferromagnets. *Phys. Rev. B*, 73:060505, 2006.

[80] I. C. Moraru, W. P. Pratt, and N. O. Birge. Observation of standard spin-switch effects in ferromagnet/superconductor/ferromagnet trilayers with a strong ferromagnet. *Phys. Rev. B*, 74:220507, 2006.

[81] A. Iovan, T. Golod, and V. M. Krasnov. Controllable generation of a spin-triplet supercurrent in a Josephson spin valve. *Phys. Rev. B*, 90:134514, 2014.

[82] Yu. N. Khaydukov, B. Nagy, J. H. Kim, T. Keller, A. Rühm, Yu. V. Nikitenko, K. N. Khernenkov, J. Stahn, L. F. Kiss, A. Csik, L. Bottyán, and V. L. Aksinov. On the feasibility to study inverse proximity effect in a single S/F bilayer by polarized neutron reflectometry. *JETP Lett.*, 98:107, 2013.

[83] R. Stewart, M. G. Flokstra, M. Rogers, N. Satchell, G. Burnell, D. Miller, H. Luetkens, T. Prokscha, A. Suter, E. Morenzoni, and S. L. Lee. Controlling the electromagnetic proximity effect by tuning the mixing between superconducting and ferromagnetic order. *Phys. Rev. B*, 100:020505, 2019.

[84] M. G. Flokstra, R. Stewart, N. Satchell, G. Burnell, H. Luetkens, T. Prokscha, A. Suter, E. Morenzoni, S. Langridge, and S. L. Lee. Manifestation of the electromagnetic proximity effect in superconductor-ferromagnet thin film structures. *Appl. Phys. Lett.*, 115:072602, 2019.

[85] Yu. N. Khaydukov, E. A. Kravtsov, V. D. Zhaketov, V. V. Progliado, G. Kim, Yu. V. Nikitenko, T. Keller, V. V. Ustinov, V. L. Aksenov, and B. Keimer. Magnetic proximity effect in Nb/Gd superlattices seen by neutron reflectometry. *Phys. Rev. B*, 99:140503, 2019.

[86] A. Yaouanc and P. Dalmas de Réotier. *Muon Spin Rotation, Relaxation, and Resonance: Applications to Condensed Matter.* Oxford University Press, Oxford, 2011.

[87] S. L. Lee, S. H. Kilcoyne, and R. Cywinski. *Muon Science: Muons in Physics, Chemistry and Materials.* Institute of Physics Publishing, Bristol, 1998.

[88] S. F. J. Cox. Implanted muon studies in condensed matter science. *J. Phys. C: Solid State Physics*, 20(22):3187–3319, 1987.

[89] S. J. Blundell. Spin-polarized muons in condensed matter physics. *Contemp. Phys.*, 40(3):175–192, 1999.

[90] P. Bakule and E. Morenzoni. Generation and applications of slow polarized muons. *Contemp. Phys.*, 45:203, 2004.

[91] T. Prokscha, E. Morenzoni, K. Deiters, F. Foroughi, D. George, R. Kobler, A. Suter, and V. Vrankovic. The new μE4 beam at PSI:

A hybrid-type large acceptance channel for the generation of a high intensity surface-muon beam. *Nucl. Instr. and Meth. A*, 595:317–331, 2008.

[92] *LEM instrument documentation.* Laboratory for muon spin spectroscopy, Paul Scherrer Institute, Switzerland, 2018.

[93] E. Morenzoni, H. Glückler, T. Prokscha, R. Khasanov, H. Luetkens, M. Birke, E. M. Forgan, Ch. Niedermayer, and M. Pleines. Implantation studies of kev positive muons in thin metallic layers. *Nucl. Instr. and Meth. B*, 192:254–266, 2002.

[94] W. Eckstein. *Computer Simulation of Ion-Solid Interactions.* Springer, New York, 1991.

[95] W. H. Press, S. A. Teukolsky, W. T. Vetterling, and B. P. Flannery. *Numerical Recipes: The Art of Scientific Computing.* Cambridge University Press, Cambridge, 2007.

[96] P. G. de Gennes. *Superconductivity of Metals and Alloys.* (P. Pincus Trans.), Westview Press, Boulder, 1999.

[97] *Mini Cryogen-Free Magnet System User Manual.* London, UK, 2013.

[98] *Model 6220 DC Current Source Model 6221 AC and DC Current Source User's Manual., 2^{nd} edition.* Cleveland, Ohio, USA, 2005.

[99] I. Miccoli, F. Edler, H. Pfnür, and C. Tegenkamp. The 100th anniversary of the four-point probe technique: the role of probe geometries in isotropic and anisotropic systems. *J. Phys.: Condens. Matter*, 27(22):223201, 2015.

[100] D. V. Dimitrov, G. C. Hadjipanayis, V. Papaefthymiou, and A. Simopoulos. Magnetic properties and microstructure of $\mathrm{Fe-O}$ and $\mathrm{Co-O}$ thin films. *IEEE trans. magn.*, 33(5):4363–4366, 1997.

[101] M. Gruyters. Cobalt oxide/ ferromagnet bilayers: Exchange coupling and dominance of the antiferromagnet. *EPL*, 64:803, 2003.

[102] D. L. Cortie, Y. W. Ting, P. S. Chen, X. Tan, K. W. Lin, and F. Klose. Enhancement of the magnetic interfacial exchange energy at a specific interface in NiFe/CoO/Co trilayer thin films via ion-beam modification. *J. Appl. Phys.*, 115:073901, 2014.

[103] J. Sugiyama, H. Nozaki, J. H. Brewer, E. J. Ansaldo, T. Takami, H. Ikuta, and U. Mizutani. Appearance of a two-dimensional antiferromagnetic order in quasi-one-dimensional cobalt oxides. *Phys. Rev. B*, 72:064418, 2005.

[104] *Magnetic Properties Measurement System., 2^{nd} edition.* San Diego, California, USA, 1999.

[105] M. M^{c}Elfresh. *Fundamentals of magnetism and magnetic measurements.* Quantum Design, San Diego, California, USA, 1994.

[106] T. P. Papageorgiou, L. Bauernfeind, and H. F. Braun. Possible pitfalls in squid magnetometry of superconducting samples: The case of $RuSr_2GdCu_2O_8$. *J. Low Temp. Phys.*, 131(1/2):129–143, 2003.

[107] M. Buchner, K. Höfler, B. Henne, V. Ney, and A. Ney. Basic principles, limits of detection, and pitfalls of highly sensitive squid magnetometry for nanomagnetism and spintronics. *J. Appl. Phys.*, 124:161101, 2018.

[108] F. B. Silsby. Current distribution in supraconductors. *Scientific papers of the bureau of standards.*, 22:293–315, 1927.

[109] J. N. Rjabinin and L. V. Shubnikov. Magnetic properties and critical currents of superconducting alloys. *Nature*, 135:581–582, 1935.

[110] D. Roher, L. Thiel, B Müller, M. Kasperczyk, R. Kleiner, D. Koelle, and P. Maletinsky. Real-space probing of the local magnetic response of thin-film superconductors using spin magnetometry. *Sensors*, 18:3790, 2018.

[111] Y. Oda and H. Nagano. Meissner effect in Cu of thick Cu-clad Nb. *Solid State Commun.*, 35:631, 1980.

[112] Y. Oda, A. Sumiyama, and H. Nagano. Meissner effect and magnetic field dependence of Cu-clad Nb in the mK region. *Japanese Journal of Applied Physics*, 22, 1983.

[113] H. Onoe, A. Sumiyama, M. Nakagawa, and Y. Oda. Superconducting proximity effect in Au of Au-clad Nb wire in the clean limit. *J. Phys. Soc. Jpn.*, 64:2138–2143, 1995.

[114] M. Wolz, C. Debuschewitz, W. Belzig, and E. Scheer. Evidence for attractive pair interaction in diffusive gold films deduced from studies of the superconducting proximity effect with aluminium. *Phys. Rev. B*, 84:104516, 2011.

[115] A. Stepniak, M. Caminale, A. A. Leon Vanegas, H. Oka, D. Sander, and J. Kirschner. Temperature dependence of the superconducting proximity effect quantified by scanning tunneling spectroscopy. *AIP Advances*, 5:017125, 2015.

[116] J. Linder, M. Cuoco, and A. Sudbø. Spin-active interfaces and unconventional pairing in half-metal/superconductor junctions. *Phys. Rev. B*, 81:174526, 2010.

[117] T. Yokoyama, Y. Tanaka, and N. Nagaosa. Anomalous Meissner effect in a normal-metal–superconductor junction with a spin-active interface. *Phys. Rev. Lett.*, 106:246601, 2011.

[118] F. S. Bergeret, A. Verso, and A. F. Volkov. Spin-polarized Josephson and quasiparticle currents in superconducting spin-filter tunnel junctions. *Phys. Rev. B*, 86:060506, 2012.

[119] I. Sosnin, H. Cho, V. T. Petrashov, and A. F. Volkov. Superconducting phase coherent electron transport in proximity conical ferromagnets. *Phys. Rev. Lett.*, 96:157002, 2006.

[120] L. Y. Zhu, Y. Liu, F. S. Bergeret, J. E. Pearson, S. G. E. te Velthuis, S. D. Bader, and J. S. Jiang. Unanticipated proximity behavior in ferromagnet-superconductor heterostructures with controlled magnetic noncollinearity. *Phys. Rev. Lett.*, 110:177001, 2013.

[121] D. Fritsch and J. F. Annett. Proximity effect in superconductor/conical magnet/ferromagnet heterostructures. *New J. of Phys.*, 16:055005, 2014.

[122] N. Banerjee, C. B. Smiet, R. G. J. Smits, A. Ozaeta, F. S. Bergeret, M. G. Blamire, and J. W. A. Robinson. Evidence for spin selectivity of triplet pairs in superconducting spin valves. *Nat. Commun.*, 5:3048, 2014.

[123] J. D. S. Witt, J. F. K. Cooper, N. Satchell, C. J. Kinane, P. J. Curran, S. J. Bending, S. Langridge, L. J. Heyderman, and G. Burnell. Magnetic phases of sputter deposited thin-film erbium. *Sci. Rep.*, 6:39021, 2016.

[124] N. Satchell, J. D. S. Witt, M. G. Flokstra, S. L. Lee, J. F. K. Cooper, C. J. Kinane, S. Langridge, and G. Burnell. Control of superconductivity with a single ferromagnetic layer in niobium/erbium bilayers. *Phys. Rev. Appl.*, 7:044031, 2017.

[125] N. G. Pugach, M. O. Safonchik, D. M. Heim, and V. O. Yagovtsev. Superconducting spin valves based on spiral magnets. *Phys. Solid State*, 60:2237–2243, 2018.

[126] S. Swann. Magnetron sputtering. *Phys. Technol.*, 19, 1988.

[127] P. J. Kelly and R. D. Arnell. Magnetron sputtering: a review of recent developments and applications. *Phys. Technol.*, 56:159–172, 2000.

[128] E. Chason and T. M. Meyer. Thin film and surface characterisation by specular x-ray reflectivity. *Crit. Rev. Solid State*, 22:1–67, 1997.

[129] M. Tinkham. *Introduction to Superconductivity.* M^{c}Graw-Hill INC., New York, 1980.

[130] V. Storchak, S. F. J. Cox, S. P. Cottrell, J. H. Brewer, G. D. Morris, D. J. Arseneau, and B. Hitti. Muonium formation via electron transport in silicon. *Phys. Rev. Lett.*, 78:2835–2838, 1997.

[131] M. G. Flokstra. *PhD thesis: Proximity effects in superconducting spin-valve structures.* Casimir PhD Series, Delft-Leiden, 2010.

[132] T. Lancaster and S. J. Blundell. *Quantum field theory for the gifted amateur.* Oxford university Press, Oxford, 2014.

[133] N. Nagaosa. *Quantum field theory in condensed matter physics.* (S. Heusler Trans.), Springer, Berlin, 2010.

[134] A. A. Abrikosov, L. P. Gorkov, and I. E. Dzyaloshinski. *Methods of quantum field theory in statistical physics.* (R. A. Silverman Trans.), Dover, New York, 1975.

[135] N. Kopnin. *Theory of non-equilibrium superconductivity.* Oxford University Press, Oxford, 2001.

[136] K. D. Usadel. Generalized diffusion equation for superconducting alloys. *Phys. Rev. Lett.*, 25:507–509, 1970.

[137] T. Löfwander, T. Champel, J. Durst, and M. Eschrig. Interplay of magnetic and superconducting proximity effects in ferromagnet-superconductor-ferromagnet trilayers. *Phys. Rev. Lett.*, 95:187003, 2005.

[138] Y. V. Nazarov. Novel circuit theory of Andreev reflection. *Superlattices Microstruct.*, 25:1221–1231, 1999.

[139] O. Narikiyo and H. Fukuyama. Proximity induced Meissner effect in dirty normal metals. *J. Phys. Soc. Jpn.*, 58:4557–4568, 1987.

[140] C. Kittel. *Introduction to solid state physics,* 7^{th} *edition.* Wiley, New York, 1996.

[141] F. J. Himpsel and D. E. Eastman. Experimental energy-band dispersions and magnetic exchange splitting for cobalt. *Phys. Rev. B*, 21, 1980.

[142] H. X. Wei, F. Q. Zhu, X. F. Han, Z. C. Wen, and C. L. Chien. Current-induced multiple spin structures in 100 nm ring magnetic tunnel junctions. *Phys. Rev. B*, 77:224432, 2008.

[143] M. S. Gabureac, K. J. Dempsey, N. A. Porter, C. H. Marrows, S. Rajauria, and H. Courtois. Spin-polarized tunneling with Au impurity layers. *J. Appl. Phys.*, 103:07A915, 2008.

[144] S. J. Pennycook and P. D. Nellist. *Scanning transmission electron microscopy: imaging and analysis.* Springer, New York, 2011.

[145] F. Hippert, E. Geissler, J. L. Hodeau, E. Lelièvre-Berna, and J. R. Regnard. *Neutron and* X*-ray spectroscopy.* Springer, Dordrecht, 2006.

[146] M. G. Blamire and J. W. A. Robinson. The interface between superconductivity and magnetism: understanding and device prospects. *J. Phys.: Condens. Matter*, 26:453201, 2014.

[147] A. Rusanov, R. Boogaards, M. Hesselberth, H. Sellier, and J. Aarts. Inhomogeneous superconductivity induced in a weak ferromagnet. *Phys. C*, 369:300–303, 2002.

[148] G. Gladstone, M. A. Jenson, and J. R. Schrieffer. *Superconductivity, Volume II.* Marcel Decker, New York, 2006.

[149] R. König, A. Schindler, and T. Herrmannsdörfer. Superconductivity of compacted platinum powder at very low temperatures. *Phys. Rev. Lett.*, 82:4528–4531, 1999.

[150] W. Zhang, V. Vlaminck, J. E. Pearson, R Divan, S. D. Bader, and A. Hoffmann. Determination of the Pt spin diffusion length by spin-pumping and spin Hall effect. *Appl. Phys. Lett.*, 103:242414, 2014.

[151] G. W. C. Kaye and T. H. Laby. *Tables of physical and chemical constants, sixteenth edition.* Longman, Essex, 1995.

[152] A. Manchon, H. C. Koo, J. Nitta, S. M. Frolov, and R. A. Duine. New perspectives for Rashba spin–orbit coupling. *Nat. Mater.*, 14:871–882, 2015.

[153] A. Soumyanarayanan, N. Reyren, A. Fert, and C. Panagopoulos. Emergent phenomena induced by spin–orbit coupling at surfaces and interfaces. *Nature*, 539:509–517, 2016.

[154] X. Montiel and M. Eschrig. Generation of pure superconducting spin current in magnetic heterostructures via nonlocally induced magnetism due to Landau Fermi liquid effects. *Phys. Rev. B*, 98:104513, 2018.

[155] M. Amundsen and J. Linder. Quasiclassical theory for interfaces with spin-orbit coupling. *Phys. Rev. B*, 100:064502, 2019.

[156] C. Bell, S. Milikisyants, M. Huber, and J. Aarts. Spin dynamics in a superconductor-ferromagnet proximity system. *Phys. Rev. Lett.*, 100:047002, 2008.

[157] T. Wakamura, N. Hasegawa, K. Ohnishi, Y. Niimi, and YoshiChika Otani. Spin injection into a superconductor with strong spin-orbit coupling. *Phys. Rev. Lett.*, 112:036602, 2014.

[158] T. Wakamura, H. Akaike, Y. Omori, Y. Niimi, S. Takahashi, A. Fujimaki, S. Maekawa, and Y. Otani. Quasiparticle-mediated spin Hall effect in a superconductor. *Nat. Mater.*, 14:675–678, 2015.

[159] J. A. Ouasson, A. Di Bernardo, J. W. A. Robinson, and J. Linder. Electric control of superconducting transition through a spin-orbit coupled interface. *Sci. Rep.*, 6:29312, 2016.

[160] N. Satchell and N. O. Birge. Supercurrent in ferromagnetic Josephson junctions with heavy metal interlayers. *Phys. Rev. B*, 97:214509, 2018.

[161] K.-R. Jeon, C. Ciccarelli, A.J. Ferguson, H. Kurebayashi, L. F. Cohen, X. Montiel, M. Eschrig, J. W. A. Robinson, and M. G. Blamire. Enhanced spin pumping into superconductors provides evidence for superconducting pure spin currents. *Nat. Mater.*, 17:499–503, 2018.

[162] Nathan Satchell, Reza Loloee, and Norman O. Birge. Supercurrent in ferromagnetic Josephson junctions with heavy-metal interlayers. ii. canted magnetization. *Phys. Rev. B*, 99:174519, 2019.

[163] K.-R. Jeon, C. Ciccarelli, H. Kurebayashi, L. F. Cohen, X. Montiel, M. Eschrig, S. Komori, J. W. A. Robinson, and M. G. Blamire. Exchange-field enhancement of superconducting spin pumping. *Phys. Rev. B*, 99:024507, 2019.

[164] G. Fischer, H. Hoffmann, and J Vancea. Mean free path and density of conduction electrons in platinum determined by the size effect in extremely thin films. *Phys. Rev. B*, 22:6065–6073, 1980.

[165] C. M. Yim. personal communication, July 2019.

[166] S. H. Tessmer, M. B. Tarlie, D. J. Van Harlingen, D. L. Maslov, and P. M. Goldbart. Probing the superconducting proximity effect in $NbSe_2$ by scanning tunneling microscopy. *Phys. Rev. Lett.*, 77:924–927, 1996.

[167] Y. Kalcheim, I. Felner, O. Millo, T. Kirzhner, G. Koren, A. Di Bernardo, M. Egilmez, M. G. Blamire, and J. W. A. Robinson. Magnetic field dependence of the proximity-induced triplet superconductivity at ferromagnet/superconductor interfaces. *Phys. Rev. B*, 89:180506, 2014.

[168] A. Di Bernardo, S. Diesch, J. Linder Y. Gu, G. Divitini, C. Ducati, E. Scheer, M.G. Blamire, and J.W.A. Robinson. Signature of magnetic-dependent gapless odd frequency states at superconductor/ferromagnet interfaces. *Nat. Commun.*, 6:8053, 2015.